UNIVERSITÀ DEGLI STUDI FIRENZE

DOTTORATO DI RICERCA IN
ATOMIC AND MOLECULAR PHOTONICS

(international doctorate)

CICLO XXVIII

COORDINATORE   Prof. Roberto Righini

MID-INFRARED SINGLE- AND MULTI-FREQUENCY COHERENT SOURCES FOR HIGH-RESOLUTION MOLECULAR SPECTROSCOPY

Settore scientifico-disciplinare FIS/03

Dottorando   Tutore
Dott. Francesco Cappelli   Dott. Paolo De Natale

_____   _____

Coordinatore

Prof. Roberto Righini

_____

30 novembre 2012 – 29 novembre 2015

Preface & Abstract

November 29, 2015

The *mid-infrared* portion of the electromagnetic spectrum is of particular interest due to the abundance and intensity of simple molecule absorption lines that fall in this spectral region. On the other hand, laser technologies are here still in development. This thesis, entitled *Mid-infrared single- and multi-frequency coherent sources for high-resolution molecular spectroscopy*, contains the collection of the *experiments* to which I have directly contributed during my PhD course. They all have been aimed to the generation and the control of coherent mid-infrared radiation for high-resolution molecular spectroscopy purposes. The proposed sources are based on *non-linear generation* and on *quantum cascade lasers*. The initial approach consisted in generating single-frequency mid-infrared radiation, eventually referenced to a near-infrared frequency comb. Subsequently, approaches to generate and control frequency combs directly in the mid infrared have been implemented.

The three-year PhD course that I have attended is the *International doctorate in atomic and molecular photonics*, organised by the European Laboratory for Non-Linear Spectroscopy - LENS in Florence (Italy). I have worked in the research group (part of the Italian National Institute of Optics - CNR-INO) led by my PhD supervisor Paolo De Natale. The expertise of the group is mainly in the fields of infrared frequency metrology, spectroscopy and trace-gas sensing. The international course provides for a period abroad. Thanks to a preexisting – I would say *natural* – collaboration, I had the opportunity of spending ten months during my second year at the Swiss Federal Institute of Technology (ETH) in Zürich working in Jérôme Faist's group. The expertise of the group is mainly in design, realisation and study of quantum cascade lasers. I'm very grateful to both the research groups for what I have learned in these highly stimulating years. I hope I have been helpful in carrying on the activities.

Francesco Cappelli

Preface II

This second version of my thesis is the result of the suggestions I received from my referees. I have to thank Piotr Masłowski and Stéphane Schilt for having accepted to referee my thesis and for having performed this task with competence and accuracy. In particular the appendix has been expanded by adding sections A.5 to A.7, and few minor revisions have been applied to the main text. I think that the overall quality of the manuscript has improved and for this reason I'm very grateful to both of them.

Francesco Cappelli

Contents

<div style="text-align: right">

Introduction

</div>

The interest in generating and detecting *infrared* radiation is high in today's society, in particular for applications in environment and health fields. The main absorption lines of simple molecules fall in this spectral region, and the study of the absorption spectra can give precise information on their concentration in gaseous samples. Moreover, molecular spectra deal with fundamental-physics open issues.

According to the ISO standard, the infrared region of the electromagnetic spectrum is classified as follows [1]:

<div style="text-align: center">

near-infrared (NIR) $0.78 - 3\ \mu$m

mid-infrared (MIR) $3 - 50\ \mu$m

far-infrared (FIR) $50 - 1000\ \mu$m

</div>

Carbon dioxide is one of the most important examples concerning simple molecules of environmental and biological interest. In the atmosphere, it contributes to the *greenhouse effect* [2, 3]. In addition, since it is generated in biological oxidation processes, it can give information on the health condition of live beings.

Another interesting application is the analysis of the concentration of *radiocarbon dioxide*[1] in a gaseous sample [4, 5], since the knowledge of this concentration enables the *dating* of the related biological specimen and can give again an insight on climate changes.

The observation of the electromagnetic absorption spectrum of the carbon dioxide molecule, shown in fig. I.1, clarifies the importance of the MIR region. The *fundamental ro-vibrational transitions* of the molecule

---

[1]Carbon dioxide made of ^{14}C atoms.

correspond to these frequencies. Since they are the fundamental ones, their line intensity is the highest in the whole absorption spectrum of the molecule. This peculiar feature, combined with refined spectroscopy
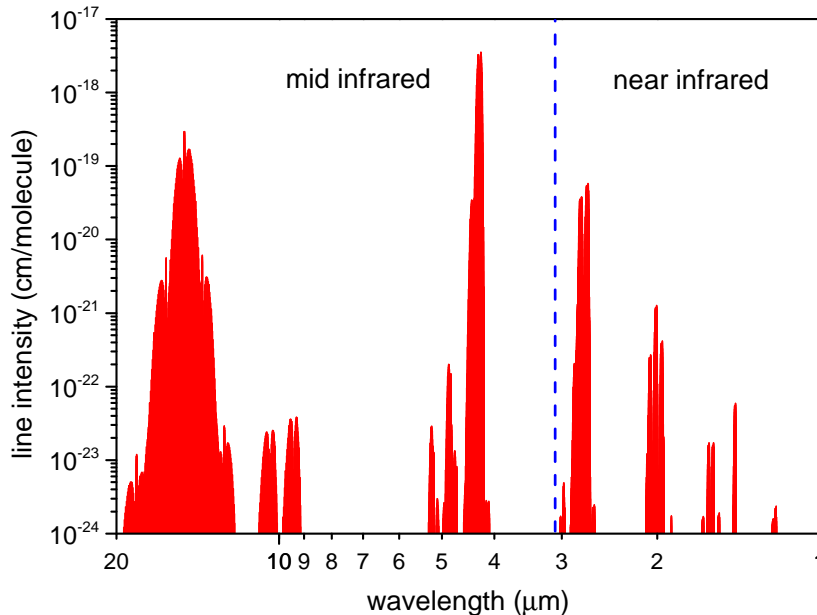
Figure I.1: CO_2 infrared absorption spectrum at a temperature $T = 300$ K, where the border between the mid infrared and the near infrared portions is pointed out. The most intense absorption lines fall in the mid infrared region (note the logarithmic scale). Source: HITRAN database [6].

techniques such as cavity ring-down [7], enables trace-gas sensing up to a part-per-quadrillion sensitivity. Moreover, such a strong dipole is useful in testing the strictness of the *symmetrization postulate*, which lies at the basis of the standard approach to quantum mechanics. If the spin of all the identical nuclei is zero, since the function has to be totally symmetric, all the antisymmetric states should be missing, together with the related transitions. Therefore, the search for these forbidden transitions can give an insight to which extent the symmetrization postulate is valid [8–10].

Visible and NIR are well covered in terms of *laser sources* and detection techniques and technologies as well, since research in this field historically started in these spectral regions [11, 12].[2] On the other hand, technologies in the MIR region are still in development. Such a gap is due to the lack of tunable and wavelength-engineerable laser

---

[2]It is worth reminding that the ancestors of the laser is the maser. This kind of device operates in the microwave region.

sources up to the invention of *quantum cascade lasers* (QCLs) in 1994
[13]. It was indeed necessary to apply quantum engineering in order
to extend semiconductor laser operation to the MIR. In the meanwhile,
coherent MIR radiation has been generated exploiting *frequency mixing
in non-linear crystals* starting from visible/NIR radiation [14, 15]. This
approach ensures wide tunability and high spectral purity, but presents
severe limitations in terms of generated power.

A tool that is nowadays essential in spectroscopy measurements is
the *optical frequency comb* (OFC). It has been found that the spectrum
of the radiation emitted by lasers operating in mode-locked regime [16]
(generating short coherent pulses) is made of a comb of perfectly equis-
paced and coherent modes. If the spectrum is wide enough,[3] they can be
self-referenced [17–19], serving as *rulers* for frequencies. These devices
have proven to be very useful both as references for continuous-wave
lasers as well as for direct comb spectroscopy [20–23].

Unfortunately, up to now there are no pulsed mode-locked lasers
operating in the MIR. The classical method for having OFCs in the
MIR takes again advantage of frequency mixing in non-linear crystals
starting from visible/NIR standard OFCs [24–28]. A recent and compact
approach employs high-*Q microresonators* pumped with continuous-
wave lasers, where the OFC is generated thanks to the Kerr effect [29–
33]. An alternative approach is provided by QCLs. Their unexpected
capability of generating OFCs has been discovered only recently [34]. It
has to be remarked that the comb formation, due to the four-wave mixing
process taking place in the gain medium, is peculiar. The phase relation
between the modes is similar to that of frequency-modulated lasers, no
pulses are emitted.

Both laser spectra and molecular transitions detected by laser spec-
troscopy in the real world are *broadened* by several phenomena. This
width sets a limit on the precision of determination of the laser emis-
sion frequency or of the molecular transition center frequency. On the
molecular side, the precision of the measurement can be greatly in-
creased overcoming the Doppler broadening even at room temperature
using techniques such as *saturation* and *polarization spectroscopy* [35].
These techniques have only been enabled by the introduction of lasers
in spectroscopy, since a highly-concentrated power (both in space and

---

[3]The spectrum has to cover an octave.

in frequency) is required. On the laser side, the linewidth can be greatly reduced resorting to stabilization techniques such as *phase locking* to a stable reference or *frequency locking* to molecular transitions. For stabilization purposes, it is of fundamental interest to study the frequency noise proper of the laser sources to be used.

This thesis deals with MIR spectroscopy. *Spectroscopy techniques* are discussed, with a particular focus on the *laser sources*. In particular, techniques to generate and stabilize both *single-frequency* and *multi-frequency* coherent MIR radiation are presented. In chapter 1 the theoretical background at the basis of the topic is recalled. In particular, in section 1.1 infrared molecular spectra, collective absorbing behavior (including the broadening phenomenon), and saturation and polarization spectroscopy techniques are presented. In section 1.2 optical non-linear second-order and third-order phenomena are discussed. Then, in section 1.3 optical frequency combs are introduced, discussing the mode-locking mechanism and their stabilization and absolute frequency referencing. In section 1.4 frequency noise in laser emission is discussed. Finally, in section 1.5 quantum cascade lasers are presented, discussing in particular their capability of generating frequency combs.

In chapter 2 seven experiments to which the author directly contributed during his PhD course are presented. In particular, in section 2.1 stabilized and referenced single-frequency MIR QCLs are proved as spectroscopy sources, using frequency locking to a molecular absorption line and phase locking to a metrological non-linear-generated radiation. On the other hand, in section 2.2 MIR OFCs generation, control and application as spectroscopy tools are presented. In particular, generation of a highly-coherent MIR OFC through intracavity difference-frequency generation is presented. Moreover, a frequency noise characterization and phase-locking of QCL OFCs is presented, useful for proving both the coherence and the potential spectroscopy performances of these sources. Finally, in the appendix details on the frequency-to-amplitude conversion (converter calibration and multimode conversion demonstration) used for frequency noise characterization are given, followed by the estimation of the Henry linewidth enhancement factor for a QCL. To conclude, a discussion on the relation between the two main optical parameters of a frequency comb (spacing and offset frequencies) and the waveguide effective refractive index and group refractive index is presented.

Theoretical framework

1.1 Molecular spectra detected by laser spectroscopy

Molecules, seen both as singles or taken as a whole, are rich and interesting physics systems. Spectroscopy basically studies their interaction with electromagnetic radiation. This section deals with molecular spectroscopy and it is essentially divided into two parts. The first one (sections 1.1.1 to 1.1.3) gives an overview on infrared molecular spectra, describing single molecules as systems and their interaction with light. The discussion focuses on linear molecules and in particular on carbon dioxide, giving examples of ro-vibrational spectral bands.

The second one (sections 1.1.4 to 1.1.7) introduces the collective absorbing behavior of a molecular gas sample, explaining the broadening phenomena (homogeneous and inhomogeneous) and the saturation. Then it focuses on two laser spectroscopy techniques (saturation and polarization spectroscopy) that enable the overcoming of the spectral-resolution limitation due to the inhomogeneous broadening, opening the way to room-temperature high-resolution spectroscopy.

1.1.1 Molecular energy levels

Considering the *Born-Oppenheimer approximation*, the eigenfunction describing a molecule can be factorized as follows:

$$\psi_m = \psi_t \psi_e \psi_n \psi_v \psi_r \tag{1.1}$$

where ψ_t describes the translation, ψ_e the electronic state, ψ_n the nuclear spin state, ψ_v the vibration and ψ_r the rotation of the molecule. The functions describing the vibrational states are very close to the ones describing the ideal harmonic oscillator, while the functions describing the rotational states are the spherical harmonics. For the moment we consider the molecule *stationary* in the considered reference frame, and it is assumed to stay in its electronic ground state.[1] In this way, the translational and electronic contributions can be omitted, considering only the rotational and vibrational ones.[2] Now the ro-vibrational energy of a molecule can be expressed as [36]

$$\frac{E}{h} = G(u_1, u_2, \dots) + F(J) \tag{1.2}$$

with h Plank constant.

The *vibrational contribution G* depends on the vibrational normal modes characterizing the considered molecule. Their number and nature are tightly linked to the symmetry properties of the molecule itself and are labeled u_1, u_2 and so on. For generic polyatomic molecules the number of vibrational degrees of freedom (DOF) is $(3N - 6)$, where N is the number of atomic nuclei in the molecule. This result comes considering that the motion of each atomic nucleus is described by 3 DOF, but looking at the molecule as a system, 3 of them describe the translation of the center of mass, while other 3 describe the rotation of the system. For linear molecules the number of vibrational DOF is equal to $(3N - 5)$ because there is no rotation around the molecular axis. Each vibrational mode can be in its ground state – for example $u_1 = 0$ – or in an excited state ($u_1 = 1, 2, \dots$). The vibrational contribution depends on the quantum numbers and the constants as follows:

$$
G(u_1, u_2, \dots) = \underbrace{\sum_i \nu_i \left(u_i + \frac{d_i}{2} \right)}_{\text{harmonic vibrations}}
$$
$$
+ \underbrace{\sum_{i,k \geq i} x_{ik} \left(u_i + \frac{d_i}{2} \right) \left(u_k + \frac{d_k}{2} \right)}_{\text{anharmonic corrections}} + \underbrace{\sum_{i,k \geq i} g_{ik} l_i l_k}_{\text{deg. rotation}} + \dots \tag{1.3}
$$

---

[1]This assumption is justified by the fact that the energy associated to mid- and far-infrared radiation is too low to excite electronic transitions ($E < 0.40$ eV).

[2]The nuclear spin contribution is neglected.

where index i counts the degenerate modes only once. $\nu_i = \omega_i/2\pi$ is the vibrational frequency related to the mode u_i. d_i counts its degree of degeneracy,[3] giving the zero-point energy. x_{ik} is the (small) anharmonicity constant. g_{ik} is a constant[4] related to the vibrational angular momentum of degenerate modes and l_i the related quantum number.[5]

On the other hand, the *rotational contribution F* depends on the total angular momentum number J ($J = 0, 1, 2, \dots$)[6] and reads as follows:

$$F(J) = \underbrace{BJ(J+1)}_{\text{rotational energy}} - \underbrace{DJ^2(J+1)^2}_{\text{centrifugal distortion}} + \dots \qquad (1.4)$$

where $B = h/8\pi^2 I$ is the rotational constant, I is the moment of inertia about an axis going through the center of mass. D is the (small) centrifugal distortion constant, related to the non rigidity of the molecule, accounting for the changing of the internuclear distances with increasing rotation. As a consequence of the interaction of vibration and rotation, the rotational constant shows a little dependence on the vibrational level. This is because the moment of inertia I changes during a vibration in such a way that the average value of $1/I$ is slightly different respect to its value in the equilibrium position. As a consequence, the expression for the rotational constant is

$$B_{[u]} = \underbrace{\frac{h}{8\pi^2 I}}_{\text{rest value}} - \underbrace{\sum_i \alpha_i \left(u_i + \frac{d_i}{2} \right)}_{\text{vibrational dependence}} \qquad (1.5)$$

where α_i are constants much smaller than the rest value. For the sake of completeness, even the constant D has a dependence on the vibrational state, but usually this effect is completely negligible.

The relative population of each level depends on J through the expression

$$N_J = g_J \, e^{-hF(J)/(k_B T)} \qquad (1.6)$$

where the term is the Boltzmann factor giving the population of the level, with k_B Boltzmann constant and T absolute temperature. For

---

[3] $d_i = 1$ if the mode is non-degenerate, $d_i = 2$ if it is doubly degenerate, and so on.
[4] g_{ik} is of the same order of magnitude of x_{ik}.
[5] $l_i = u_i, u_i - 2, u_i - 4, \dots, 1, 0$ if the mode is degenerate, while $l_i = 0$ (and $g_{ik} = 0$) if the mode is non-degenerate.
[6] Actually, for determining the smallest value that J can take, the vibrational level degeneracy has to be taken into account, because $J \geq l$.

linear asymmetric molecules $g_J = (2J+1)$ corresponds to the number of degenerate rotational sublevels, while for the symmetric ones that factor oscillates with J depending on the nuclear spin of the external atoms (see fig. 1.2 for an example).

1.1.2 Linear molecules ro-vibrational bands

In order to estimate the transitions that a certain molecule can show and their intensity, the dipole moment matrix element between the molecular states has to be computed. The absorption intensity is usually expressed in terms of *line intensity* (S), a parameter that accounts for the transition dipole moment and the levels population at thermal equilibrium for a given temperature T. Depending on the symmetry that characterizes a molecule, only certain transitions are allowed. As a consequence, some *selection rules* can be established. A molecule shows ro-vibrational transitions in the mid-infrared only if its dipole varies during the oscillation in one of its vibrational modes. This becomes evident writing the dipole matrix element [37]

$$\boldsymbol{M}_{ul \text{ vib}} = \vec{P}(0) \int \psi_{vl}\psi_{vu} \, d\tau_{\text{vib}} + \sum_{n=1}^{\text{vib. DOF}} \frac{\partial \vec{P}}{\partial q_n}\bigg|_0 \int \psi_{vl} q_n \psi_{vu} \, d\tau_{\text{vib}} \quad (1.7)$$

where $\vec{P}$ is the molecular dipole vector,[7] q_n are the nuclear displacement coordinates for the vibrational modes, and $d\tau_{\text{vib}}$ is the volume element in the q_n frame. The subscript u denotes the upper state, while l denotes the lower one. Since the two vibrational states are different and the vibrational wavefunctions are orthonormal, the first integral vanishes, leaving only the second term, which depends on the variation of the dipole during the oscillation in a certain vibrational mode.

Considering transitions between non degenerate vibrational states (Σ), the selection rules for ro-vibrational transitions impose [36]

$$\Delta u = u_u - u_l = \pm 1 \qquad (1.8a)$$

and

$$\Delta J = J_u - J_l = \pm 1 \qquad (1.8b)$$

---

[7]Here $\vec{P}$ is the dipole given by the placement of the atoms (with different electronegativity) in the molecule.

The transitions corresponding to $\Delta J = +1$ form the *R* branch, while the ones corresponding to $\Delta J = -1$ form the *P* branch. Once given the center frequency of the vibrational transition ν_0, each line forming the same *band*, given by the involved rotational levels $[F(J_u) - F(J_l)]$, is obtained by

$$\nu = \nu_0 + (B_u + B_l)\, m + (B_u - B_l)\, m^2 \qquad (1.9)$$

where $m = J + 1$ for the *R* branch and $m = -J$ for the *P* branch. In this formula the terms given by the centrifugal distortion ($\propto D$) have been neglected. These spectral lines are almost equispaced.

In order to properly understand the selection rules, we consider again eq. 1.1 and recall that the functions describing the vibrational states are very close to the ones describing the ideal harmonic oscillator, while the functions describing the rotational states are the spherical harmonics. We consider then the inversion operation, i.e. what happens reflecting each particle in the molecule with respect to the origin. The electronic function in the ground state is always symmetric. The same holds for the totally symmetric vibrational levels (Σ^+, e.g. the vibrational ground state). In these conditions the symmetry properties depend only on the rotational function. Levels with even *J* are positive, while levels with odd *J* are negative. The basic selection rule for dipole transitions states that positive levels can combine only with negative levels (and vice versa).

1.1.3 Symmetry properties

Linear molecules have been divided into two symmetry groups. The ones having a symmetry plane perpendicular to the molecular axis belong to the $D_{\infty h}$ group, the others to the $C_{\infty v}$ group. The carbon-dioxide molecule ($^{12}C^{16}O_2$) belongs to the first group, while the isotopologue $^{17}O^{12}C^{16}O$ belongs to the second one. The symmetric molecule $^{12}C^{16}O_2$ has zero permanent dipole moment. As a consequence the pure rotational spectrum in the far infrared cannot be observed and in the mid infrared only transitions involving vibrational modes with a periodic changing of the dipole moment[8] can be observed (see eq. 1.7). The CO_2 molecule has three vibrational modes (see fig. 1.1):

Symmetric stretch It is labeled u_1 and since it does not brake the molecular symmetry it's inactive in the mid infrared.

---

[8]This is possible only if the vibration *brakes* the symmetry of the molecule.

Bending It is labeled u_2 and it's doubly degenerate. For these mode the additional quantum number l is used. It is active in the mid infrared with a characteristic frequency of 667 cm^{-1}.

Asymmetric stretch It is labeled u_3 and it's active in the mid infrared with a characteristic frequency of 2349 cm^{-1} ($\lambda = 4.25$ μm).
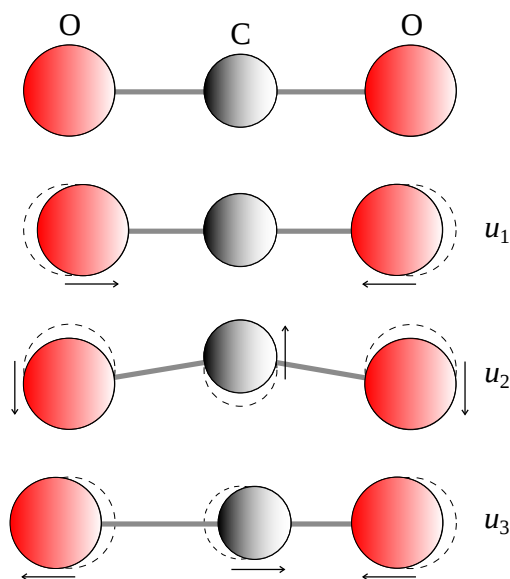

Figure 1.1: CO$_2$ vibrational modes: symmetric stretch, bending and asymmetric stretch.

The vibrational state of the molecule is expressed synthetically as $(u_1 u_2^l u_3)$. Symmetric linear molecules (group $D_{\infty h}$) have an additional symmetry property, they can be symmetric or antisymmetric with respect to an exchange of the identical nuclei. The total eigenfunction ψ of the system (apart from the nuclear spin function) remains unchanged or changes sign when all nuclei on one side of the center are simultaneously exchanged with the corresponding ones on the other side. The corresponding rotational states are called symmetric or antisymmetric in the nuclei. In general, considering the vibrational ground state Σ_g^+ (00^00), the positive rotational levels are symmetric (even J) and the negative antisymmetric (odd J), while in the first excited Σ_u^+ the property is inverted. For these molecules another selection rule holds: only levels with the same kind of symmetry can combine together. If the spin of all the identical nuclei is zero, since the function has to be totally symmetric, all the antisymmetric states are missing. This is the case for the ^{12}C^{16}O$_2$ molecule.

This question of the symmetry does not hold anymore if instead of the non-degenerate ground state Σ_g^+ we consider the first excited degenerate state Π_g (01^10). In this case all the rotational states are present. For a transition $\Pi_g \rightarrow \Pi_u$ $(01^10) \rightarrow (01^11)$ not only odd and even values of J are allowed, but also transitions with $\Delta J = 0$ are allowed. For this reason, the additional Q branch is present.[9] Since $J \geq l$ the first R and P branch lines are missing. Obviously the two transitions $(00^00) \rightarrow (00^01)$ and $(01^10) \rightarrow (01^11)$ are very close (almost overlapping) in frequency. This is the case for the $^{12}C^{16}O_2$ molecule spectrum around 4.25 μm (see fig. 1.2).

1.1.4 Homogeneous and inhomogeneous broadening

The aim of spectroscopy is to study the electromagnetic absorption spectra of gaseous samples. The simplest modern experimental scheme consists in a frequency-tunable laser source which generates a beam passing through a cell containing the sample gas and a detector to measure the transmitted light. For the moment we assume the laser source strictly monochromatic. Even avoiding any technical issue that could broaden the peaks related to the gas absorption, there are physics phenomena that let the spectral peaks appear broad [38], limiting the spectral resolution. The spectral line profile is said to be *homogeneously broadened* if the probability of absorption of resonant photons is equal for all the molecules of the sample that are in the same initial state. In other words, this probability must not depend on a property of the single molecule. The most important example is *natural broadening*, given by *spontaneous emission*. The shape of homogeneously broadened absorption lines is *Lorentzian*, as obtained with a semiclassical approach to the absorption of an electromagnetic wave by a collection of microscopic oscillators at rest, and stated by the Kramers-Kronig equations for the absorption

---

[9]For the Q branch, the frequency decreases with J. Moreover, for $\Pi_g \rightarrow \Pi_u$ transitions the intensity decreases very rapidly with J.
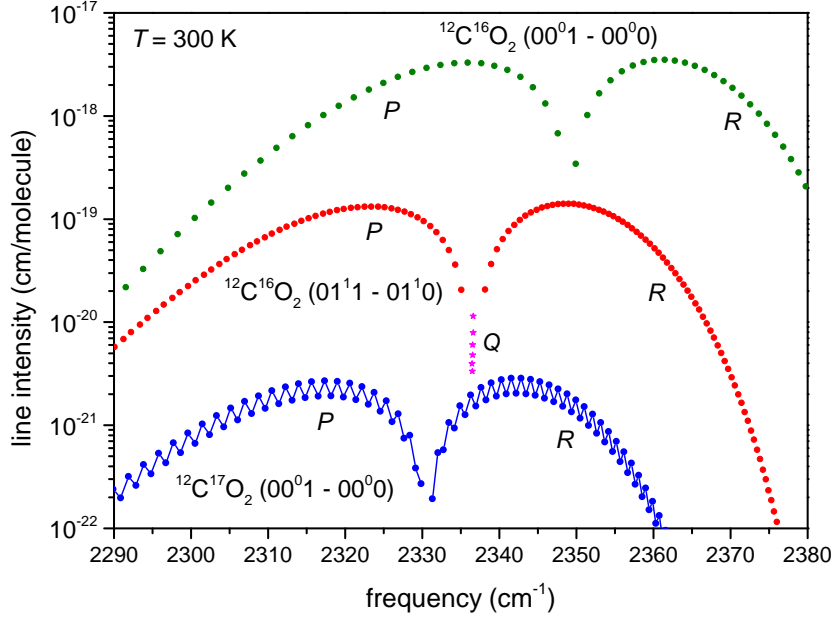
Figure 1.2: CO_2 bands around 4.25 μm at a temperature $T = 300$ K, where the frequency scale is expressed in cm^{-1} (1 cm$^{-1} \approx 30$ GHz). Three bands are shown. The $(00^01 - 00^00)$ band of the $^{12}C^{16}O_2$ molecule is the most intense, since it involves the fundamental vibrational level (00^00). Moreover this isotopologue is the most prevalent in nature (98.4 %). In this band only transitions involving a rotational ground state with even J are allowed by the vibrational levels symmetry and by the ^{16}O atoms nuclear spin (0). The $(01^11 - 01^10)$ band of the same isotopologue is also shown. It is a so-called *hot band*, since the lower level is not the ground state of the molecule. In this case the restriction on J does not hold, since the rotational levels do not have the same degree of symmetry of the previous case. Not only odd and even values of J are allowed, but also transitions with $\Delta J = 0$ are allowed. For this reason, the additional Q branch is present. For the sake of clearness, transitions belonging to this branch with line intensities $< 3 \times 10^{-21}$ cm/molecule have been artificially removed. Finally, the $(00^01 - 00^00)$ band of the $^{12}C^{17}O_2$ molecule is shown. For graphical reasons, the whole band has been *multiplied* by a factor 10^4. This isotopologue is quite rare, the natural abundance is 1.37×10^{-7}. It has the same symmetry of the $^{12}C^{16}O_2$ molecule, but the ^{17}O atoms nuclear spin is 5/2. For this reason, transitions involving a rotational ground state with odd J are not forbidden but show a different line intensity with respect to the others, resulting in the characteristic intensity modulation, artificially underlined in the graph with the trait connecting the dots representing the absorption lines. Source: HITRAN database [6].

coefficient and the refractive index[10]

$$\alpha(\omega) = \frac{Ne^2}{4\varepsilon_0 mc} \frac{\gamma}{(\omega - \omega_0)^2 + (\gamma/2)^2} \qquad (1.10a)$$

$$n(\omega) = 1 + \frac{Ne^2}{4\varepsilon_0 m\omega_0} \frac{\omega - \omega_0}{(\omega - \omega_0)^2 + (\gamma/2)^2} \qquad (1.10b)$$

where N is the number of oscillators per unit volume, e is the unitary electric charge, ε_0 is the dielectric constant in vacuum, m is the mass of the oscillators and $\omega_0 = 2\pi\nu_0$ is the transition center frequency. γ is the natural linewidth. This factor, accounting for the spontaneous emission, is related to the Einstein coefficients as follows:

$$\gamma = A_{21} = \frac{8\pi h}{c^3}\nu^3 B_{21} \qquad (1.11)$$

where A_{21} and B_{21} are the Einstein coefficients for the spontaneous and the stimulated emission respectively. Another contribution to the homogeneous broadening is due to the *transit time*, given by the finite time that the molecules spend within the laser beam section, expressed as follows [39]:

$$\gamma_t = \frac{1}{w}\sqrt{\frac{\ln 2}{\pi}\frac{k_B T}{m}} \qquad (1.12)$$

with m molecular mass and w beam waist. Finally it is worth mentioning the homogeneous broadening contribution due to *collisions*, the so-called *pressure broadening*.

On the other hand, if the probability of absorption depends on a property of the single molecule, the line is said to be *inhomogeneously broadened*. The most important example of inhomogeneous line broadening is *Doppler broadening*. In this case, the probability of absorption of monochromatic radiation depends on the velocity of the single molecules. Since the velocity distribution in a sample in thermal-equilibrium conditions follows the Boltzmann statistics, the shape of pure inhomogeneously broadened absorption lines is *Gaussian*, with a FWHM given by

$$\Delta\nu_D = \frac{\nu_0}{c}\sqrt{8\ln 2 \frac{k_B T}{m}} \qquad (1.13)$$

This width depends linearly on the frequency ν_0, but only under square root on the ratio between the temperature and the molecular mass, there-

---

[10]This version of the equations holds close to an absorption line, where $|\omega - \omega_0| \ll \omega_0$.

fore only a major cooling of the sample can appreciably reduce it.

In order to understand how the two broadening mechanisms interact to give the real line shape, we can divide the molecules in the same initial state into subgroups, such that all molecules with a velocity component within the interval v_z to $v_z + \Delta v_z$ belong to one subgroup. If we choose $\Delta v_z = \gamma/k$, where k is the wavenumber, we may consider the frequency interval γ to be homogeneously broadened inside the much larger inhomogeneous Doppler width. To be more explicit, we can say that all molecules in the subgroup can absorb or emit radiation with frequency $\nu = \nu_0 + v_z k$. This happens because in the moving molecules reference frame this frequency falls within the natural width γ around ν_0. The resulting line shape is a convolution between the two, a so-called *Voigt profile*.

1.1.5 Linear and non-linear absorption

Taking advantage of the so-called *non-linear absorption spectroscopy techniques*, it is possible to get rid of the Doppler broadening. They take advantage of the *saturation phenomenon*, i.e. the fact that the absorption coefficient of a gaseous sample is not constant but at a certain point it starts to decrease with increasing optical power. In order to understand the saturation phenomenon, we start by studying the absorption with respect to optical intensity [40]. For a monochromatic plane lightwave defined as

$$E = E_0 \cos(\omega t - kz + \varphi) \tag{1.14}$$

we define the mean intensity as

$$I = \frac{1}{2} c \varepsilon_0 E_0^2 \tag{1.15}$$

The power absorbed in a volume $dV = A \, dz$ is

$$dP = -P_0 \alpha \, dz = -A I \sigma \Delta N \, dz \tag{1.16}$$

where A is the cross-section of the illuminated area, ΔN is the difference of the population densities of the upper and lower levels, and σ is the absorption cross section. If P_0 is sufficiently low, ΔN and α can be considered constant, otherwise their dependence on P_0 becomes important. Actually, the intensity distribution of the plane wave in frequency is not a

delta function, therefore a spectral intensity I_ν can be defined as follows:

$$I = \int I_\nu \, d\nu \approx I_\nu(\nu_0)\delta\nu_L \tag{1.17}$$

where $\delta\nu_L$ is the I_ν FWHM. The absorbed power is then

$$dP = \Delta N \, dV \int I_\nu \sigma(\nu) \, d\nu \tag{1.18}$$

where $\sigma(\nu)$ has the shape of the absorption with a FWHM $\delta\nu_a$. If $\delta\nu_a < \delta\nu_L$ the expression for the absorbed power is

$$dP = \Delta N \, dV I(\nu_0)\sigma(\nu_0)\frac{\delta\nu_a}{\delta\nu_L} \tag{1.19}$$

This shows that for spectroscopy purposes what counts is the spectral intensity I_ν and its width, more then the intensity. In particular, it is important to have laser sources narrower in frequency than the absorptions, since the spectral portion of the optical power that falls outside the absorption line does not contribute to the detection.

The population difference in saturation conditions is given by

$$\Delta N = \frac{\Delta N_0}{1 + S} \tag{1.20}$$

with $S = I/I_s$, where I_s is the saturation intensity given by the stimulated absorption Einstein coefficient and the relaxation rates, while if $\delta\nu_a > \delta\nu_L$, the absorbed power is

$$dP = dV I(\nu_0)\sigma(\nu_0)\frac{\Delta N_0}{1 + S} \tag{1.21}$$

and if the only relaxation process is spontaneous emission, the saturation intensity can be expressed as

$$I_s = \frac{2h}{c^2}\nu^3 A_{21} \tag{1.22}$$

If pressure is low enough the transition probability due to collisions is negligible respect to A_{21}.

The saturation of homogeneously broadened transitions with Lorentzian profiles gives again a Lorentzian profiles with a FWHM

$$\Delta\nu_s = \Delta\nu_0\sqrt{1 + S(\nu_0)} \tag{1.23}$$

and the absorption coefficient results

$$\alpha(\nu) = \frac{\alpha_0(\nu)}{1 + S(\nu)} \tag{1.24}$$

with $\alpha_0(\nu)$ unsaturated absorption coefficient. When a monochromatic wave of the form given by eq. 1.14 passes through a gas in thermal equilibrium, only those molecules with a certain velocity v_z such that in their reference frame the wave frequency results in resonance within the natural width contribute to absorption. The absorption cross section is given by

$$\sigma(\omega - \omega_0 - kv_z) = \sigma_0 \frac{(\gamma/2)^2}{(\omega - \omega_0 - kv_z)^2 + (\gamma/2)^2} \tag{1.25}$$

but even though a hole in the population difference is burned, the absorption coefficient still shows a Voigt profile (as in the non-saturated case)

$$\alpha(\nu) = \frac{\alpha_0(\nu)}{1 + S(\nu_0)} \tag{1.26}$$

and that hole is not detectable.

1.1.6 Saturation spectroscopy

That hole becomes detectable using two *counterpropagating* beams in a so-called *saturation spectroscopy* scheme. The first powerful beam is called *pump beam* and indicated by the wave vector $\vec{k}_1$, the second weak beam is called *probe beam* and indicated by the wave vector $\vec{k}_2$. The probe beam is the one which is detected. Many experimental schemes have been thought and realized, here we will study the one where the second beam is just obtained from the first one using a partial reflector (see fig. 1.3).[11] Since they are counterpropagating, we have $k_{z2} = -k_{z1}$. Now in the absorption coefficient $\alpha(\omega)$ there are two absorption cross-section contributions, $\sigma(\omega - \omega_0 - kv_z)$ and $\sigma(\omega - \omega_0 + kv_z)$. If $S(\nu_0) \ll 1$ we have

$$\alpha_s(\omega) = \alpha_0(\omega) \left[1 - \frac{S(\nu_0)}{2} \frac{(\gamma_s/2)^2}{(\omega - \omega_0)^2 + (\Gamma_s/2)^2} \right] \tag{1.27}$$

---

[11] The most known are with two frequency independent beams (fix pump and tunable probe), or with both the beams having the same optical power (e.g. in intracavity spectroscopy).
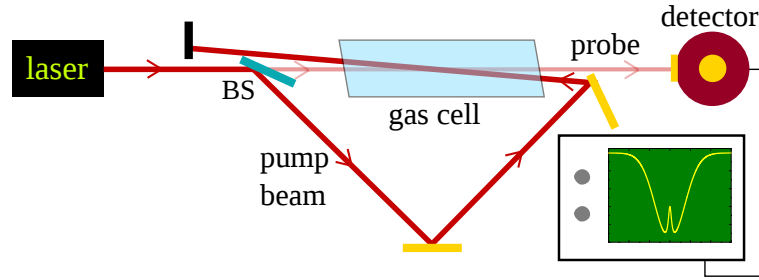
Figure 1.3: Saturation spectroscopy scheme. The beam splitter (BS) splits the main beam in a probe beam (the transmitted one) and a pump beam (the reflected one). In these conditions the pump beam saturates the sample and a Lamb dip is observed on the Doppler-broadened absorption profile.

where $\Gamma_s = (\gamma + \gamma_s)/2$ and $\gamma_s = \gamma\sqrt{1 + S(\nu_0)}$. Now the absorption coefficient shows a Lorentzian dip for $\omega = \omega_0$. In order to understand the formation of a Lamb dip, we consider that for $\omega \neq \omega_0$ the pump radiation is absorbed by the class of molecules with the velocity component $v_z = +(\omega - \omega_0 \mp \gamma_s/2)/k$, while the probe radiation by the unperturbed class of molecules with $v_z = -(\omega - \omega_0 \pm \gamma_s/2)/k$. For $\omega = \omega_0$ both the waves are absorbed by the same class of molecules $v_z = (0 \pm \gamma_s/2)/k$, which is the one having zero component of the velocity along the wave propagation axis. The pump beam, which is the most intense, saturates the absorption of the sample for that class and the absorption of the probe beam is significantly reduced.

Saturation spectroscopy is a very useful technique since it enables the detection of transitions with natural broadening even at room temperature, but it shows some limitations:

- Whatever chopping technique is used to get rid of the Doppler background, the whole probe beam intensity is shined on the detector, limiting the signal-to-noise ratio.

- The shape of the line is Lorentzian, therefore on the center of the transmission the signal function has a local maximum (or minimum). For this reason this signal cannot be directly used to lock a laser.

As we will see, the polarization spectroscopy technique allows to overcome these limitations.

1.1.7 Polarization spectroscopy

Polarization spectroscopy was reported for the first time in 1976 by Wieman and Hänsch [35] as an evolution of the standard saturation spectroscopy. The technique is based on the fact that the pump beam can also induce a change in the polarization of the probe beam. Again the two beams come from the same laser, but now, using proper wave plates and polarizers, the pump is made *circularly polarized*, while the probe is linearly polarized.[12] We assume that the involved transition is a molecular ro-vibrational transition belonging to the *R* or the *P* branch. If the pump beam is σ^+ polarized, the selection rule on the projection of the angular momentum *J* states $\Delta M = +1$. For this reason the pump beam saturates the transition *unbalancing* at the same time the population among the $2J + 1$ degenerate rotational sublevels. In this way the sample becomes *birefringent*. The linear probe beam can be thought to be composed of two balanced circularly polarized components σ^+ and σ^-. Clearly such an induced birefringent sample unbalances the two components, resulting in a probe beam with a *rotated polarization*. Now, to be able to detect the probe beam only when the polarization is rotated it is sufficient to add a *polarizer* at the end of the path (named *analyzer*) just before the detector, with a transmission axis perpendicular to the polarization axis of the unperturbed probe beam. Clearly the same principle that holds for saturation spectroscopy still holds in this case. This rotation effect happens only for those molecules that are simultaneously in resonance with both the beams (within the natural width), i.e. for those molecules whose velocity component on the beam direction is zero. This is the fact that enables Doppler-free detection. To be more quantitative deriving the polarization signal [40], we start writing the linearly polarized probe wave as

$$\vec{E} = E_0 \hat{x} e^{i(\omega t - kz)} \tag{1.28}$$

---

[12] As an alternative, the pump beam can be linearly polarized, with the axis 45° rotated respect to the probe beam. This configuration gives different spectroscopic line shapes.

It can be expanded on the two circular polarizations σ^+ and σ^- as $\vec{E} = \vec{E}^+ + \vec{E}^-$, where

$$\vec{E}^+ = \frac{1}{2}E_0(\hat{x} + \mathrm{i}\hat{y})\,\mathrm{e}^{\mathrm{i}(\omega t - k^+ z)} \tag{1.29a}$$

$$\vec{E}^- = \frac{1}{2}E_0(\hat{x} - \mathrm{i}\hat{y})\,\mathrm{e}^{\mathrm{i}(\omega t - k^- z)} \tag{1.29b}$$

with $\hat{x}$ and $\hat{y}$ unit vectors identifying the axis. The σ^+-polarized pump beam causes a non-isotropic saturation of the sample, therefore the absorption coefficient and the refractive index experienced by the two polarizations are different. Passing through the sample for a length L the two polarizations result

$$\vec{E}^+ = \frac{1}{2}E_0(\hat{x} + \mathrm{i}\hat{y})\,\mathrm{e}^{\mathrm{i}[\omega t - k^+ L + \mathrm{i}(\alpha^+/2)L]} \tag{1.30a}$$

$$\vec{E}^- = \frac{1}{2}E_0(\hat{x} - \mathrm{i}\hat{y})\,\mathrm{e}^{\mathrm{i}[\omega t - k^- L + \mathrm{i}(\alpha^-/2)L]} \tag{1.30b}$$

The non-isotropic saturation gives a phase difference

$$\Delta\varphi = (k^+ - k^-)L = \frac{\omega L}{c}\Delta n \tag{1.31}$$

where $\Delta n = n^+ - n^-$. Moreover an amplitude difference is also developed:

$$\Delta E = \frac{E_0}{2}\left[\mathrm{e}^{-(\alpha^+/2)L} - \mathrm{e}^{-(\alpha^-/2)L}\right] \tag{1.32}$$

After the sample (for $z = L$) the two polarization components give an elliptically polarized wave:[13]

$$\vec{E}(L) = \vec{E}^+ + \vec{E}^- = \frac{1}{2}E_0\,\mathrm{e}^{\mathrm{i}\omega t}\,\mathrm{e}^{-\mathrm{i}[\omega n L/c - \mathrm{i}\alpha L/2]}\left[(\hat{x} + \mathrm{i}\hat{y})\,\mathrm{e}^{-\mathrm{i}\Lambda} + (\hat{x} - \mathrm{i}\hat{y})\,\mathrm{e}^{+\mathrm{i}\Lambda}\right] \tag{1.33}$$

with $n = (n^+ + n^-)/2$, $\alpha = (\alpha^+ + \alpha^-)/2$ and

$$\Lambda = \frac{\omega L \Delta n}{2c} - \mathrm{i}\frac{L\Delta\alpha}{4} \tag{1.34}$$

If the transmission axis of the analyzer is tilted respect to $\hat{y}$ of a small angle ϑ, the transmitted amplitude becomes

$$E_t = E_x \sin\vartheta + E_y \cos\vartheta \tag{1.35}$$

---

[13]For a complete discussion the absorption and the pressure-induced birefringence of the windows of the gas cell should be considered [40].

The transmitted amplitude is then

$$
\begin{aligned}
E_t &= E_0 \, \mathrm{e}^{\mathrm{i}\,\omega t} \, \mathrm{e}^{-\mathrm{i}[\omega n L/c - \mathrm{i}\alpha L/2]} (\sin\vartheta \cos\Lambda + \cos\vartheta \sin\Lambda) \\
&= E_0 \, \mathrm{e}^{\mathrm{i}\,\omega t} \, \mathrm{e}^{-\mathrm{i}[\omega n L/c - \mathrm{i}\alpha L/2]} [\sin(\vartheta + \Lambda)]
\end{aligned}
\tag{1.36}
$$

The detected signal is proportional to the transmitted intensity

$$
S(\omega) \propto I_t(\omega) = c\varepsilon_0 E_t E_t^*
\tag{1.37}
$$

The $\Delta\alpha$ line profile is Lorentzian, as for saturation spectroscopy, therefore we can define

$$
\Delta\alpha(\omega) = \frac{\Delta\alpha_0}{1 + x^2}, \ \text{ with } x = \frac{\omega_0 - \omega}{\gamma_s/2}
\tag{1.38}
$$

and $\alpha_0 = \alpha(\omega_0)$. The Kramers-Kronig equations (1.10) relate the refractive index and the absorption coefficient, yielding

$$
\Delta n(\omega) = \frac{c}{\omega_0} \Delta\alpha_0 \frac{x}{1 + x^2}
\tag{1.39}
$$

At the end, using eqs. 1.36–1.39 and expanding them considering that all factors in Λ and the ϑ angle are small, we obtain the detected signal

$$
I_t(\omega) = I_0 \, \mathrm{e}^{-\alpha L} \left[\vartheta^2 + \underbrace{\vartheta \Delta\alpha_0 \, L \frac{x}{1 + x^2}}_{\text{dispersive}} + \underbrace{\left(\frac{\Delta\alpha_0 \, L}{4}\right)^2 \frac{1}{1 + x^2}}_{\text{Lorentzian}} + \frac{3}{4} \left(\frac{\Delta\alpha_0 \, x}{1 + x^2}\right)^2 \right]
\tag{1.40}
$$

Now a *dispersive* term is present. It is centered around ω_0 and its magnitude depends on the angle ϑ. Tuning properly this angle, the dispersive term can be maximized, being greater than the other frequency-dependent terms. Unfortunately, a constant term proportional to ϑ is present, giving an unwanted background to the signal. A smart way to get rid of this background is to rotate the analyzer setting $\vartheta \approx \pi/4$, and detect both the transmitted and the reflected components in a *differential-detection* scheme.[14] Now

$$
S(\omega) \propto I_t(\omega) - I_r(\omega) = I_0 \, \mathrm{e}^{-\alpha L} [|\sin(\vartheta + \Lambda)|^2 - |\cos(\vartheta + \Lambda)|^2]
\tag{1.41}
$$

---

[14]See fig. 2.1 for a schematic representation and ref. [41] for an application.

Setting $\vartheta = \pi/4$ and expanding for $\Lambda \ll 1$ we obtain

$$S(\omega) \propto 2I_0 \, e^{-\alpha L} \, \text{Re}[\Lambda] = I_0 \, e^{-\alpha L} \, \Delta\alpha_0 \, L \, \frac{x}{1+x^2} \qquad (1.42)$$

In this way a background-free dispersive signal centered on the transition is obtained. With this configuration (circular pump) transitions belonging tho the R or the P branches give more intense signals, while transitions belonging tho the Q branch give weaker signals.[15]

1.2   Non-linear phenomena

Non-linear phenomena are at the basis of a large number of optical techniques and technologies. This section deals with this topic. Firstly, a general discussion starting with Maxwell's equations introduces the non-linear polarization (section 1.2.1). Then, in sections 1.2.2 and 1.2.4 non-linear second-order and third-order phenomena, such as second-harmonic generation, sum-frequency generation, difference-frequency generation, third-harmonic generation, four-wave mixing and the Kerr effect, are introduced, with a side discussion on the phase-matching condition and bandwidth (section 1.2.3).

1.2.1   Non-linear polarization

Maxwell's equations can describe the electromagnetic field evolution in every condition, in vacuum as well as in matter. In the version reported below [42], they are valid far away from electrical charges and currents:

$$\vec{\nabla} \wedge \vec{E} = -\frac{\partial}{\partial t}\vec{B} \qquad (1.43\text{a})$$

$$\vec{\nabla} \wedge \vec{H} = \frac{\partial}{\partial t}\vec{D} \qquad (1.43\text{b})$$

$$\vec{\nabla} \cdot \vec{D} = 0 \qquad (1.43\text{c})$$

$$\vec{\nabla} \cdot \vec{B} = 0 \qquad (1.43\text{d})$$

where $\vec{E} = \vec{E}(\vec{r},t)$ and $\vec{H} = \vec{H}(\vec{r},t)$ are the electric and the magnetizing field, respectively. The two vectors $\vec{D} = \vec{D}(\vec{r},t)$ and $\vec{B} = \vec{B}(\vec{r},t)$, respectively the displacement field and the magnetic field, are related to the

---

[15]The opposite holds if the pump is linearly polarized.

main fields through the relations

$$\vec{D} = \varepsilon_0 \vec{E} + \vec{P} \tag{1.44a}$$

$$\vec{B} = \mu \vec{H} + \vec{M} \tag{1.44b}$$

where $\vec{P} = \vec{P}(\vec{E})$ and $\vec{M}$ are the electric polarization vector and the magnetization vector respectively, while ε_0 is the dielectric constant in vacuum and μ is the magnetic permeability constant. Since we are going to deal with non-magnetic samples, we impose $\vec{M} = 0$.

Usually, in-lab generated fields are way weaker respect to the ones that bound electrons to molecules. Therefore the *polarization vector* can be expanded in series respect to the electric field, yielding

$$\vec{P} = \varepsilon_0 \chi(\vec{E}) \vec{E} = \varepsilon_0 (\chi^{(1)} \vec{E} + \chi^{(2)} \vec{E}^2 + \chi^{(3)} \vec{E}^3 + \dots) \tag{1.45a}$$

with $\chi(\vec{E})$ *dielectric susceptibility* and $\chi^{(i)} = \chi^{(i)}(\vec{E})$ ith susceptibility coefficient. The second-order coefficient is non-vanishing only for acentric crystals, i.e. for crystals without a center of symmetry.

Eq. 1.45a can be expressed in tensorial form[16] as follows:

$$P_k(\vec{r},t) = \varepsilon_0 (\chi_{kl}^{(1)} E_l + \chi_{klm}^{(2)} E_l E_m + \chi_{klmn}^{(3)} E_l E_m E_n + \dots) \tag{1.45b}$$

where P_k is the kth component of the polarization. The indexes l m n run over the three spatial coordinates x y z, while

$$\chi_{1,2,\dots,i+1}^{(i)} = \frac{1}{i! \varepsilon_0} \frac{\partial^i P_1}{\partial E_2 \partial E_3 \dots \partial E_{i+1}} \tag{1.46}$$

For standard dielectric materials the permanent dipole moment is zero. If in the polarization expression we separate the linear terms in the field from the non-linear ones we obtain [43]

$$\vec{P}(\vec{r},t) = \varepsilon_0 \chi^{(1)} \vec{E}(\vec{r},t) + \vec{P}_{(\text{NL})}(\vec{r},t) \tag{1.47}$$

Combining eqs. 1.43b, 1.44a and 1.47 we obtain

$$\vec{\nabla} \wedge \vec{H} = \varepsilon \frac{\partial}{\partial t} \vec{E} + \frac{\partial}{\partial t} \vec{P}_{(\text{NL})} \tag{1.48}$$

---

[16]Here the Einstein summation convention is adopted. The summation over repeated indexes is implied.

with $\varepsilon = \varepsilon_0(1 + \chi^{(1)})$. Recalling the identity

$$\vec{\nabla} \wedge \vec{\nabla} \wedge \vec{E} = \vec{\nabla}(\vec{\nabla} \cdot \vec{E}) - \nabla^2 \vec{E} \qquad (1.49)$$

and assuming

$$\vec{\nabla} \cdot \vec{E} = 0 \qquad (1.50)$$

the curl of both the terms in eq. 1.43a can be evaluated, obtaining the *wave equation*

$$\nabla^2 \vec{E} = \mu\,\varepsilon\,\frac{\partial^2}{\partial t^2}\vec{E} + \mu\,\frac{\partial^2}{\partial t^2}\vec{P}_{(\mathrm{NL})} \qquad (1.51a)$$

In order to simplify the discussion we can assume $\vec{P}_{(\mathrm{NL})} \parallel \vec{E}$, yielding the wave equation in scalar form

$$\nabla^2 E = \mu\,\varepsilon\,\frac{\partial^2}{\partial t^2}E + \mu\,\frac{\partial^2}{\partial t^2}P_{(\mathrm{NL})} \qquad (1.51b)$$

We consider now an electric field made of several plane waves, propagating along the z axis with angular frequencies ω_i:

$$E(z,t) = \sum_i \frac{1}{2}[E_i(z)\ \mathrm{e}^{\mathrm{i}(\omega_i t - k_i z)} + c.c.] \qquad (1.52)$$

Replacing eq. 1.52 in eq. 1.51b we understand how the non-linear term *mixes* the components at different frequencies.[17]

1.2.2 Second-order non-linear phenomena

For the interpretation of second-order non-linear phenomena, only the second-order term in eq. 1.45 must be considered, as well as only three plane waves ($i = 1, 2, 3$ in eq. 1.52, where $i = 2, 3$ are the sources, $i = 1$ is the generated one). Evaluating now $P^{(2)}$ we find terms oscillating at $2\omega_2$ (*second-harmonic generation -* SHG), $\omega_2 + \omega_3$ (*sum-frequency generation -* SFG), and $|\omega_2 - \omega_3|$ (*difference-frequency generation -* DFG), capable of generating new field at ω_1. The relation among the frequencies is given by the conservation of energy law applied to photons. Now we can rewrite eq. 1.51b for the field oscillating at ω_1 and evaluate the term $\nabla^2 E^{(\omega_1)}$ according to eq. 1.52. Neglecting the second derivative of the field respect to z, and recalling that $k_1^2 = \omega_1^2\,\mu\,\varepsilon_1$, with $\varepsilon_1 = \varepsilon(\omega_1)$,

---

[17]This mixing takes place since the field is multiplied by itself, therefore terms related to different frequencies multiplies among each other. See eq. 1.45.

we obtain

$$\frac{d}{dz}E_1 = -i\omega_1\sqrt{\frac{\mu}{\varepsilon_1}}\, d^{(\omega_3,\omega_2)}E_3 E_2^*\, e^{-i\Delta k\, z} \tag{1.53}$$

where $d^{(\omega)}$ is the value of the non-linear constant defined as $d_{lmn} = \frac{1}{2}\varepsilon_0\chi^{(2)}_{lmn}$, obtained evaluating the sum over the indexes l,m in eq. 1.45b for a certain geometry of the involved fields. Eq. 1.53 describes the variation of the generated field along the generating path. For the other two fields similar expressions hold, and the three amplitudes are coupled through the non-linear constants $d^{(\omega)}$. Eq. 1.53 by itself can describe second-order non-linear phenomena as long as the conversion efficiency is low, i.e. the source fields are not significantly depleted. We now integrate it assuming that the two fields E_2 and E_3 hit a non-linear crystal side, and on that side $E_1(z=0)=0$. For the DFG process the conservation of energy gives

$$\omega_1 = \omega_3 - \omega_2 \tag{1.54}$$

and we define the *phase-mismatch factor* as[18]

$$\Delta k = k_1 - (k_3 - k_2) = k_1 - k_3 + k_2 \tag{1.55}$$

We can now integrate eq. 1.53 along the crystal length l, obtaining

$$E_1(l) = -i\omega_1\sqrt{\frac{\mu}{\varepsilon_1}}\, d\, E_3 E_2^* \frac{e^{i\Delta k\, l}-1}{i\Delta k} \tag{1.56}$$

The related intensity is

$$I(l) = E_1(l)E_1^*(l)\sqrt{\frac{\varepsilon_1}{\mu}} = \sqrt{\frac{\mu}{\varepsilon_1}}\frac{\omega_1^2 d^2}{n_1^2}\,|E_3|^2|E_2|^2\, l^2\, \frac{\sin^2\left(l\Delta k/2\right)}{(l\Delta k/2)^2} \tag{1.57}$$

where $n_1 = n(\omega_1) = \varepsilon_1/\varepsilon_0$ is the refractive index of the material.

1.2.3 Phase matching

Eq. 1.57 clearly shows that the generated power is proportional to the function

$$\text{sinc}^2\left(\frac{l\Delta k}{2}\right) = \frac{\sin^2(l\Delta k/2)}{(l\Delta k/2)^2} \xrightarrow[\Delta k\to 0]{} 1 \tag{1.58}$$

---

[18]For the other processes the phase-mismatch factor is defined in the same way with just a different distribution of the signs.

If the *phase-matching condition* $\Delta k = 0$ is satisfied, the generated power increases quadratically[19] with l, otherwise it simply oscillates with a spatial period given by $l_c = \pi/\Delta k$, the so-called *coherence length* (see fig. 1.4). There are two techniques to fulfill the phase-matching condition:
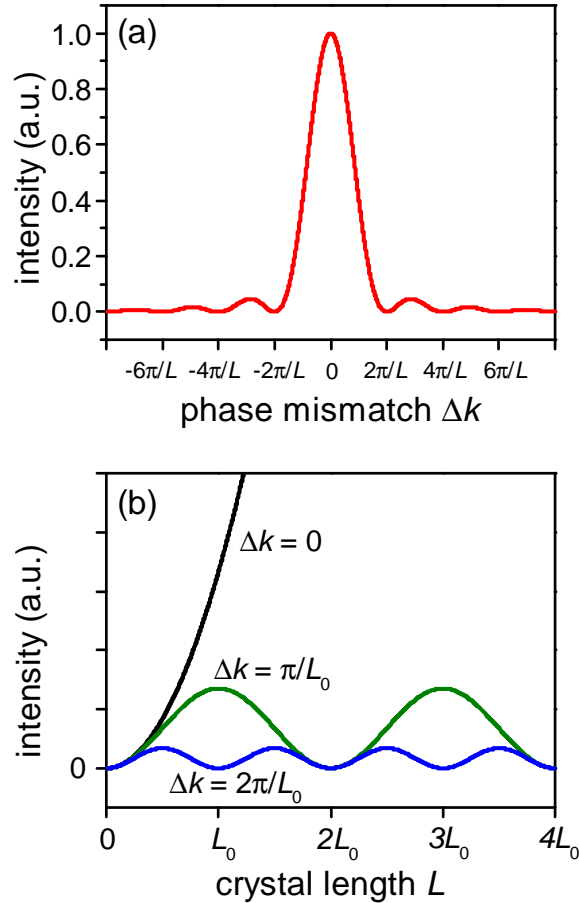

Figure 1.4: Phase-matching curves. **a)** Phase-matching curve (eq. 1.58) as a function of the phase-mismatch factor Δk, with a fixed crystal length $l = L$.
b) Generated power (eq. 1.57) as a function of the crystal length l, with different fixed values of the phase-mismatch factor Δk. The length is expressed in terms of a reference L_0.

- One takes advantage of the natural birefringence of anisotropic crystals and for this reason it is named *birefringent phase matching*. If we consider the case of uniaxial crystals, characterized by a single symmetry axis, and we consider to hit the crystal with waves

---

[19]This result holds since we have considered plane waves. If we consider that the incident waves are focused Gaussian beams, we obtain that the generated power increases linearly with l.

whose wave vectors are perpendicular to that axis, we have that the waves experience two different refractive indexes, depending whether the electric field is perpendicular (ordinary polarization) or parallel (extraordinary polarization) to the symmetry axis. The first one is the *ordinary refractive index n_o*, while the second one is the *extraordinary refractive index $n_e = n_e(\vartheta)$*, which depends on the angle ϑ between the wave vector and the symmetry axis [44]. In order to simplify the discussion we assume that all the wave vectors are parallel to each other and $k_i = k(\omega_i) = \omega_i n_i / c$. Now the phase-matching condition reads

$$\omega_1 n_o(\omega_1) = \omega_3 n_e(\omega_3, \vartheta) - \omega_2 n_o(\omega_2) \qquad (1.59)$$

where we have assumed E_1 and E_2 ordinarily polarized, while E_3 extraordinarily polarized. By properly adjusting the angle ϑ the phase-matching condition can be satisfied.

- The other one, the so-called *quasi phase matching*, takes advantage of the possibility of periodically reverting one of the principal optical axis of the crystal, resulting in a *modulation* of the sign of the non-linear constant d. If this modulation has the proper spatial period $\Lambda = l_c$, the generated power still oscillates, but *increasing* at every oscillation, like a stairs. Formally, we can rewrite the new phase-matching condition as follows:

$$\Delta k' = k_3 - k_2 - k_1 - \frac{2\pi}{\Lambda} = 0 \qquad (1.60)$$

Now the parameter that has to be properly chosen is Λ, a constructive feature that can also be slightly adjusted with temperature.

The advantages of the quasi phase matching are an overall higher conversion efficiency and a higher flexibility in reaching the phase-matching condition.

For these conversion processes, an important parameter that has to be taken into account is the *phase-matching bandwidth*, i.e. fixing the phase-matching condition, how much the frequency of the generated radiation can be tuned still having an appreciable amount of power. Supposing that the tunable frequency is ω_2, we use eq. 1.54 to rewrite the phase-mismatch factor (eq. 1.55) expressing it in terms of the other

two frequencies, obtaining[20]

$$\omega_3(n_3 - n_2) + \omega_1(n_2 - n_1) - \frac{2\pi c}{\Lambda} = c\Delta k \qquad (1.61)$$

with $n_i = n(\omega_i)$. Observing the phase-mismatch function (eq. 1.58 and fig. 1.4), we can assume as a limit for the generation its first zero, i.e. $l\Delta k/2 = \pi$, yielding for the crystal length $L < 2\pi/\Delta k = 2l_c$. The bandwidth of the generated radiation at ω_1 is now obtained subtracting member by member eq. 1.61, once in phase-matching condition $\Delta k = 0$ and then in the limit condition $\Delta k = 2\pi/L$, and finally multiplying the result by 2 since the sinc function is symmetrical. The result is

$$\Delta\nu_1 = \frac{2c}{L\,\Delta n_{21}} \qquad (1.62)$$

This result depends only on the difference of the refractive indexes $\Delta n_{21} = n_2 - n_1$ and the crystal length L.

1.2.4 Third-order non-linear phenomena

For the interpretation of third-order non-linear phenomena, the third-order term in eq. 1.45 must be considered, as well as four plane waves ($i = 1, 2, 3, 4$ in eq. 1.52). The third-order susceptibility $\chi^{(3)}_{klmn}$ is a fourth-rank tensor, with 81 elements [45]. For crystals with low symmetry all the terms are independent and can be nonzero. On the other hand, for high-symmetry materials the number of independent elements is significantly reduced. For isotropic materials the independent elements are only three. Evaluating now $P^{(3)}$ we find terms oscillating at $3\omega_2$ (*third-harmonic generation*), $\omega_2 + \omega_3 + \omega_4$ (*sum-frequency generation*), and $|\omega_2 + \omega_3 - \omega_4|$ and permutations (*four-wave mixing - FWM*), capable of generating new field at ω_1. The relation among the frequencies is again given by the conservation of energy. With a discussion similar to the one adopted in section 1.2.2, an expression equivalent to eq. 1.53 can

---

[20]Compare eqs. 1.59 and 1.60.

be retrieved:

$$
\begin{aligned}
\frac{\mathrm{d}}{\mathrm{d}z}E_1 = -\mathrm{i}\frac{\omega_1^2\mu\varepsilon_0\chi^{(3)}}{8k_1}\Bigg[& \underbrace{6E_3E_4E_2^*\,\mathrm{e}^{-\mathrm{i}\Delta k\,z}}_{\text{four-wave mixing}} \\
& + \underbrace{6E_1\left(\frac{1}{2}|E_1|^2+|E_2|^2+|E_3|^2+|E_4|^2\right)}_{\text{Kerr}}\Bigg]
\end{aligned}
\tag{1.63}
$$

For the other three fields similar expressions hold, and the four amplitudes are coupled through the $\chi^{(3)}$ parameter. The *four-wave mixing term* comes from the mixing of the other three waves. The factor 6 in front of it comes from the degeneracy given by the interchangeability of the three fields. On the other hand, the *Kerr term* comes from the sum of the *intensities* of the other fields and only modifies the propagation constant of the same wave. It causes the arising of a change of the refractive index according to the following equation:

$$
n(I) = n_0 + n_2(I_2 + I_3 + I_4)
\tag{1.64}
$$

Eq. 1.63 can be integrated and the intensity can be computed, yielding a dependency from the phase-mismatch factor Δk of the same type of eq. 1.58, with a related phase-matching bandwidth.

1.3 Optical frequency combs

Optical frequency combs (OFCs) are laser spectra made of perfectly equispaced and locked longitudinal modes. The *mode-locking mechanism* takes care of turning the group of independent modes into a set of modes with fixed reciprocal phases and mode spacing. The frequency components of such a spectrum can then be expressed as follows:

$$
\nu_N = N\,f_s + f_o
\tag{1.65}
$$

where f_s is the *spacing*, f_o is the *offset frequency*, while N is a large integer.[21] According to eq. 1.65, when mode locking is effective only two degrees of freedom survive.

---

[21]Here we have used the following notation: ν for optical frequencies, f for radio-frequencies.

In the following sections the mode-locking mechanism is described in its versions, the active and passive amplitude-modulation mode locking (sections 1.3.1 and 1.3.2), and the frequency-modulation mode locking (section 1.3.3). In order to have a metrological OFC for high-resolution and precision spectroscopy measurements, it is fundamental to measure and stabilize both the parameters defined in eq. 1.65. A brief discussion about this aspect is presented in section 1.3.4.

1.3.1 Amplitude-modulation mode locking

The classical way to achieve mode locking takes advantage of a *modulation* of intracavity *losses*. If this modulation is induced by an external mechanism respect to the lasing, the mode locking is named *active*. On the other hand, if the modulation is spontaneous, it is named *passive*. In mode-locked operating regime, the lasers emit pulses which are very short in time,[22] and the repetition rate f_r is given by the length of the laser cavity.[23] As in any optical resonator, the laser mode spacing is given by

$$f_s = \frac{c}{rnL} \tag{1.66}$$

where n is the refractive index and L is the length of the cavity. The factor r depends whether the laser cavity is linear ($r = 2$) or ring ($r = 1$). For pulsed mode-locked lasers the equality $f_s = f_r$ holds.

In order to explain the mode-locking mechanism [46], we start expressing the intracavity electric field at any fixed point as

$$E(t) = \sum_{i=-m/2}^{+m/2} E_i e^{i[2\pi(\nu_0 + if_s)t + \varphi_i]} \tag{1.67}$$

where m is the total number of lasing modes, while ν_0 is the carrier frequency. φ_i is the phase of the i-th mode. An important property of $E(t)$ expressed in these terms is its periodicity in $T_r = 1/f_s$, the round-trip

---

[22]Usually the pulse width is on the scale of picoseconds and can reach the femtoseconds level.

[23]Usually the pulse repetition rate spans from hundreds of megahertz to few tens of gigahertz.

transit time within the cavity:

$$
\begin{aligned}
E(t + T_r) &= \sum_i E_i \, e^{i[2\pi(\nu_0 + if_s)(t + 1/f_s) + \varphi_i]} \\
&= \sum_i E_i \, e^{i[2\pi(\nu_0 + if_s)t + \varphi_i]} \underbrace{e^{i 2\pi(\nu_0/f_s + i)}}_{=1} \\
&= E(t)
\end{aligned}
\tag{1.68}
$$

because ν_0/f_s is an integer. This result holds as long as the phases φ_i are fixed. The mode-locking mechanism takes care of keeping these phases fixed. A particular form of mode locking consist in having all the phases vanishing[24] ($\varphi_i = 0$). Moreover, taking $E_i = E_0$, eq. 1.67 gives

$$
E(t) = E_0 \sum_{i=-m/2}^{+m/2} e^{i 2\pi(\nu_0 + if_s)t} = E_0 \, e^{i 2\pi\nu_0 t} \frac{\sin(m\pi f_s t)}{\sin(\pi f_s t)}
\tag{1.69}
$$

The laser output power is proportional to

$$
P(t) \propto |E(t)|^2 = E_0^2 \frac{\sin^2(m\pi f_s t)}{\sin^2(\pi f_s t)}
\tag{1.70}
$$

A number of properties can be inferred from eqs. 1.69 and 1.70:

- The emitted power is made of a *train of pulses* with a periodicity $T_r = 1/f_s$.

- The peak power is equal to m times the average power.

- The peak field amplitude is equal to m times the single-mode amplitude.

- The individual pulse width, defined as the time difference between the peak and the first zero, is

$$
\tau_0 = \frac{T_r}{m} = \frac{1}{m f_s} \approx \frac{1}{\Delta\nu}
\tag{1.71}
$$

  where $\Delta\nu$ is the laser gain bandwidth.

A schematic is reported in fig. 1.5. This discussion shows what happens at a fixed position. Considering what happens along the laser cavity, we

---

[24] Actually this corresponds to have all the phases equal, then this unique phase can be reabsorbed without any loss of generality.
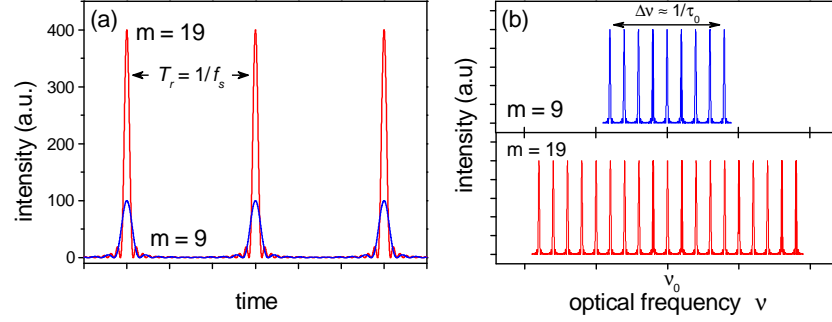
Figure 1.5: In this figure comb pulses generated by an ideal laser with 9 and 19 locked modes lasing are depicted. **a)** Optical pulses in time domain. **b)** Related modes in frequency domain.

have a traveling pulse passing at a certain position every $\Delta t = T_r$, with a spatial length

$$l_0 \approx c\,\tau_0 = c\,\frac{T_r}{m} = \frac{rnL}{m} \qquad (1.72)$$

Despite what stated by eq. 1.70, the actual shape of the pulses is usually close to – and it is always approximated with – a Gaussian bell.[25]

In order to understand how a modulation of the losses can lock the phases of the modes in a laser having inhomogeneously-broadened gain[26] [43], we have to start from the analysis of Maxwell's equations (eq. 1.43). It is important to note that the periodicity of the modulation has to be close to the round-trip transit time. We consider eq. 1.43a as it is, while in eq. 1.43b we introduce gain and periodic losses through a time-dependent conductivity $\sigma(\vec{r}, t)$ as follows:

$$\vec{\nabla} \wedge \vec{H} = \sigma(\vec{r}, t)\vec{E} + \varepsilon\frac{\partial}{\partial t}\vec{E} \qquad (1.73)$$

Replacing $\vec{H}$ in eq. 1.73 using eq. 1.43a, and recalling as usual eqs. 1.49 and 1.50, we obtain the wave equation

$$\nabla^2\vec{E} - \mu\sigma(\vec{r}, t)\frac{\partial}{\partial t}\vec{E} - \mu\varepsilon\frac{\partial^2}{\partial t^2}\vec{E} = 0 \qquad (1.74)$$

---

[25]This result comes from the property of the Gaussian shape. Combined with the quadratic approximation for the gain medium, multiplying the Gaussian pulse spectrum by the gain function using the quadratic expansion, a new Gaussian pulse with a modified pulse parameter is obtained. In other words, the Gaussian pulse tends to maintain its Gaussian shape after each round trip.

[26]This means that the laser, increasing the pumping, spontaneously operates in multimode regime.

where we have considered $\sigma(\vec{r},t)$ slowly-varying compared to $\vec{E}$. First of all we solve eq. 1.74 for $\sigma = 0$. The simplest solution within a cavity of length L is a set of plane waves, where $\vec{E}(\vec{r},t) = \hat{x}E(z,t)$, with

$$E(z,t) = \sum_i a_i \, \mathrm{e}^{\mathrm{i}2\pi n i f_s z/c} \, \mathrm{e}^{\mathrm{i}2\pi i f_s t} \tag{1.75}$$

where the complex formalism is adopted. Since $c^2 = 1/(\mu\varepsilon)$, each term in eq. 1.75 satisfies eq. 1.74 with $\sigma = 0$, and the same holds for the total field $E(z,t)$ for any arbitrary choice of the mode amplitudes a_i. Considering now $\sigma(\vec{r},t) \neq 0$, the field solution given by eq. 1.75 no longer satisfies eq. 1.74, but we can still use the complete and orthonormal basis function set $\mathrm{e}^{\mathrm{i}2\pi n i f_s z/c}$ to expand the field at any time t at a position $0 < z < rL$. The expression is the same as eq. 1.75 but with $a_i \to a_i(t)$. Here the factor $a_i(t)\,\mathrm{e}^{\mathrm{i}2\pi i f_s t}$ is merely seen as the Fourier series expansion coefficient of the field at time t, i.e.

$$E(z,t) = \sum_i b_i(t)E_i(z) \tag{1.76a}$$

$$E_i(z) = \mathrm{e}^{\mathrm{i}2\pi n i f_s z/c} \tag{1.76b}$$

$$b_i(t) = a_i(t)\,\mathrm{e}^{\mathrm{i}2\pi i f_s t} \tag{1.76c}$$

The basic difference respect to the case $\sigma = 0$ is that now the coefficients $a_i(t)$ are no longer arbitrary and are related to each other, as imposed by eq. 1.74. Replacing eq. 1.76 in eq. 1.74 we obtain

$$\sum_i \left\{ a_i(t) \left[\nabla^2 \vec{E}_i + \mu\varepsilon(2\pi i f_s)^2 \vec{E}_i \right] - [\mu\sigma(\vec{r},t) + 2\,\mathrm{i}\,\mu\varepsilon 2\pi i f_s] \vec{E}_i \frac{\partial}{\partial t} a_i + \right.$$
$$\left. -\,\mathrm{i}\,2\pi i f_s \mu\sigma(\vec{r},t) a_i \vec{E}_i \right\} \mathrm{e}^{\mathrm{i}2\pi i f_s t} = 0$$

$$\tag{1.77}$$

The sum of the first two terms vanishes according to eq. 1.74 with $\sigma = 0$. Moreover we have to consider that $\sigma/\varepsilon \ll i f_s$.[27] At the end we obtain

$$\sum_i \vec{E}_i \frac{\mathrm{d}a_i}{\mathrm{d}t} \mathrm{e}^{\mathrm{i}2\pi i f_s t} = -\sum_i a_i \frac{\sigma(\vec{r},t)}{2\varepsilon} \vec{E}_i \mathrm{e}^{\mathrm{i}2\pi i f_s t} \tag{1.78}$$

---

[27]This is equivalent to state that the frequency spacing among the modes is much greater than the modes linewidth.

In this discussion, $\sigma(\vec{r},t)$ represents both the time-independent average loss as well as the periodic loss modulation, yielding the mode locking. Therefore we express it as

$$\sigma(\vec{r},t) = \sigma_0 + \sigma_m f(\vec{r}) \left(e^{i2\pi f_m t} + e^{-i2\pi f_m t}\right)/2 \qquad (1.79)$$

where f_m is the modulation frequency and σ_m a real constant. Replacing $\sigma(\vec{r},t)$ in eq. 1.78, then dot-multiplying both sides by $\vec{E}_j(\vec{r})$ (namely the same set of modes, but indexed independently) and integrating over the resonator volume, considering the orthonormality of the waves, we obtain

$$e^{i2\pi i\nu_j t}\frac{d}{dt}a_j = -e^{i2\pi i\nu_i t}\frac{\sigma_0}{2\varepsilon}a_i - \sum_i S_{ij}\frac{\sigma_m f(\vec{r})\left(e^{i2\pi f_m t} + e^{-i2\pi f_m t}\right)}{4\varepsilon}a_i e^{i2\pi i\nu_i t}$$

$$(1.80a)$$

$$S_{ij} = \int\limits_{V_{\text{resonator}}} f(\vec{r})\,\vec{E}_i\cdot\vec{E}_j^+\,dV \qquad (1.80b)$$

For $\sigma_m = 0$ (no modulation) we have

$$a_i(t) = a_i(0)\,e^{-\sigma_0 t/(2\varepsilon)} \qquad (1.81)$$

giving that ε/σ_0 is the decay time, that approaches infinity since in lasers the gain compensates for the losses within a bandwidth given by the inverse of the laser transition lifetime. Therefore we can assume $\sigma_0 = 0$ and eq. 1.80a becomes

$$\frac{d}{dt}a_j = -\sum_i \frac{S_{ij}\sigma_m}{4\varepsilon}\,a_i \left(e^{i2\pi f_m t} + e^{-i2\pi f_m t}\right) e^{i2\pi(i-j)f_s t} \qquad (1.82)$$

For sustained interaction the sum of the terms $[(i-j)f_s \pm f_m]$ must be close to zero, i.e. the modulation frequency must be almost equal to the difference of two cavity modes. We introduce therefore the detuning as

$$\Delta = 2\pi(f_s - f_m) \qquad (1.83)$$

Keeping only the two synchronous terms on the right side of eq. 1.82, which correspond to $i = j + 1$ and $i = j - 1$, we obtain

$$\frac{\mathrm{d}}{\mathrm{d}t} a_i = \varkappa a_{i+1} \, \mathrm{e}^{\mathrm{i}t\Delta} + \varkappa a_{i-1} \, \mathrm{e}^{-\mathrm{i}t\Delta} \qquad (1.84\mathrm{a})$$

$$\varkappa = \frac{S_{i,i+1}\sigma_m}{4\varepsilon} \qquad (1.84\mathrm{b})$$

At this point we note that the effect of the modulation is reduced to a simple coupled mode equation. As stated by eq. 1.80b, because of the orthogonality of the modes, $f(\vec{r}) = \text{constant}$ would imply $\varkappa = 0$, meaning that the modulation has to be non-uniform along the laser cavity. To simplify the discussion we introduce the quantity

$$c_i(t) = -\mathrm{i}\, \mathrm{e}^{\mathrm{i}t\Delta} \, \mathrm{e}^{-\mathrm{i}i\pi/2} \, a_i(t) \qquad (1.85\mathrm{a})$$

$$a_i(t) = \mathrm{i}\, c_i(t) \, \mathrm{e}^{-\mathrm{i}it\Delta} \, \mathrm{e}^{+\mathrm{i}i\pi/2} \qquad (1.85\mathrm{b})$$

yielding

$$\mathrm{i}\frac{\mathrm{d}}{\mathrm{d}t} c_i + \mathrm{i}c_i\Delta = -\varkappa c_{i+1} + \varkappa c_{i-1} \qquad (1.86)$$

The steady state solution $(\mathrm{d}c_i/\mathrm{d}t = 0)$ of this equation is

$$c_i = \mathrm{I}_i\left(\frac{\varkappa}{\Delta}\right) \qquad (1.87)$$

where I_i is the hyperbolic Bessel function (or modified Bessel Function)[28] of order i. For the Bessel function, in the limit $\varkappa/\Delta \gg 1$, we have $\mathrm{I}_i(\varkappa/\Delta) \to (2\pi\varkappa/\Delta)^{-1/2}$, yielding as original modes amplitudes

$$a_i(t) = \mathrm{i}\,\frac{\mathrm{e}^{-\mathrm{i}i(t\Delta - \pi/2)}}{\sqrt{2\pi\varkappa/\Delta}} \qquad (1.88)$$

The total laser field (eq. 1.76) is then

$$E(t) = \sum_i \mathrm{i}\,\frac{\mathrm{e}^{\mathrm{i}i\pi/2}}{\sqrt{2\pi\varkappa/\Delta}} \, \mathrm{e}^{-\mathrm{i}2\pi i f_m t} \qquad (1.89)$$

The laser field is no longer made of independent modes, it has to be expressed as a superposition of modes with fixed amplitudes, phases and frequencies, a so-called *supermode*. The spacing between the modes is given by f_m, even though this value has to be close to the natural mode

---

[28]The relation that links the hyperbolic Bessel functions to the standard Bessel functions is $\mathrm{I}_i(x) = \mathrm{i}^{-i} \mathrm{J}_i(\mathrm{i}x)$.

spacing.

The former discussion holds for lasers having inhomogeneously-broadened gain. Ideal lasers having homogeneously-broadened gain do not operate spontaneously in multimode regime. However, in that case the modulation itself generates the side modes starting from the carrier and bringing them above threshold.

1.3.2 Passive mode locking

A number of fast actuators, such as acousto-optic modulators [47] or semiconductor elements, have been used to actively mode-lock different types of lasers. However, the best performances in terms of pulse shortness and peak energy are proper of *passively mode-locked* lasers. In order to have a spontaneous modulation of the losses, non-linear effects within the laser cavity have to take place. For example, the insertion within the laser cavity of a *saturable-absorber* element favors pulse operation than continuous-wave one, since the pulse, due to its highly-concentrated energy, saturates the absorbing element, experimenting lower losses than the continuous-wave radiation would do. In order to have a stable pulsed regime, the laser dynamics has to be regulated by properly temporized phenomena. We define T_{sat} as the saturable absorber recovery time and T_g as the laser transition (gain) recovery time. To generate short and high-energy pulses, the recovery constants have to be $T_{sat} < T_r < T_g$, i.e. the saturable absorber has to recover faster than the cavity round-trip time,[29] while the gain has to recover more slowly. According to the type of laser, examples of used saturable absorbers are dilute solutions of organic dyes [48], or appropriate molecular gases, or semiconductor materials. An interesting approach consist in the use of SESAMs – intracavity semiconductor saturable absorber mirrors [49].

The *optical Kerr effect* constitutes a valid alternative to the saturation as spontaneous phenomenon that ensures a modulation of the losses (see section 1.2.4). It is commonly exploited for example to phase-lock Ti:sapphire lasers. In this case we consider eq. 1.90 where the non-linear refractive index seen by the lasing beam depends on the beam intensity itself:

$$n(I) = n_0 + n_2 I \qquad (1.90)$$

---

[29]See [48] for an example.

Usually $n_2 > 0$. Considering the transverse intensity profile of a Gaussian beam [50]

$$I(r) = \frac{2P}{\pi w^2} e^{-2r^2/w^2} \tag{1.91}$$

where P is the total power in the beam, r is the radial distance from the beam axis (center) and w is the waist. Now, replacing this intensity shape in eq. 1.90, we obtain a differential refractive index profile

$$\Delta n(r) = n_2 \frac{2P}{\pi w^2} e^{-2r^2/w^2} \tag{1.92}$$

At this point we expand $\Delta n(r)$ around $r = 0$ obtaining

$$\Delta n(r) = n_2 \frac{2P}{\pi w^2} \left(1 - \frac{4r^2}{w^2} \right) \tag{1.93}$$

If we think in terms of optical path $\mathcal{L} = nL$ when a beam passes through an optical element, it is completely equivalent to assign the radial variation to the refractive index or to the physical length, namely $\mathcal{L}(r) = n(r)L = nL(r)$. But an optical element with a thickness varying with r as eq. 1.93 is nothing more than a focusing lens. This discussion shows that every Gaussian beam passing through a Kerr medium tends to self-focus. Moreover, we have to consider that due to the longitudinal intensity profile of a pulse, this effect is much more intense for the core of the pulse than for the wings. If we insert an aperture in the laser cavity, we can think to align the cavity in a way that for the continuous-wave operating regime the losses are high, while for the pulsed regime, thanks to the Kerr effect, the losses are lower. In this conditions the mode-locking operation is similar to passive mode-locking in solid-state lasers with a fast saturable absorber. For lasers pumped by other lasers, the finite transverse profile of the pump beam within the active medium constitutes by itself a soft aperture. The dynamic equation describing the interplay among non-linear refractive-index variation, diffraction, and transversely-varying gain (due to the pump beam profile) is expressed in terms of slowly-varying field amplitude $E(x, y, z)$ as [51]

$$\frac{\partial}{\partial z}E + \frac{i}{2k} \left(\frac{\partial^2}{\partial x^2}E + \frac{\partial^2}{\partial y^2}E \right) = g\, e^{-2r^2/w_p^2} E + i\varkappa |E|^2 E \tag{1.94}$$

with $r^2 = x^2 + y^2$. $\varkappa = n_2 k/n_0$ is the Kerr effect coefficient, w_p is the pump-beam size (1/e amplitude), $g = g_0/(1 + S)$ is the saturated gain,

and $S = 2P/(\pi w^2 I_s)$ is the gain-saturation parameter, with P and I_s, the average power and the saturation intensity, respectively. Solving eq. 1.94 shows that through the Kerr effect and the transversely-varying gain, the laser-beam parameters become power dependent, giving rise to the spontaneous modulation that ensures the mode locking.

1.3.3 Frequency-modulation mode locking

Another relevant way of reaching an operating regime where the phases of the modes are related takes advantage of *frequency modulation*. For this case, a discussion similar to the one shown in section 1.3.1 holds. In order to take into account a pure frequency modulation, in eq. 1.79 the constant σ_m has to be taken pure imaginary. As a consequence, the solution of eq. 1.86 is now the standard Bessel function J_i. Again the spectrum of the field is made of a comb of frequencies (eq. 1.89) but now the laser output amplitude is constant, no pulses are emitted.

1.3.4 Frequency-comb parameters control

Eq. 1.65 shows that in mode-locking conditions only two degrees of freedom survive. In order to have a *metrological*[30] OFC it is fundamental to measure and stabilize both f_s and f_o [52]. Observing the emitted radiation with a fast-enough detector,[31] the beat-note signal coming from the beating between the adjacent modes can be detected. This beat note corresponds to f_s. This parameter depends on the cavity length, therefore, comparing f_s with a local oscillator,[32] a phase-locked loop can be implemented to control this parameter acting for example on a piezoelectric actuator mounted on a laser-cavity mirror.

Managing f_o is less trivial. First of all, the simplest and more widespread method for measuring this quantity requires an octave-spanning OFC spectrum.[33] The low-frequency portion of the spectrum has to be frequency-doubled in a non-linear crystal through the SHG process (see section 1.2.2)

---

[30]Here *metrological* means useful for measuring absolute frequencies with a high accuracy (of the order of 10^{-12}).

[31]The detector bandwidth has to be larger than f_s.

[32]The local oscillator can be itself referenced to the primary Cs-clocks standard, providing an absolute reference for the whole system.

[33]This means that within the spectrum both the frequencies ν_N and ν_{2N} have to be present.

and beaten with the high-frequency portion of the spectrum.[34] The beat-note signal oscillates at

$$2\nu_N - \nu_{2N} = 2Nf_s + 2f_o - 2Nf_s - f_o = f_o \qquad (1.95)$$

Even less trivial is controlling f_o. A common practice adopted in solid state lasers consists in trying to drive the laser in a regime where f_o depends on the pump power. In these conditions, fine acting on the power, the parameter can be controlled.

In order to have a real metrological OFC, both f_s and f_o have to be stabilized against a common oscillator referenced to a primary standard, such as a Cs atomic clock.

1.4 Laser emission noise

As a first approximation, the electric field emitted by a laser can be described by a plane wave with a well defined frequency (eq. 1.14). Actually, due to both fundamental and technical reasons, it is physiologic that the field emitted by real lasers undergoes random amplitude and phase *fluctuations*, therefore it is better described as follows:

$$E = \mathrm{Re}\left[E_0(t)\,e^{i[\omega_0 t + \varphi(t)]}\right] \qquad (1.96)$$

where $E_0(t)$ and $\varphi(t)$ are slowly-varying quantities, such that

$$\frac{\mathrm{d}}{\mathrm{d}t}E_0(t)/\langle E_0 \rangle \ll \omega_0 \qquad (1.97\mathrm{a})$$

$$\frac{\mathrm{d}}{\mathrm{d}t}\varphi(t) \ll \omega_0 \qquad (1.97\mathrm{b})$$

These fluctuations are generally defined as *noise*.

In the following sections the noise in laser sources is described. Firstly, in section 1.4.1 the noise spectral density is introduced. Then, in section 1.4.2 the noise due to the spontaneous emission is discussed, with its implications in terms of phase/frequency noise (section 1.4.3). Moreover, in section 1.4.4 the frequency noise quantum limit due to the spontaneous

---

[34]A proper compensation line on one of the two arms has to be implemented in order to compensate for the delay that the pulses on one way can accumulate respect to the other one.

emission is presented. Finally, in section 1.4.5 $1/f$ frequency noise is discussed.

1.4.1 Noise spectral density definition

In eq. 1.96, both the quantities $E_0(t)$ and $\varphi(t)$, henceforth indicated generally as $A(t)$, can be split in a constant component and a time varying part with zero mean value [53], that is the noise, as follows:

$$A(t) = \langle A \rangle + \delta A(t) \tag{1.98}$$

Since we are considering stationary and ergodic noise processes, the mean value denoted with $\langle \ \rangle$ may either refer to the ensemble average or to the average on time

$$\langle A \rangle = \lim_{t' \to \infty} \frac{1}{t'} \int_{t_0}^{t_0+t'} A(t) \, \mathrm{d}t \tag{1.99}$$

The noise may be described in the time domain in terms of its autocorrelation

$$\rho_A(\tau) = \langle \delta A(\tau) \, \delta A(t-\tau) \rangle \tag{1.100}$$

The noise may be also described in the frequency domain in terms of *noise power spectral density* (NPSD)

$$\begin{aligned}
\mathrm{NPSD}_A(f) = \langle |\Delta A(f)|^2 \rangle &= \int_{-\infty}^{+\infty} \rho_A(\tau) \, \mathrm{e}^{-\mathrm{i} \, 2\pi f \tau} \, \mathrm{d}\tau \\
&= \lim_{t' \to \infty} \frac{1}{t'} \left| \int_0^{t'} \delta A(t) \, \mathrm{e}^{-\mathrm{i} \, 2\pi f t} \, \mathrm{d}t \right|^2
\end{aligned} \tag{1.101}$$

$\mathrm{NPSD}_A(f)$ and $\rho_A(\tau)$ form a Fourier transform pair,[35] so that the inverse Fourier transform gives

$$\rho_A(\tau) = \int_{-\infty}^{+\infty} \mathrm{NPSD}_A(f) \, \mathrm{e}^{-\mathrm{i} \, 2\pi f \tau} \, \mathrm{d}f \tag{1.102}$$

$\Delta A(f)$ may be seen as the $\delta A(t)$ Fourier transform. Combining eqs. 1.100–1.102 $\delta A(t)$ mean square can be expressed in terms of $\mathrm{NPSD}_A(f)$ as[36]

$$\langle \delta A^2(t) \rangle = \rho_A(0) = \int_{-\infty}^{+\infty} \mathrm{NPSD}_A(f) \, \mathrm{d}f = \int_{-\infty}^{+\infty} \langle |\Delta A(f)|^2 \rangle \, \mathrm{d}f \tag{1.103}$$

---

[35]This is stated by the Wiener-Khintchine theorem.
[36]This is stated by the Parseval's theorem.

In order to account for the probability that a noise signal exceeds a certain value, the probability density function is introduced. Its normalization is

$$\int_{-\infty}^{+\infty} p(\delta A) \; d(\delta A) = 1 \tag{1.104}$$

and δA nth moment is defined as

$$\langle \delta A^n(t) \rangle = \int_{-\infty}^{+\infty} p(\delta A) \delta A^n \, d(\delta A) \tag{1.105}$$

With $n = 2$ eq. 1.105 is an alternative definition of δA mean-square value. Considering an infinite number of noise processes with different statistics, for the central limit theorem a Gaussian probability density function is obtained:

$$p(\delta A) = \frac{1}{\sqrt{2\pi \langle \delta A^2 \rangle}} \, e^{-\delta A^2/(2\langle \delta A^2 \rangle)} \tag{1.106}$$

1.4.2 Spontaneous emission noise

The *spontaneous emission noise* is the fundamental noise contribution in laser emission. In order to include the spontaneous emission into the classical rate equations, a factor $E_{sp}(t)$ has to be added, yielding

$$\frac{d}{dt} E(t) = \left[i(\omega - \omega_0) + \frac{G-1}{2\tau_{ph}} \right] E(t) + E_{sp}(t) \tag{1.107}$$

where ω_0 is the central optical frequency, τ_{ph} is the photon lifetime in the laser cavity, and the normalized gain is defined as $G = R_{st}\tau_{ph}$, with R_{st} stimulated emission coefficient. Since the spontaneous emission extends over a large frequency range, its noise contribution can be considered as *white*, i.e. constant in frequency, with an autocorrelation function

$$\langle E_{sp}(t) \, E_{sp}^*(t-\tau) \rangle = R\delta(\tau) \tag{1.108}$$

where R is a constant to be determined according to a quantum mechanical discussion, and $\delta(\tau)$ is the Dirac delta function. Spontaneous emission can be treated as thermal light, where photons are emitted in a very large number of uncorrelated processes with different statistics. As a consequence, E_{sp} exhibits a Gaussian probability density function as in eq. 1.106, both for the real and the imaginary part. Eq. 1.107 can be split

in a part for the normalized intensity S, defined as

$$E(t) = \sqrt{S(t)} \; e^{i\varphi(t)} \tag{1.109}$$

and one for the phase. For the intensity we start from $\frac{d}{dt}S = \frac{d}{dt}[E(t)E^*(t)]$ and then we use eq. 1.107, while for the phase we start from $\frac{d}{dt}\varphi = \text{Im}[E^*(t)\frac{d}{dt}E]/S(t)$ and then again eq. 1.107, yielding

$$\frac{d}{dt}S = \frac{S}{\tau_{ph}}(G-1) + 2\,\text{Re}[E_{sp}(t)\,E^*(t)] \tag{1.110a}$$

$$\frac{d}{dt}\varphi = (\omega - \omega_0) + \frac{1}{S}\,\text{Im}[E_{sp}(t)\,E^*(t)] \tag{1.110b}$$

Since the laser acts as an amplifier for the spontaneous emission, $E(t)$ do depend on E_{sp}, yielding

$$\langle E_{sp}(t)\,E^*(t)\rangle = \frac{R}{2} \tag{1.111}$$

and then, eq. 1.110a can be rewritten as

$$\frac{d}{dt}S = \frac{S}{\tau_{ph}}(G-1) + R + F_S(t) \tag{1.112}$$

where $F_S(t)$ is the related Langevin noise source, and $R = K_{tot}R_{sp}$, with K_{tot} and R_{sp} enhancement factor and spontaneous emission coefficient, respectively. Comparing eqs. 1.110a and 1.112 and recalling eq. 1.109, we obtain

$$F_S(t) \approx 2E_x(t)\sqrt{\langle S\rangle} \tag{1.113}$$

In particular

$$E_x(t) \approx \text{Re}\left[e^{-i\varphi(t)}E_{sp}(t)\right] \tag{1.114a}$$

and

$$E_y(t) \approx \text{Im}\left[e^{-i\varphi(t)}E_{sp}(t)\right] \tag{1.114b}$$

represent two independent zero-mean-value Gaussian processes with equal autocorrelation function

$$\langle E_x(t)E_x(t-\tau)\rangle = \langle E_y(t)E_y(t-\tau)\rangle \tag{1.115}$$

and

$$\langle E_{sp}(t)E_{sp}^*(t-\tau)\rangle = 2\langle E_x(t)E_x(t-\tau)\rangle = R\delta(\tau) \qquad (1.116)$$

yielding

$$\langle F_S(t)F_S(t-\tau)\rangle = 2R\langle S\rangle\delta(\tau) \qquad (1.117)$$

For the phase as well a Langevin noise source can be introduced:

$$\frac{\mathrm{d}}{\mathrm{d}t}\varphi = (\omega - \omega_0) + F_\varphi(t) \qquad (1.118)$$

where $F_\varphi(t)$ is given by

$$F_\varphi(t) \approx \frac{E_y(t)}{\sqrt{\langle S\rangle}} \qquad (1.119)$$

with autocorrelation function

$$\langle F_\varphi(t)F_\varphi(t-\tau)\rangle = \frac{R\delta(\tau)}{2\langle S\rangle} \qquad (1.120)$$

F_S and F_φ as well represent two independent Gaussian noise processes with zero mean value.

1.4.3 Phase/frequency noise and related emission spectrum

Phase (or frequency) noise is particularly important for laser sources since it determines the *finite linewidth* of the emitted radiation. The following discussion will show how to relate phase and frequency noise to the power spectrum.[37] We consider again eq. 1.109 for the slowly-varying complex field amplitude. Phase noise is related to the fluctuations of $\varphi(t)$. For the discussion it is worth introducing the instantaneous frequency $\dot{\varphi} = \frac{\mathrm{d}}{\mathrm{d}t}\varphi$, which represents the deviation from the central frequency ω_0. We define the phase difference and the instantaneous frequency difference as

$$\delta\varphi = \varphi - \langle\dot{\varphi}\rangle t \qquad (1.121a)$$
$$\delta\dot{\varphi} = \dot{\varphi} - \langle\dot{\varphi}\rangle \qquad (1.121b)$$

so that the latter has a zero mean value and the laser radiation mean frequency is $\langle\omega\rangle = \omega_0 + \langle\dot{\varphi}\rangle$. Clearly, even for $\delta\dot{\varphi}(t)$ eq. 1.101, with

---

[37]Here with power spectrum we mean the distribution of the laser power in frequency domain around the carrier frequency $\omega_0 = 2\pi\nu_0$.

$\mathrm{NPSD}_A(f) = \mathrm{NPSD}_{\dot{\varphi}}(f) = \mathrm{FNPSD}(f)$, holds.

In interferometric setups the phase difference for a delay τ can be observed[38]

$$\langle \Delta\varphi^2 \rangle = \langle [\delta\varphi(t) - \delta\varphi(t-\tau)]^2 \rangle = \tau^2 \int_{-\infty}^{+\infty} \mathrm{FNPSD}(f) \frac{\sin^2(2\pi f\tau/2)}{(2\pi f\tau/2)^2} \, \mathrm{d}f \tag{1.122}$$

Knowing this phase difference it is possible to evaluate the autocorrelation function of the field amplitude. Neglecting the intensity noise, the field and its autocorrelation are expressed as

$$E(t) = \sqrt{\langle S \rangle}\, \mathrm{e}^{\mathrm{i}[\delta\varphi(t) + \langle\dot{\varphi}\rangle t]} \tag{1.123}$$

$$\langle E(t)E^*(t-\tau) \rangle = \langle S \rangle\, \mathrm{e}^{\mathrm{i}\langle\dot{\varphi}\rangle\tau} \langle \mathrm{e}^{\mathrm{i}\Delta\varphi} \rangle \tag{1.124}$$

Recalling the series expansion of the exponential function and using the Gaussian moment theorem [54], it can be proven that

$$\langle \mathrm{e}^{\mathrm{i}\Delta\varphi} \rangle = \mathrm{e}^{\langle\Delta\varphi^2\rangle/2} \tag{1.125}$$

At this point the *power spectrum* is obtained by evaluating the Fourier transform of the autocorrelation function:

$$W_E(\Delta\nu) = \int_{-\infty}^{+\infty} \langle E(t)E^*(t-\tau) \rangle\, \mathrm{e}^{\mathrm{i}2\pi\tau\Delta\nu} \, \mathrm{d}\tau \tag{1.126}$$

where $\Delta\nu = \nu - \langle\nu\rangle$. Alternatively, introducing the one-side Fourier transform and the one-side $\mathrm{FNPSD}(f)$ we obtain Elliott's equation

$$W_E(\Delta\nu) = \langle S \rangle \int_0^\infty \mathrm{d}\tau \, \cos(2\pi\tau\Delta\nu) \, \mathrm{e}^{-Z(\tau)} \tag{1.127a}$$

with

$$Z(\tau) = 2 \int_{1/T}^\infty \mathrm{d}f \, \mathrm{FNPSD}(f) \left[\frac{\sin(\pi f\tau)}{f} \right]^2 \tag{1.127b}$$

where T is the time scale on which the $\mathrm{FNPSD}(f)$ has been acquired. This is a general result: having the frequency noise spectral density $\mathrm{FNPSD}(f)$ acquired on a certain time scale T, the power spectrum on that time scale can be computed.

---

[38]See [54] for a comparison.

1.4.4 Quantum noise limit

The case of white frequency noise, i.e. a flat FNPSD, is particularly important, since the frequency noise due to *spontaneous emission* is of this type. In this case eq. 1.122 gives

$$\langle \Delta \varphi^2 \rangle = |\tau| \, \text{FNPSD} = 2 \frac{|\tau|}{t_c} \tag{1.128}$$

where t_c is the coherence time. Since the variance of the phase difference increases with time, and the coherence decreases, t_c is an estimation of the time delay in which the radiation can interfere with itself. Applying eqs. 1.126–1.128 for this case we obtain

$$W_{E \text{ white}}(\Delta \nu) = \frac{\langle S \rangle}{\pi^2 \, \text{FNPSD}} \frac{1}{1 + \left(\frac{2 \, \Delta \nu}{\pi \, \text{FNPSD}} \right)^2} \tag{1.129}$$

The shape of the power spectrum is Lorentzian, with a FWHM of $2 \, \Delta \nu = \pi \, \text{FNPSD}$, value that is independent of the acquisition time scale T. This width is named *intrinsic linewidth*.

In order to obtain the white FNPSD given by the spontaneous emission, we recall eq. 1.101 for the phase (eq. 1.118) and considering only the Langevin force term for the autocorrelation (eq. 1.120) we obtain

$$\text{FNPSD}_{\text{S-T}} = \frac{R}{2\langle S \rangle} \int_{-\infty}^{+\infty} \delta(\tau) \, e^{-i \, 2\pi f \tau} \, d\tau = \frac{R}{2\langle S \rangle} \approx \frac{K_{tot} n_{sp}}{2\tau_{ph} \langle S \rangle} \tag{1.130}$$

where $n_{sp} = R_{sp}/R_{st}$ is the ratio between the spontaneous emission and the stimulated emission coefficients. This is the lowest noise level for a laser, set by the quantum nature of the emission. It is essentially given by the ratio of the spontaneous photons to the stimulated ones, and for these reason it shows a $1/P$ dependency, where P is the optical power emitted by the laser. This result was firstly obtained by Schawlow and Townes in 1958 [55]. For semiconductor lasers it was clear since the beginning that this expression could not reproduce the data. The prediction was always underestimated. In 1982 Henry realized that for semiconductor lasers this discussion is incomplete, since it neglects the intensity noise contribution to the frequency noise.[39] Therefore he proposed to add a

---

[39]This contribution is due to the intensity noise which modulates the population and therefore the gain. Eq. 1.10 tell that to a modulation of the gain corresponds a modulation of the refractive index and, as a consequence, a modulation of the frequency.

factor α_E and a function $H(f)$ to account for this phenomenon [56], such that

$$\text{FNPSD}_{\text{S-T-H}} = \frac{K_{tot}n_{sp}}{2\tau_{ph}\langle S \rangle}(\alpha_E^2|H(f)|^2 + 1) \tag{1.131a}$$

with

$$H(f) = \frac{1}{(\text{i } f/f_{rx})^2 + \text{i } f/f_d + 1} \tag{1.131b}$$

where f_{rx} is the relaxation resonance frequency and f_d the damping frequency. The α_E parameter is for standard bipolar semiconductor lasers of the order of $3\ldots7$.

1.4.5 $1/f$ frequency noise

At low frequencies the FNPSD of common free-running lasers exhibits a $1/f$ trend. This contribution is named *flicker noise* and it is independent on the emitted power. In this case we can write

$$\text{FNPSD}(f) = \frac{f_{FL}^2}{f} \tag{1.132}$$

where f_{FL} is the characteristic frequency determining the magnitude of this type of noise. Here it is important to work with the one-side FNPSD. Moreover we underline that to measure the FNPSD for $f \to 0$ a time $T \to \infty$ would be required. Since in practical cases T is always finite, the integral in eq. 1.122 (as in eq. 1.127b) can be evaluated from $1/T$ to $+\infty$ avoiding the divergence. Considering $\tau/T \ll 1$ and replacing $\tau \to t_c$ in the logarithm in the result, we finally obtain

$$\langle \Delta\varphi^2 \rangle \approx \tau^2 4\pi f_{FL}^2 \ln\left(\frac{5T}{t_c}\right) \tag{1.133}$$

Since the dependence on τ is quadratic, a Gaussian autocorrelation function for the field is obtained (eqs. 1.124 and 1.125). Finally, using eq. 1.126, a Gaussian power spectrum is obtained:

$$W_{E\ 1/f}(\Delta\nu) = \langle S \rangle \frac{\sqrt{2}}{4f_{FL}l} \text{ e}^{-\left[\Delta\nu/\left(f_{FL}l\sqrt{2\ln2/\pi}\right)\right]^2} \tag{1.134}$$

with $l = \sqrt{\ln(5T/t_c)}$. In this case the width of the obtained spectrum does depend on the acquisition time scale T. As shown in fig. 1.6, if a FNPSD is made of a $1/f$ part (at low frequencies) and of a white noise one (at high frequencies), $\langle \Delta\varphi^2 \rangle$ is given by the sum of the two
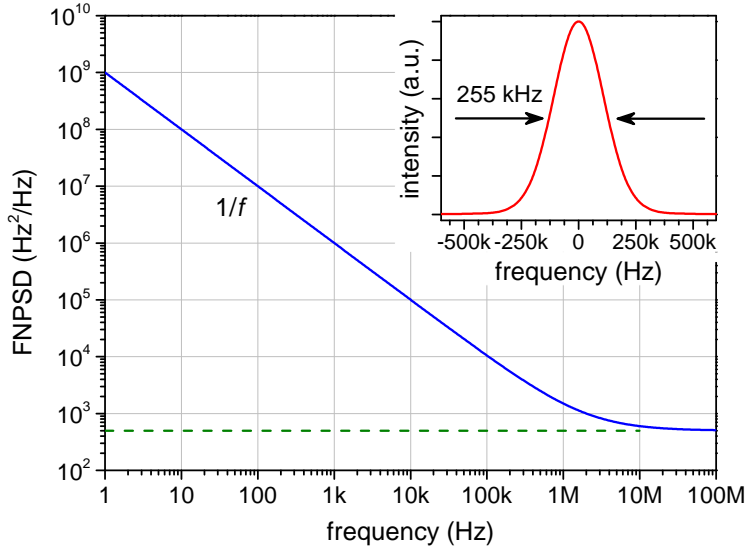
Figure 1.6: In this graph a typical laser FNPSD is depicted. The FNPSD is made of a $1/f$ part and a white noise one, the latter due to the spontaneous emission (intrinsic noise).

Inset: Laser power spectrum (centered around the carrier optical frequency ν_0) related to the shown FNPSD. It has been computed solving numerically eq. 1.127. The curve is a Voigt function, given by the convolution of the white-noise Lorentzian contribution and the $1/f$ Gaussian contribution.

contributions, and the resulting power spectrum is the convolution of a Lorentzian and a Gaussian function (Voigt profile), each of them with its own width.

1.5 Quantum cascade lasers

Quantum cascade lasers (QCLs) are current-driven semiconductor lasers based on intersubband transitions in quantum wells. To date they are the best-performing lasers in the mid-infrared and terahertz wavelength region, in terms of reliability and power combined with tunability. For this reason they are fundamental tools for molecular spectroscopy.

In the following sections QCLs realization and operation are briefly described. Firstly, in section 1.5.1 an introduction on the basic operating principles is given. Then, in section 1.5.2 the fabrication process is described. The nowadays-adopted solutions for having broad-gain devices, which ensure wide single-mode tunability or wide multimode spectra, are

presented in section 1.5.3. Finally, in section 1.5.4 the QCLs capability of generating frequency combs is discussed, together with their peculiar mode-locking mechanism.

1.5.1 Fundamentals

The first proposal of such a device was made by Kazarinov and Suris in 1971 [57]. The proposed semiconductor active region is a superlattice made of uniform wells. The idea is very simple as well as intriguing, but unfortunately the structure proved to be electrically unstable. The first working QCL, realized at Bell Labs by Faist and co-workers in 1994 [13], is based on a complex *superlattice* made of different cells, each of them made of a series of *quantum wells*. In particular, each cell (or period) is divided into two regions, a gain region and a relaxation-injection region (see fig. 1.7).

- In the *gain region* a population inversion is maintained by the current flux due to the externally-applied electric field. Here three levels, which are sublevels of the electronic conduction band, are present. The electrons are injected in level 3 (the highest in energy) and the population inversion is maintained between level 3 and level 2.

- The adjacent *relaxation-injection* region must essentially drive the electrons from level 1 of the preceding gain region to level 3 of the following one, matching the energies. The transition occurs through resonant tunneling. A portion of this region is doped with electron donors, in order to provide the carriers.

The structure is organized in an *alternate cascade* of relaxation-injection and gain regions in a number that spans from 10 to 100. The externally-applied electric field provides the needed potential energy to the electrons. The advantages of this cascade structure are the decreasing of the population density required for each individual gain region, with the consequent reduction of the threshold current density, and the possibility of recycling the same electrons for many transitions. In principle, each electron can generate as many photons as the gain regions are.
In order to understand the essential behavior of a QCL, we consider the
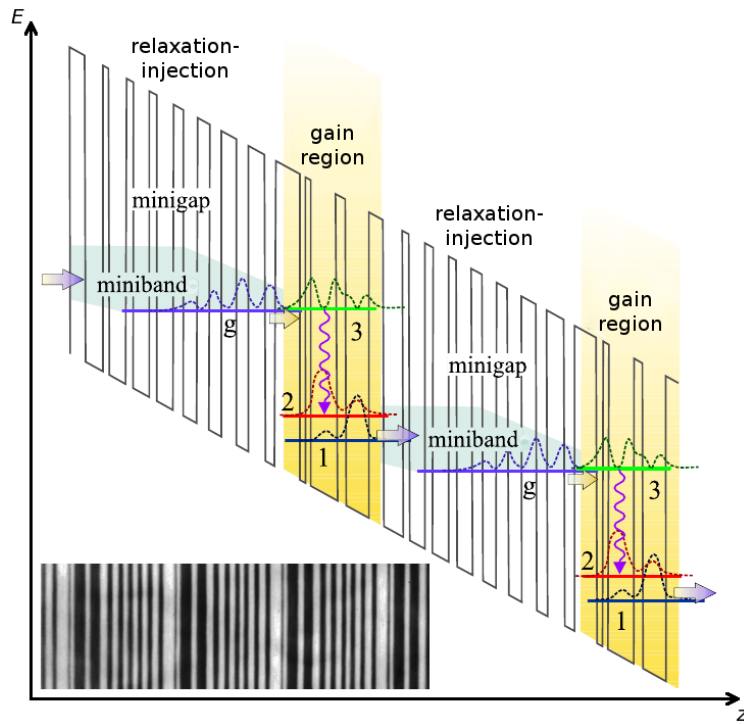
Figure 1.7: Schematic of the band structure of a QCL. The scheme shows a three-quantum-well vertical-transition design. Two periods are shown. Together with the superlattice, the square moduli of the electronic wavefunctions are depicted. The overall slope is given by the externally-applied electric field. The thick arrows denote the flow of the electrons, while the thin wavy arrows denotes the laser transition. **g** denotes the ground-state miniband in the relaxation-injection region.

Moreover, a TEM micrograph of a clived cross-section of an active region of the same type is shown. Light regions are AlInAs barriers, while dark regions are GaInAs wells.

rate equations for the three-levels system [58]:

$$\frac{\mathrm{d}}{\mathrm{d}t}n_3 = \frac{J}{e} - \frac{n_3}{\tau_3} - Sg_c(n_3 - n_2) \tag{1.135a}$$

$$\frac{\mathrm{d}}{\mathrm{d}t}n_2 = \frac{n_3}{\tau_{32}} + Sg_c(n_3 - n_2) - \frac{n_3 - n_{2\,\text{the}}}{\tau_2} \tag{1.135b}$$

$$\frac{\mathrm{d}}{\mathrm{d}t}S = \frac{c}{n}\left\{[g_c(n_3 - n_2) - \alpha_{\text{tot}}]S + \beta\frac{n_3}{\tau_{sp}}\right\} \tag{1.135c}$$

where n_3 and n_2 are the upper and lower sheet densities per period (in cm^{-2}), S is the photon flux per unit active region width (in cm^{-1}s^{-1}), τ_3 and τ_2 are the total lifetimes of state 3 and 2 respectively, τ_{32} is the nonradiative relaxation time from level 3 to level 2, τ_{sp} is the spontaneous emission lifetime, $n_{2\,\text{the}}$ is the thermal population of level 2, β is the fraction of spontaneous photons emitted within the lasing mode, g_c is the gain cross section, e is the electron charge, n is the effective refractive index, J is the current density, and α_{tot} are the total losses, due to the mirrors and the waveguide. Neglecting the amplified spontaneous emission, the behavior below threshold can be obtained by eq. 1.135 by setting the time derivatives and S to zero. From eq. 1.135a we obtain $n_3 = J\tau_3/e$, and using this result in eq. 1.135b we obtain for the population inversion

$$\Delta n = n_3 - n_2 = \frac{J\tau_{ef}}{e} - n_{2\,\text{the}} \tag{1.136}$$

with $\tau_{ef} = \tau_3(1 - \tau_2/\tau_{32})$. Note that the population inversion takes place only if $\tau_2 < \tau_{32}$. The threshold current density is reached when the modal gain $g_c\Delta n$ compensates for the losses α_{tot}:

$$J_{\text{thr}} = e\,\frac{\alpha_{\text{tot}}/g_c + n_{2\,\text{the}}}{\tau_{ef}} \tag{1.137}$$

Above threshold the gain is clamped and S increases linearly with J. The slope efficiency is obtained again from eq. 1.135 by setting the derivatives to zero and differentiating over J:

$$\frac{\mathrm{d}}{\mathrm{d}I}P = h\nu\alpha_{m1}\frac{\mathrm{d}}{\mathrm{d}J}P = \frac{h\nu}{e}\frac{\alpha_{m1}}{\alpha_{\text{tot}}}\frac{\tau_{ef}}{\tau_{ef} + \tau_2} \tag{1.138}$$

where α_{m1} are the front mirror losses, P the optical power emitted by the laser and I is here the current flowing thorough the active medium.

1.5.2 Growth, processing and mounting

The first step in QCLs fabrication is the growth of the active medium, i.e. the deposition of the layers that constitute the superlattice. The used technique is *molecular beam epitaxy* (MBE), that enables the deposition of thin layers of material in a fully-controlled way. The MBE machine is essentially a thermal evaporator with a very low base pressure (10^{-11} mbar) and clean environment. While growing QCLs, 3–10-μm-thick semiconductor layers have to be grown, with a layer accuracy of about 1 Å for individual wells and barriers. Typical structures are made of GaInAs/AlInAs layers with varying doping concentration (see fig. 1.7 for an example). The most important tool to check the quality of a growth is high-resolution X-ray diffraction. It provides highly-accurate measurements of thicknesses and lattice parameters.

Once grown the active medium material (wafer), it has to be cut and placed within the waveguide. QCLs are monolithic lasers, the facets of the semiconductor constitute the mirrors of the cavity. A proper design of the waveguide is essential in order to give gain only to the fundamental Gaussian transverse mode, i.e. in order to obtain single-transverse-mode emission devices. In QCLs the population inversion is obtained at the cost of a thermal dissipation of 20–100 kW/cm^2. The heat extraction is a crucial aspect to be taken into account, since the threshold current (eq. 1.137) increases with the temperature of the active region. The type of process that is nowadays usually adopted is called *buried-heterostructure*, where a lateral regrowth of material is made [59]. This is crucial for enhancing heat extraction, allowing QCLs to operate in continuous wave at room temperature. Once the active region sequence of layers is grown by MBE on a substrate, a cladding is grown by metal organic vapor phase epitaxy. Then another layer is deposited by plasma enhanced chemical vapor deposition. Afterwards, using ultraviolet photolitography, the waveguide pattern is transfered on the sample. Then a series of chemical reactions (etching) and regrowth processes give to the waveguide the right shape and electrical conduction/isolation characteristics. Finally, ohmic contacts are deposited on the top and on the bottom. Once the waveguide has been obtained, it has to be cleaved. The length of the cavity spans usually between 1 and 6 mm. As a standard practice, QCLs are mounted epi-side up (junction up) using indium solder on copper submounts, but the best performances in terms of heat extraction are obtained with epi-side down

mounting on diamond submounts. The devices obtained with such a standard process are called *Fabry-Pérot* devices and usually emit multi-longitudinal-mode radiation. In order to obtain a single-mode emission at a specific wavelength, a *distributed feedback* (DFB) can be included in the active region [60], by etching a grating directly onto the waveguide.

1.5.3 Broad-gain devices

As already stated, one of the selling points of QCLs is the wavelength tunability for single-mode devices, or the wide spectral coverage for multimode devices. This features are obtained by using two systems that contribute to broaden the gain curve.

- The first one concerns the design of the active region. Instead of the classic three-levels scheme, the *bound-to-continuum* scheme is adopted [61]. Essentially, levels 2 and 1 are replaced by minibands forming a continuum. There is no more a net separation between the active and the relaxation-injection regions. The whole period is made of a chirped superlattice.

- The other one consists in cascading periods with different gain curve centers [62]. Unlike bipolar interband transitions, intersubband transitions are transparent on both sides (both for higher and lower energies with respect to the peak). For this reason it is possible to grow a cascade of periods made of two or three subgroups, each of them with a gain centered at a different wavelength, resulting in a total wider gain curve.[40]

Combining these two solutions, gain curves as wide as 500 cm^{-1} can be obtained. This value corresponds to 40% of the wavelength at 9 μm.

1.5.4 Quantum-cascade-laser frequency combs

A broad gain, together with a low group velocity dispersion, is an essential feature in order to enable *frequency combs generation* for QCLs (QCL-combs). This unexpected capability has been discovered only recently [34]. The four-wave mixing process (FWM – see section 1.2.4) that takes place in the gain medium [63] is responsible for the mode

---

[40]In this configuration attention must be paid in order to avoid cross reabsorption of photons by couples of levels.

locking in an *auto-injection-locking* fashion. In a simplified framework, we can say that through the non-linear process three laser modes generate radiation nearby a fourth mode.[41] This radiation tends to injection-lock the nearest mode.[42] This phenomenon tends to take place in cascade in every portion of the laser emission spectrum, ensuring the locking of all the modes. For mid-infrared operating devices the upper-state lifetime, inherent to the intersubband transition of the active region, is very short (≈ 0.3 ps) compared to the cavity round-trip time (≈ 140 ps for 6-mm-long devices). This is responsible for the broadband nature of the FWM that ensures the mode locking, but also for a tendency to operate with a nearly constant output power, damping any energy spike propagating at the round-trip frequency within the cavity. As a consequence, the phase relation between the modes is similar to that of frequency-modulated lasers (see section 1.3.3), as theoretically predicted [64, 65], and no pulses are emitted.

---

[41]This closeness is due to the law of energy conservation (see section 1.2.4), which preserves the spacing among the modes.

[42]The injection locking of two oscillators happens if their distance in frequency falls within the bandwidth of the process, which is given essentially by $\Delta f_{\text{inj-lo}} = \eta f_s \sqrt{(P_m/P_s)}/(2\pi^2)$, where η is a coupling factor, and $P_{m,s}$ is the power of the master source (the radiation generated through FWM in our case) and of the slave oscillator (the natural laser mode), respectively [50]. Within the bandwidth, the stationary phase difference is given by $\Delta\varphi = \varphi - \varphi_m = \sin^{-1}[(f_s - f_m)/\Delta f_{\text{inj-lo}}]$, where φ_m and $f_{m,s}$ are phase and frequency of the master and the slave oscillator, respectively.

CHAPTER 2

The experiments

2.1 Single-frequency quantum cascade lasers stabilization and spectroscopy

As stated in sections 1.1.5 and 1.1.6, in order to perform high-sensitivity and resolution sub-Doppler spectroscopy, it is fundamental to have intense and narrow (low-frequency-noise) mid-infrared laser sources. Moreover, if also a high accuracy is required, an absolute reference for frequencies is needed. QCLs (see section 1.5) are ideal candidates for this role, since their intrinsic linewidth[1] is comparable to the natural linewidth of molecular transitions (tens–hundreds of Hz), and the emitted radiation intensity spans from the milliwatt up to the watt level. Moreover, their tunability is another desirable feature (see section 1.5.3). Unfortunately, on a time scale spanning from 1 s to 10 ms, QCLs linewidth is way wider in free-running operation (about 1 MHz) due to the $1/f$ noise contribution (see section 1.4.5). Two main approaches can be used in order to overcome this limitation and to provide the desired absolute frequency reference: (1) The QCL emission can be stabilized and narrowed against a molecular absorption line, (2) or it can be referenced to an OFC (see section 1.3) through a phase-locking chain. Such schemes are described in the following sections (sections 2.1.1 and 2.1.2, respectively). Moreover, in section 2.1.3 a demonstration of the phase-locking setup performances for high-resolution CO_2 spectroscopy is described.

2.1.1 Polarization locking

With the following experiment, a method to obtain a narrow-emission and absolutely-referenced QCL has been proven [67]. It exploits the avail-

---

[1]See section 1.4.4 for an overview and ref. [66] for the first measurement.

ability of a natural ruler of frequency references given by the many strong molecular absorption lines, whose center frequency can be absolutely measured with a sub-kHz precision [39]. Basing on this, it is possible to have a simple system for high-sensitivity/precision spectroscopy for a specific molecular species, without using an OFC. A *polarization-spectroscopy* (PS) scheme[2] produces, without any external modulation, the narrow dispersive sub-Doppler signal used to close the feedback loop on the QCL driving current for frequency stabilization. It will be shown that the linewidth of a continuous-wave room temperature QCL can be narrowed below 1 kHz (FWHM) by locking the laser to a CO_2 line.

The laser is a room temperature DFB QCL emitting at 4.3 μm, provided by Hamamatsu Photonics. It is operated at a temperature of 283 K and a current of 710 mA, delivering an output power of about 10 mW. A
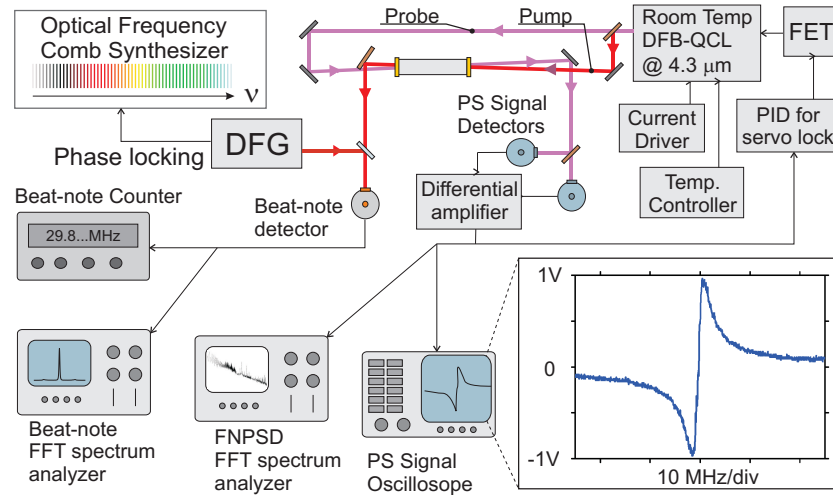
Figure 2.1: Polarization-locking setup. The probe beam gives the signal used for the frequency locking. The pump beam is also used for the beat-note detection and the frequency counting. PS: polarization spectroscopy, DFG: comb-referenced single-frequency difference-frequency generation, FET: field-effect transistor, FFT: fast Fourier transform.

schematic of the experiment is shown in fig. 2.1. The QCL is mounted on a specific compact thermoelectrically-cooled mounting. A low-noise home-made current driver is used. It ensures a current noise power spectral density always below 1 nA/$\sqrt{\text{Hz}}$, while keeping a fast current modulation capability, thanks to a control circuitry placed in parallel to the QCL based on a field-effect transistor (FET).

---

[2]See section 1.1.7 for an overview and ref. [41] for an example.

The chosen molecular transition is the P(29)e of the $(01^11 - 01^10)$ ro-vibrational band of CO_2 at 2311.5152 cm^{-1} (see section 1.1.3). The inset of fig. 2.1 shows a typical scan of the PS signal at a pressure of 8.9 Pa, when the laser frequency is tuned across the molecular resonance. By carefully balancing the differential detection, a zero-offset signal is obtained. It ensures a linear conversion of the laser frequency fluctuations into amplitude variations in the region centered around the resonance frequency.

For the QCL *frequency stabilization*, the PS signal is processed by a home-made PID controller, and fed back to the FET gate for current control. From a preliminary analysis of the free-running frequency noise power spectral density (FNPSD) of a similar QCL [68], it is expected that a locking bandwidth of about 100 kHz is required for reaching a kHz-level linewidth. In order to ensure this condition, both the differential amplifier and the PID have been designed to have bandwidths larger than 1 MHz. However, there are two more fundamental aspects that can limit the loop bandwidth. The first is the roll-off of the QCL tuning rate with the modulation frequency [69]: the tuning rate is never flat, even at low frequencies, and shows a -3 dB cut-off at about 100 kHz. The second is the width of the linear region of the PS signal, that introduces a frequency roll-off starting from 300 kHz. Following the above considerations, the bandwidth of the frequency-locking loop is expected to be in the range of a few hundred kHz.

In order to characterize the frequency locking, two different measurements are carried out in parallel. The first one is the spectral analysis of the in-loop PS signal, the second one is the analysis of the beat note between the QCL and a narrow OFC-referenced DFG source[3] providing a stable (10-Hz linewidth within 100 μs) and absolute reference. Each measurement has been also performed with the QCL in free-running regime.

In fig. 2.2 the FNPSD measurement results are shown. Firstly, it is noteworthy to highlight the improvements in the free-running regime brought by the evolution of the current driver: using the new-generation low-noise driver, the FNPSD exhibits a clean $1/f$ trend, confirming that virtually no external noise is added. By closing the frequency-locked

---

[3]See sections 1.2.2 and 1.3 for an overview and ref. [70] for an experimental implementation.
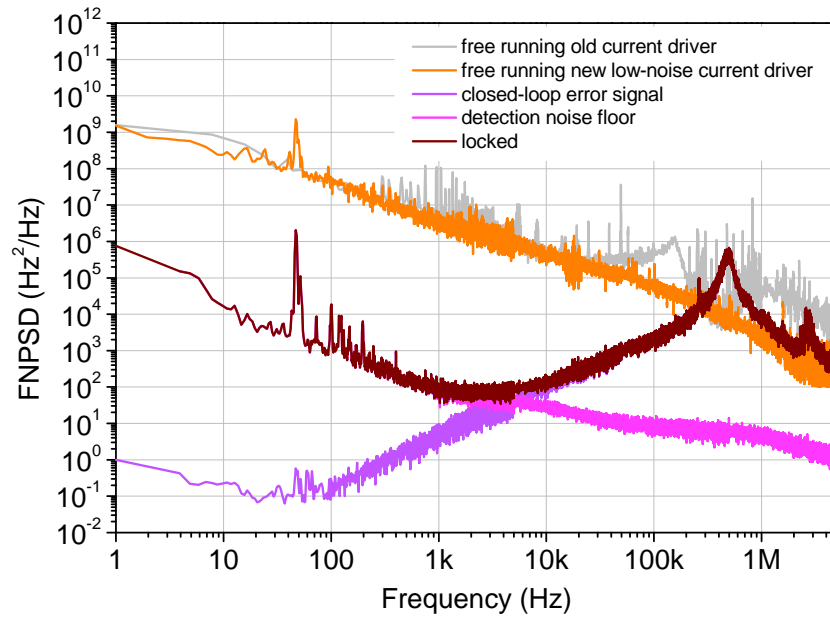
Figure 2.2: Comparison between the free-running QCL FNPSDs and the locked one. The locked QCL FNPSD is obtained by summing the spectrum of the closed-loop error signal to the PS detection noise floor, measured with empty gas cell.

loop, the FNPSD is reduced in the spectral range below 250 kHz, which is then assumed to be the loop bandwidth, as expected. At about 450 kHz, the onset of a self-oscillation peak is evident. It can be well explained by the dephasing introduced by the approaching roll-offs mentioned above and it is, at present, the factor limiting the loop performances. The FNPSD of the locked QCL is obtained by adding to the closed-loop error signal the detection noise floor. The latter is dominated, in the low-frequency range, by the residual intensity noise of the QCL, and limits the frequency-noise reduction.

The effect of the locking on the QCL emission lineshape can be more intuitively described by the spectrum of the beat note between the QCL radiation and the DFG one. An acquisition is shown in fig. 2.3. The 450 kHz servo bumps confirm the oscillation peak appearing in the FNPSD. By comparing the areas of the locked and free-running beat notes we obtain that 77% of the QCL radiation power is forced into the narrow peak centered on the molecular line. Switching from the free-running to the locked regime the linewidth (FWHM) is reduced from about 500 kHz down to 760 Hz on a 1-ms time scale (inset). The inset
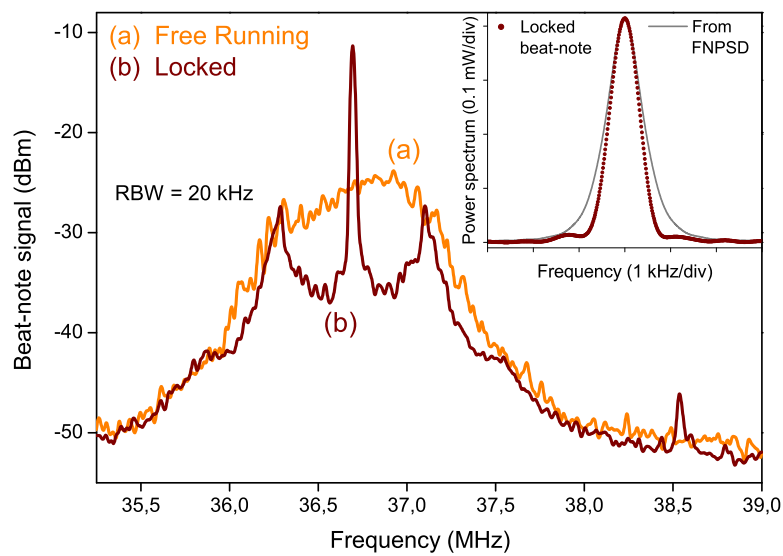
Figure 2.3: FFT spectra of a 10-ms-long evolution of the beat note between the QCL, in free-running (trace a) and locked (trace b) conditions, and the narrow DFG source. **Inset**: zoomed view (linear scale) of the central peak observed over 1 ms with a resolution bandwidth of 721 Hz (dotted curve) and QCL power spectral profile retrieved from the locked FNPSD using eq. 1.127 (straight line).

also shows the comparison between the beat note and the locked QCL power spectral profile retrieved from its FNPSD using eq. 1.127 over a 1 ms time scale. For the latter, a 900 Hz FWHM is obtained, in good agreement with the beat-note linewidth.

The beat-note frequency is also measured by a 1-s-gated frequency counter over about 2 hours. The obtained Allan deviation [7] is 3 kHz at 1 s and decreases down to 0.9 kHz up to 320 s. Then, for longer times, it increases again, due to slow variations of the locking signal offset. This prevents our oscillator from achieving the stability performances of the best mid-infrared standards [71].

The absolute frequency of the CO_2 line is measured by averaging a set of frequency counts performed counting in several days the beat note, and knowing the DFG frequency thanks to the reference. The obtained value is (69297480.708 ± 0.025) MHz, with an uncertainty which takes into account both the repeatability of the offset zeroing and the OFC accuracy. This result is in agreement with the value given by HITRAN database [6] for this transition (see table 2.1), but with at least 2 orders of magnitude increased accuracy.

2.1.2 Single-frequency phase locking

Direct phase locking of QCLs to OFCs is a valid alternative respect to frequency locking to a molecular absorption line (section 2.1.1), allowing to enhance the frequency stability while preserving the full tunability of the laser source, at the cost of a more complex and bulky setup. Having a standard near-infrared OFC and a mid-infrared QCL, two approaches are possible:

- The QCL MIR radiation can be up-converted through sum-frequency generation (SFG - see section 1.2.2) to be beaten with the OFC near-infrared radiation [72]. In this case, the final QCL linewidth is limited by the excess phase noise of the OFC tooth given by its reference oscillator.

- Alternatively, the QCL can be directly phase-locked to a DFG mid-infrared radiation, obtained starting from two OFC-referenced near-infrared sources. This method provides simultaneously an absolute frequency reference and a residual phase noise independent of the OFC noise.

The latter scheme is here presented [73]. A final QCL narrowing below the OFC tooth linewidth is obtained: indeed, a linewidth below 1 kHz on a 1 ms time scale is obtained from the analysis of the FNPSD. The QCL frequency stability and the absolute traceability have been characterized, resulting both limited by the Rb-GPS-disciplined[4] 10-MHz quartz oscillator reference of the OFC. Precision and high resolution spectroscopy performances of this QCL source are tested by measuring the frequency of the saturation Lamb dip of few CO_2 transitions with an uncertainty of 2×10^{-11}.

The laser is the same distributed-feedback QCL emitting at 4.3 μm used for the experiment described in section 2.1.1. It is operated at a temperature of 283 K and a current of 710 mA. The radiation which the QCL has been locked to is produced by non-linear DFG process in a periodically-poled $LiNbO_3$ crystal (see section 1.2.2, 1.2.3 and ref. [15]) by mixing an Yb-fiber-amplified Nd:YAG laser at 1064 nm and an external-cavity diode laser (ECDL) emitting at 854 nm. The peculiar locking scheme, employing a *direct digital synthesis* (DDS) technique [70, 74, 75], makes the ECDL be effectively phase-locked to the Nd:YAG laser, while the OFC just acts as a transfer oscillator adding negligible phase noise to the DFG radiation (see appendix A.7). As a consequence, the mid-infrared radiation is referenced to the Cs frequency standard through the OFC, but its linewidth is independent of the OFC one.

A schematic of the experimental setup is shown in fig. 2.4. A small portion of the QCL beam, taken with a beam-splitter, is used for the phase-locking. It is overlapped to the DFG beam through a second beam splitter and sent to a 200-MHz-bandwidth HgCdTe detector. A 100-MHz beat note is detected by using few μW of both QCL and DFG sources. The beat note is processed by a home-made phase-detection electronics, which compares it with a 100-MHz local oscillator (LO) and provides the error signal for closing the phase-locked loop (PLL). A home-made PID electronics processes the error signal and sends it to the gate of a field-effect transistor (FET) to fast control the QCL driving current. In fig. 2.5 the beat note acquired using a FFT spectrum analyzer is shown. The width of the carrier frequency is limited by the instrumental resolution bandwidth, as expected from a beat note between

---

[4]The Rb clock is compensated for long-term drifts through the reference to the GPS (global positioning system).
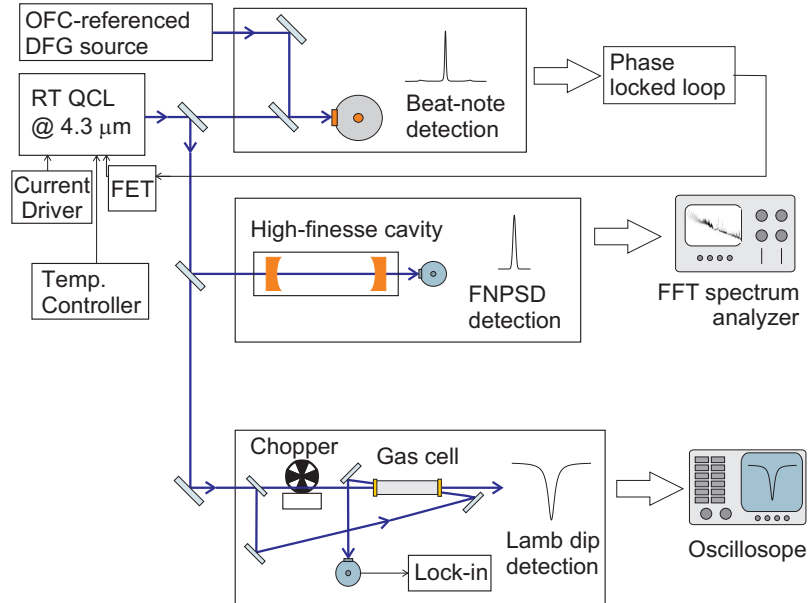
Figure 2.4: Schematic of the experimental setup. There are three main parts: the beat-note detection between QCL and DFG for the phase-locking, the high-finesse cavity for FNPSD analysis and the saturation spectroscopy signal detection for the absolute frequency measurement of the CO_2 transitions.
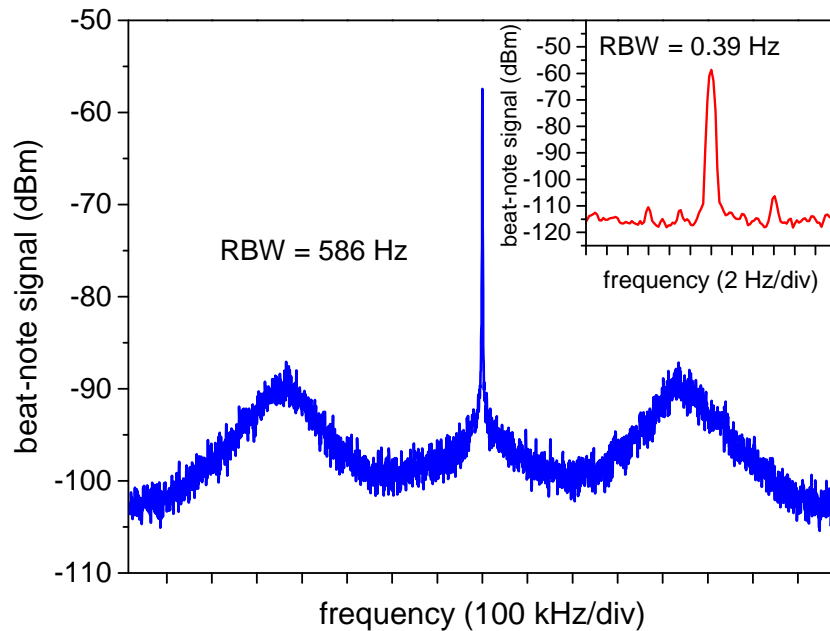

Figure 2.5: Beat-note signal between the DFG radiation and the phase-locked QCL. The inset shows the same beat note with a narrower span and resolution bandwidth. In both cases the width of the peak (FWHM) is limited by the resolution bandwidth of the spectrum analyzer.

two phase-locked sources. The locking bandwidth is limited by the dependence of the QCL tuning rate on the modulation frequency (see appendix A.5), as expected.[5] In fact, despite the completely different detector and electronics used, which are both much faster than those used in the other experiment (section 2.1.1), the same 250-kHz locking bandwidth is achieved, as confirmed by the servo bumps in the beat note. The phase-locking performance in terms of residual RMS phase error is measured by using the fractional power η contained in the coherent part of the beat-note signal, i.e. in the carrier. By evaluating the ratio between the area under the central peak of the beat note and the area under the whole beat-note spectrum (1.5-MHz wide), a phase-locking efficiency of η = 73% is obtained, yielding, through the relation [76]

$$\eta = e^{-\varphi_{RMS}^2} \tag{2.1}$$

a residual RMS phase noise of 0.56 rad.

The main portion of the QCL radiation is used for frequency-noise characterization and for spectroscopy. To the first purpose the QCL beam is coupled to a *high-finesse cavity*, which works as *frequency-to-amplitude converter*, when its length is tuned in order to have a transmission corresponding to half the peak value.[6] The cavity free spectral range is 150 MHz, and its finesse is about 9000 at $\lambda = 4.3\ \mu$m, as measured with the cavity-ring-down technique, leading to a mode FWHM of 18.8 kHz. The cavity output beam is detected by a second HgCdTe detector, and the resulting signal is processed by a FFT spectrum analyzer. In fig. 2.6 the FNPSD of the phase-locked QCL, acquired by using the high-finesse cavity, is shown. The same cavity has been also used to measure the DFG FNPSD and the QCL FNPSD when frequency-locked to a molecular line (see section 2.1.1). Such an independent converter allows for a fair comparison between the two basically different locking techniques. The plotted FNPSDs are compensated for the high-frequency cavity cut-off, due to the photon cavity ring-down rate ($f_c = 9.4$ kHz – see appendix A.1). The free-running QCL FNPSD, recorded by using the slope of the Doppler broadened CO_2 absorption line as converter, is shown. The comparison between free-running and phase-locked condi-

---

[5]Compare to section 2.1.1 and ref. [69].

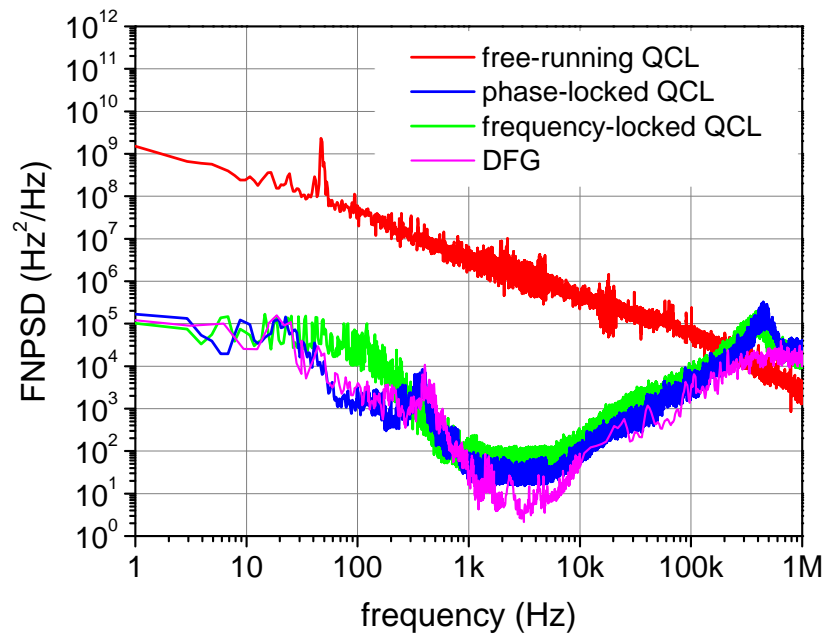[6]See appendix A.1 for a description of the calibration procedure of the frequency-to-amplitude converter.

Figure 2.6: QCL FNPSDs in free-running and phase-locked conditions, acquired by using a CO_2 line and the high-finesse cavity as frequency-to-amplitude converters, respectively. The cavity has been used also to measure the FNPSD of the DFG radiation and the FNPSD of the QCL when it is frequency-locked to a molecular absorption line (fig. 2.2). The residual $1/f$ trend between 30 Hz and 1 kHz on the DFG FNPSD is given by the the Nd:YAG. The QCL intensity noise is not shown here due to its relatively low level (more than two orders of magnitude lower than the related portion of the frequency noise spectrum). This gap is ensured by the steepness of the transmission of the high-finesse cavity used as frequency-to-amplitude converter (see appendix A.1).

tions confirms a locking bandwidth of 250 kHz, with a frequency noise reduction of about four orders of magnitude for frequencies up to 10 kHz. Moreover, the phase-locked-QCL FNPSD perfectly overlaps the DFG one, with only an excess noise above 200 kHz. If we compare the QCL FNPSD when phase/frequency locked to the DFG/molecular transition, they are almost coincident for Fourier frequencies above 1 kHz up to 450 kHz where a self-oscillation of both control loops is observed. This confirms that the locking bandwidth is limited by the laser modulation bandwidth (see appendix A.5). Nevertheless, a QCL linewidth narrower than 1 kHz (FWHM) on a time scale of 1 ms is retrieved in both cases by integrating the FNPSDs for frequencies above 1 kHz. As a consequence, we note that phase-locking the QCL does not improve laser narrowing with respect to frequency-locking. On the other hand, between 30 Hz and 1 kHz the two curves show different trends: in this range the phase-locked QCL FNPSD lies below that of the frequency-locked one, except for an evident noise peak centered at 400 Hz, which is also present in the DFG source. Apart from this peak, the comparison in this frequency range confirms a better control of the frequency jitter for the phase-locked QCL, overcoming the limits of the frequency-locked QCL set by the presence of a residual amplitude noise (see section 2.1.1). For Fourier frequencies below 30 Hz the high-finesse cavity is no more a good frequency-to-amplitude converter, since it saturates.

In order to confirm that the long-term frequency stability of the phase-locked QCL is limited by the OFC stability (6×10^{-13} on 1 s), we have measured the *Allan deviation* [7] of the DFG-QCL beat-note frequency. The result is 2.3 Hz at 1 s with a $\tau^{-1/2}$ trend up to 128 s, which is the last point used to compute the Allan deviation. Considering that the stability of this system is limited by the OFC one, we can state that we have gained a factor of about 70 in terms of stability with respect to the frequency-locked QCL. Moreover, the accuracy of the phase-locked QCL is traceable to the primary frequency standard at the 2×10^{-12} level (140 Hz at 4.3 μm). Therefore, we can conclude that the OFC-DFG phase-locked QCL, is a very suitable laser source for precision spectroscopy and metrological applications.

2.1.3 Single-frequency CO_2 spectroscopy

As a demonstration of the spectral performances of the phase-locked QCL (see section 2.1.2) in terms of resolution and precise frequency measurements in the mid infrared, sub-Doppler saturated-absorption spectroscopy of several lines of the CO_2 molecule around 4.3 μm in a 12-cm single-pass cell has been performed [73, 77]. Thanks to the PLL, the phase-locked QCL frequency is given by

$$\nu_{QCL} = \nu_{DFG} \pm f_{LO} = (N_p - N_s)f_r \pm f'_{LO} \qquad (2.2)$$

where we have expressed, in the last equality, ν_{DFG} in terms of the OFC parameters: repetition frequency f_r of the OFC, comb orders N_p (N_s) for the *pump* (*signal*) laser involved in the DFG process and a radio frequency f'_{LO}, which contains a balance of all local oscillator frequencies (including f_{LO}) used to lock the DFG radiation to the OFC. Scans of the synthesized absolute QCL frequency can be performed by changing the value of f'_{LO}.

The saturated-absorption setup, depicted schematically in fig. 2.4, uses less than 10 mW power from the QCL in a classical configuration of counterpropagating pump-probe beams (see section 1.1.6). Within the tuning range of the QCL (10–25 °C for temperature and 700–900 mA for current), the absolute center frequency of six CO_2 transitions belonging to the P branch of its $(01^1 1 - 01^1 0)$ ro-vibrational band can be measured (see section 1.1.3). In the saturated-absorption scheme, the Lamb dip at the center of the Doppler-broadened molecular line is detected. An optical chopper on the pump beam, combined with a lock-in detection, enables to cancel out the Doppler background due to the probe radiation and to retrieve the Lorentzian Lamb-dip profile with an optimal signal-to-noise ratio (S/N), when the absolute frequency of the phase-locked QCL is scanned across the Lamb dip by a stepwise tuning of the DFG source.

The recorded Lamb-dip spectrum of the P(34)f line is shown in fig. 2.7. Each data point represents the average of 10 samples, acquired by the lock-in amplifier with a chopping frequency of 2.49 kHz and a time constant of 10 ms. The 20-MHz scan is performed in 2 minutes with 50-kHz steps once forward and once backward across the Lamb-dip feature. In this way, any frequency shift caused by pulling effects of the lock-in integration is compensated for. In fig. 2.7 the fit curve and the
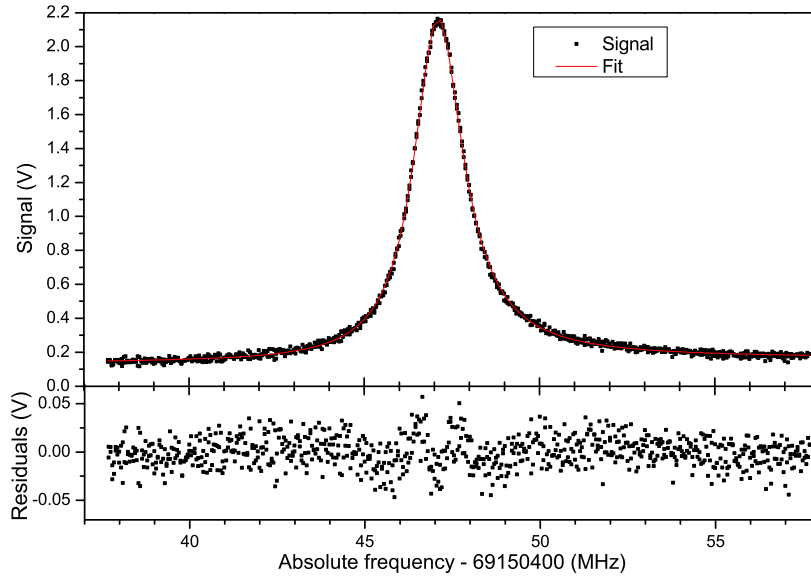
Figure 2.7: Lamb-dip recording of the P(34)f line at 2306.6108 cm^{-1} at 12 Pa and 295 K. The fit is a Lorentzian function corrected both for a linear amplitude modulation (as the QCL frequency is scanned by ramping its driving current) and a background signal of the lock-in amplifier.

corresponding residuals are also plotted. To fit the data, a function $g(\nu)$ of the following form has been used:

$$g(\nu) = A \cdot [1 + B(\nu - \nu_0)] \cdot L(\nu) + C \cdot [1 + D(\nu - \nu_0)] \qquad (2.3a)$$

$$L(\nu) = \frac{2}{\pi w} \left[1 + 4 \left(\frac{\nu - \nu_0}{w} \right)^2 \right]^{-1} \qquad (2.3b)$$

with A, w and ν_0 area, full-width and center of the Lorentzian curve, respectively. B is the slope coefficient due to the increment of the laser power related to the decrement of the frequency, C and D are the residual-background level and slope.

Thanks to the high precision/accuracy achieved by our setup, we are able to perform a series of acquisitions by varying the pressure of the CO_2 gas in a very small range (1–26 Pa). As an example, the acquisition related to the P(31)e line is reported in fig. 2.8. A weak linear dependence of the line centers on pressure is observed, as is generally expected for any molecular line (*pressure shift*). The extrapolated values at $P = 0$ yield the absolute frequencies for all the measured transitions, corrected for systematic self pressure shifts. Another example, the acquisition related
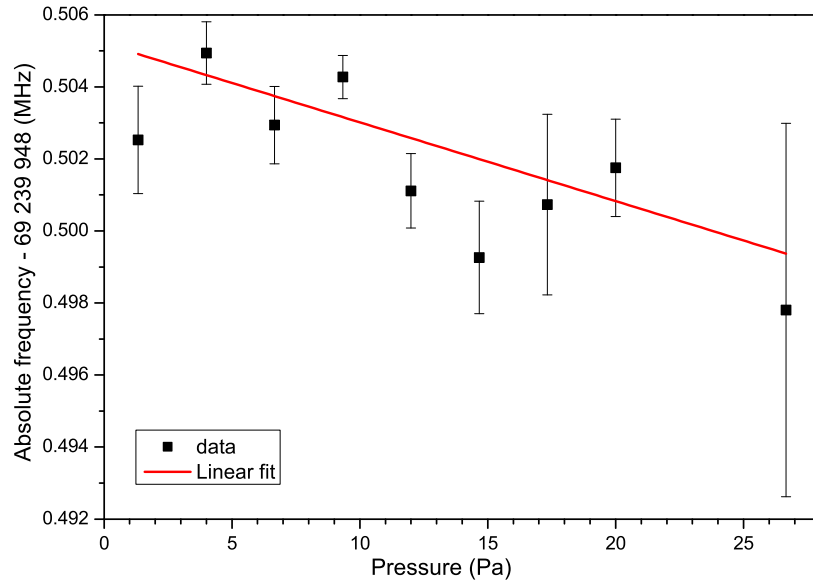
Figure 2.8: Measured self pressure shift related to the P(31)e line at 2309.5962 cm^{-1} at 295 K. Each data point represents 4 averaged line-center frequencies from fit results as shown in fig. 2.7.

to the P(29)e line is reported in fig. 2.9. The value extrapolated from this graph at $P = 0$, $\nu_{0\ P(29)} = (69297478.7978 \pm 0.0014)$ MHz is the absolute frequency of the transition (corrected by systematic pressure shift). This value is in agreement with that measured for the QCL frequency-locked to the same CO_2 transition (compare to the result in section 2.1.1) with an uncertainty improved by almost a factor of 20.

In table 2.1 the measured line-center frequencies (*obs. freq.*) and the measured self pressure shift coefficients (*press. shift*) are listed. The deviations with respect to two different sets of calculated values[7] (*Obs.-calc.*) are also reported. From the first comparison we note that the HITRAN frequency values are systematically blue-shifted by 4–5 MHz with respect to the observed ones, probably due to a miscalibrated spectroscopic apparatus [6]. Our measurements are 3–4 orders of magnitude more precise than the values extracted from the HITRAN database and thus they could be used to improve the molecular parameters of the $(01^11 - 01^10)$ ro-vibrational band (especially the band-center – see section 1.1.2). The last comparison shows that frequencies measured with a low-resolution (namely 162 MHz) Fourier-transform interferometer, when properly cal-

---

[7]These values are calculated using molecular parameters obtained by fitting some experimental data.
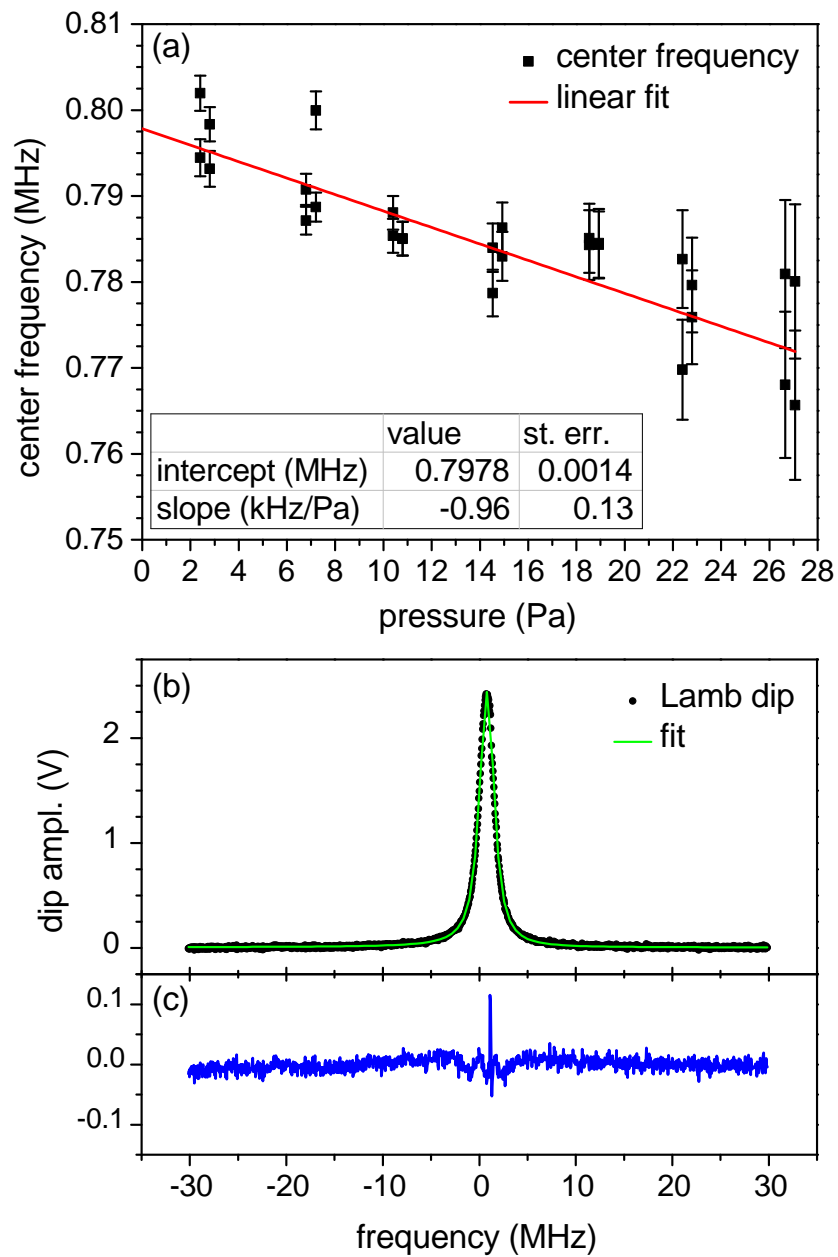
Figure 2.9: **a)** Dependence of the center of the Lamb dip of the CO_2 $(01^11 - 01^10)$ P(29)e transition on pressure, with the corresponding linear fit. For clarity, the constant value of 69297478 MHz has been subtracted from the absolute frequency values.
b) Example of a single Lamb dip acquisition. Experimental conditions: lock-in amplifier time constant 10 ms, chopper frequency 616 Hz, frequency scan with 60-MHz span and 50-kHz steps. The fit with a Voigt function (green line) and the residuals (**c**)) are also plotted.

Table 2.1: Observed line-center frequencies and self pressure shift coefficients for 6 transitions belonging to the $(01^11 - 01^10)$ ro-vibrational band of $^{12}C^{16}O_2$. Comparisons with calculated values are also reported.

transition	obs. freq. (MHz)	press. shift (kHz/Pa)	obs.-calc.[a] (MHz)	obs.-calc.[b] (MHz)
P(29)e	69 297 478.7998(31)	-1.37(52)	-4.0611	0.1362
P(30)f	69 267 227.7792(36)	-1.04(46)	-4.7036	-0.0321
P(31)e	69 239 948.5044(11)	-0.22(9)	-4.0039	0.3028
P(32)f	69 209 198.3778(8)	-0.16(9)	-4.6879	-0.1170
P(33)e	69 181 700.3740(18)	0.05(11)	-3.9287	0.0376
P(34)f	69 150 447.0863(14)	-0.22(10)	-4.6021	-0.1919

[a] Comparison with the HITRAN database [6]. The uncertainty reported by the original database for each transition is between 3 and 30 MHz.   [b] Comparison with ref. [78], where the frequencies of the same transitions measured with a low-resolution (162 MHz) Fourier-transform interferometer are reported.

ibrated, can achieve an absolute accuracy of few hundreds kHz. The 1–4 kHz precision achieved by the presented measurements is limited by both the Lamb-dip width and S/N, but neither by the spectral linewidth nor the accuracy of the absolute frequency of the QCL.

2.2 Frequency combs stabilization and spectroscopy

Compared to what presented in section 2.1, a tempting idea is to have OFCs operating *directly* in the MIR. Firstly they can serve as direct references for single-frequency MIR lasers, such as DFB QCLs. Even further, they can be used directly for MIR spectroscopy. An OFC radiation can give more spectroscopy information at a time than a single-frequency one, thanks to its instantaneous spectral coverage. The interest in using OFCs in this spectral region is related to applications such as trace-gas sensing with high-finesse cavities [4], high-precision spectroscopy and frequency metrology [27]. In order to perform high-sensitivity and resolution spectroscopy, it is again fundamental to have intense and narrow (low-frequency-noise) radiation. Moreover, if also a high accuracy is required, an absolute reference is again needed.

Pulsed mode-locked lasers have not yet been developed in the MIR, but their NIR spectra can be transferred to the MIR region (MIR-combs) taking advantage of non-linear frequency mixing. At the cost of being highly-sophisticated and bulky pieces of apparatus, such MIR-combs

have the advantage of being intrinsically metrological.[8] For applications like direct comb spectroscopy, where a high power spectral density is needed, MIR-combs were developed using optical parametric oscillators (OPO) [79, 80] or DFG systems using intense fiber-based NIR-combs [26, 28, 81]. In section 2.2.1 a method to obtain a low-frequency-noise and absolutely-referenced MIR-comb based on intracavity difference-frequency generation (DFG-comb) is described. In section 2.2.2 an application of this DFG-comb for CO_2 spectroscopy is presented.

A promising alternative for generating MIR-combs is represented by QCLs (QCL-combs). Since this technology is quite young [34], a further characterization is needed. In section 2.2.3 the frequency noise characteristic of such combs is presented. This study is essential both for spectroscopy applications as well as for a better understanding of the fundamental properties of the generated radiation. In section 2.2.4 an experiment where a QCL-comb is phase-locked through a single chain to the DFG-comb mentioned in section 2.2.1 is presented. This attempt is aimed both at the stabilization and at the further study of the coherence of the QCL-comb radiation.

2.2.1 Intracavity difference-frequency-generated mid-infrared frequency comb

For MIR-combs, values for total and per-tooth power of 1.5 W and 30 μW respectively, have been achieved [79]. In terms of spectral purity, the best so far reported values for the teeth linewidth are 30–40 kHz on a 1–2-s time scale [79, 81]. However, frequency down-conversion of combs from the NIR to the MIR may sometimes severely degrade the coherence [82].

With the following experiment, a method to obtain an absolutely-referenced MIR-comb, with a much increased spectral purity, has been proven [83]. The 1040-nm portion of the spectrum of a visible/NIR-comb (NIR-comb) is mixed with the intracavity radiation of a Ti:sapphire (Ti:Sa) laser in a non-linear crystal (DFG - see section 1.2.2). A DFG-comb centered around 4330 nm is thus generated. The excess frequency noise of the NIR-comb can be efficiently removed in the MIR one by properly implementing a direct digital synthesis (DDS) scheme. This leads to a 2.0 kHz tooth linewidth (on a 1-s time scale) of the generated DFG-comb. In addition, the high repetition rate ($f_r = 1$ GHz) and the

---

[8]Actually they are metrological *if* the original NIR OFC is metrological.

intracavity power-boosted DFG determine an average per-tooth power of 1 μW and thus a power spectral density at the μW/kHz level, comparable to the best results achieved with OPO-based MIR-combs.
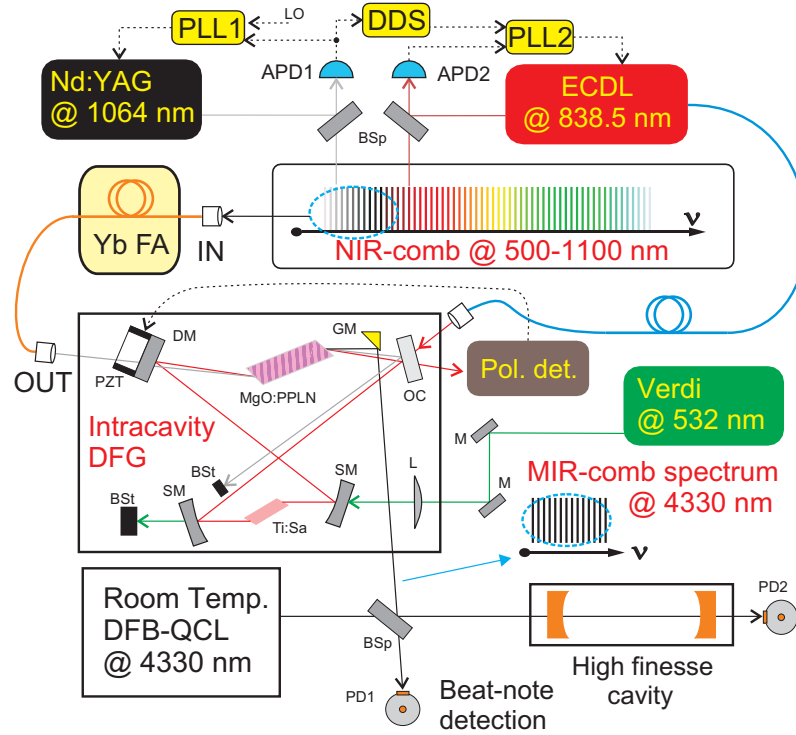
Experimental setup

Figure 2.10: Experimental setup: an Yb fiber amplifier (FA) is seeded by the NIR portion of the spectrum of the NIR-comb. The amplifier output is used as *signal* in a MgO:PPLN multiperiod crystal to generate MIR radiation, where the *pump* is the Ti:Sa intracavity radiation. The Ti:Sa laser is pumped by a Verdi laser and it is injection-locked by an ECDL. The DFG-comb (MIR-comb) beam is coupled into a high-finesse cavity and beaten with a room temperature DFB QCL for characterization purposes.
PLL: phase-locked loop, DDS: direct digital synthesis, APD: avalanche photodiode, BSp: beam splitter, PZT: piezoelectric transducer, DM: dichroic mirror, MgO:PPLN: periodically-poled lithium niobate crystal doped with magnesium oxide, GM: gold mirror, OC: output coupler, Pol. det.: polarization detection and electronic control loop, BSt: beam stopper, M: mirror, SM: spherical mirror, L: lens, Ti:Sa: titanium sapphire crystal, PD: photovoltaic detector.

In fig. 2.10 the experimental setup is reported. The setup, similar to that reported in ref. [75] for single-frequency DFG, is based on a mode-locked Ti:Sa laser with a repetition rate f_r of about 1 GHz

(see section 1.3.2), spectrally broadened to one octave operation range (500–1100 nm) by a photonic-crystal fiber (NIR-comb). The oscillator controlling f_r is referenced to a Rb/GPS-disciplined 10-MHz quartz clock with a stability of 6×10^{-13} at 1 s and an accuracy of 2×10^{-12} (see section 1.3.4). The portion of the NIR-comb spectrum above 1-μm wavelength is selected by a dichroic mirror and sent to an Yb^{3+} fiber amplifier. The output radiation, whose spectrum is limited by the amplifier gain bandwidth (fig. 2.11), is injected into the Ti:Sa laser cavity by another dichroic mirror. The amplifier output is used as *signal* in a
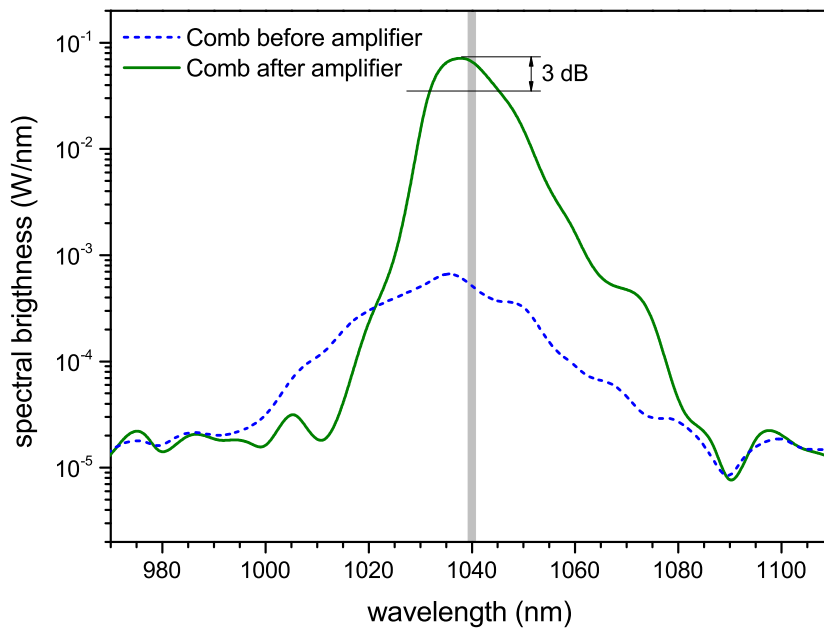
Figure 2.11: NIR-comb spectrum before and after the Yb fiber amplifier. The 1.6-nm-wide gray region indicates the portion of the spectrum effectively involved in the DFG-comb generation, essentially limited by the phase-matching bandwidth of the DFG process (see section 1.2.3).

MgO:PPLN multiperiod non-linear crystal [15] to generate *idler* radiation (DFG-comb), where the *pump* is the intracavity Ti:Sa radiation. The MIR radiation is extracted from the cavity taking advantage of different refraction angles at the facet of the crystal, cut at the Brewster angle for the *pump*. The Ti:Sa laser is optically injected by an external-cavity diode laser (ECDL) in order to make it unidirectional and single frequency. To keep the optical injection, the Ti:Sa cavity length is stabilized against the ECDL frequency by an electronic control loop using the polarization-based Hänsch-Couillaud technique [84]; the feedback signal is sent to

a piezoelectric acting on one of the cavity mirrors. The ECDL wavelength is set to 838.5 nm in order to obtain a DFG-comb centered around 4330 nm with a *signal* at 1040 nm, in coincidence with the most intense portion of the amplified NIR-comb (fig. 2.11). The DFG scheme, considering the 838–863 nm tuning range of the *pump* laser injecting source (ECDL) and the 1032–1045-nm-wide spectrum of the *signal* (NIR-comb spectrum after the amplifier), provides a tunability of the MIR central wavelength from 4.2 to 5.0 μm. The crystal temperature (and eventually the period) needs to be accordingly varied in order to ensure the quasi-phase-matching condition (see section 1.2.3). The tuning limits for the central wavelength are given by the edges of the ECDL tuning range and the NIR-comb spectrum. Actually, the upper limit at around 5.0 μm is imposed by the absorption of the PPLN crystal. The DFG-comb spectrum is limited by the PPLN crystal phase-matching bandwidth, which is 27-nm wide FWHM at 4330 nm (see section 1.2.3). This means that the portion of the NIR-comb spectrum effectively involved in the DFG-comb generation is 1.6-nm wide (see fig. 2.11). With a 5 W total power out from the amplifier and 30 W Ti:Sa intracavity power, the obtained power of the DFG-comb is 0.5 mW. Considering such an *idler* power, the *pump* radiation is reduced by 2.5 mW.[9] This value is negligible with respect to the total intracavity *pump* power (30 W), therefore the losses related to the DFG process are negligible [75].

In order to have a DFG-comb with narrow-linewidth teeth, the excess noise of the NIR-comb due to repetition rate fluctuations ($N_s \times f_r$, with N_s order number of one of the down-converted NIR teeth) must be replicated by the *pump* frequency, to be canceled in the DFG process. An intermediate stable oscillator operating around the *signal* frequency (a Nd:YAG laser) and a DDS electronic scheme similar to that adopted in the experiment reported in section 2.1.2 are used to that purpose (see appendix A.7). ECDL and Nd:YAG frequencies (ν_p and ν_Y respectively) are beaten with the NIR-comb nearest teeth and the beat-note frequencies are

$$f_p = \nu_p - N_p f_r - f_o \tag{2.4a}$$

$$f_Y = \nu_Y - N_Y f_r - f_o \tag{2.4b}$$

---

[9]The *pump* photons are 5 times more energetic than the *idler* ones.

where f_p and f_Y are the beat-note frequencies of the ECDL and the Nd:YAG respectively, f_r and f_o are the repetition rate and the carrier envelope offset of the NIR-comb respectively, and N_x is the integer identifying the tooth used for the beat note. f_o is canceled from f_Y using standard RF mixing, then the DDS multiplies $f_Y + f_o$ by a factor $(N_p - N_s)/N_Y$. A phase-locked loop (PPL2) is used to control the *pump* beat note f_p against the DDS output with a large bandwidth (2 MHz), using the driving current and the external-cavity grating position as actuators. In these conditions $f_p = (f_Y + f_o)(N_p - N_s)/N_Y$ and using eq. 2.4 the *pump* frequency can be written as

$$\nu_p = (f_Y + f_o)\left(\frac{N_p - N_s}{N_Y}\right) + N_p f_r + f_o$$
$$= (\nu_Y - N_Y f_r)\left(\frac{N_p - N_s}{N_Y}\right) + N_p f_r + f_o \tag{2.5}$$

and the frequency of the DFG-comb tooth (*idler*) obtained as difference between the *pump* laser and the *signal* NIR-comb tooth results

$$\nu_i = \nu_p - N_s f_r - f_o = \left(\frac{N_p - N_s}{N_Y}\right)\nu_Y \tag{2.6}$$

It is worth noting that an absolute frequency traceability of the generated ν_i is obtained by controlling the frequency of the Nd:YAG laser against the nearest tooth of the NIR-comb: a PLL (PLL1 in fig. 2.10) with a bandwidth of 10 Hz corrects for Nd:YAG frequency drifts acting on the Nd:YAG crystal temperature, without perturbing its linewidth. Moreover, from eq. 2.6 we note that the frequency fluctuations of ν_i depends only on ν_Y and are independent of the NIR-comb parameters (f_r and f_o), giving narrow DFG-comb teeth. The factor $(N_p - N_s)/N_Y$ is about $1/4$ in our case and, considering a Nd:YAG laser linewidth of about 5 kHz on a 1-s time scale, a linewidth of about 1 kHz of the DFG-comb teeth is expected. It is important to observe that a perfect cancellation of f_r can only be obtained for the tooth N_s, whereas, for the tooth $N_s + m$ (m is the integer that enumerates the DFG-comb teeth), the additional fluctuations amount to $m \times \delta f_r$. The fluctuations for a generic DFG-comb tooth can be expressed as

$$\delta \nu_{i,m} = \left(\frac{N_p - N_s}{N_Y}\right)\delta \nu_Y + m\delta f_r \tag{2.7}$$

In our case the two terms are of the same order of magnitude, therefore they contribute to the noise at the same level.

The DFG-comb beam is coupled to a high-finesse cavity to study its FNPSD, and it is beaten with a previously frequency-calibrated QCL at 4.33 μm in order to characterize its frequency components. A sequence of beat notes spaced by 1 GHz is measured as the QCL frequency is scanned. This confirms the value of the center wavelength emission of the generated DFG-comb and the value of f_r as expected, otherwise difficult to measure due to the lack of fast photodetectors in the MIR region.

Characterization

The 1-m-long high-finesse cavity (free spectral range FSR = 150 MHz) is made of two plano-concave ZnSe mirrors, with high-reflectivity coatings on the concave surfaces (6 m radius of curvature) [70]. At this wavelength (4.33 μm) the finesse is 9000. To maximize the transmitted signal we have matched f_r with the following Vernier ratio [85] (see appendix A.6):

$$f_{r0} = \frac{20}{3} \, \text{FSR} = \frac{20}{3} \, \frac{c}{2L_0} \tag{2.8}$$

which corresponds to a given cavity length L_0. In this condition the cavity selects a subset of comb teeth (one every three), that gives rise to the peak shown in fig. 2.12a (the first peak in fig. 2.12b). While keeping f_r constant, if the cavity length L is changed, other resonances can be observed between the comb and the cavity, for $L_1 = L_0 + \lambda/6$ (second peak), $L_2 = L_0 + \lambda/3$ (third peak) and $L_3 = L_0 + \lambda/2$ (fourth peak), where λ is the mean wavelength of the radiation (fig. 2.12b). However, the condition expressed in eq. 2.8 is valid only for the first subset of teeth. For the other cavity lengths L_n only the central comb tooth m_{0n} of the corresponding subset is resonant with a cavity mode. Neglecting the cavity dispersion, the frequency mismatch of the tooth m (again one every three) with the nearest cavity resonance is given by $[f_r - (20/3)(c/2L_n)](m - m_{0n})$. Therefore the width of the peak for $L = L_n$ is

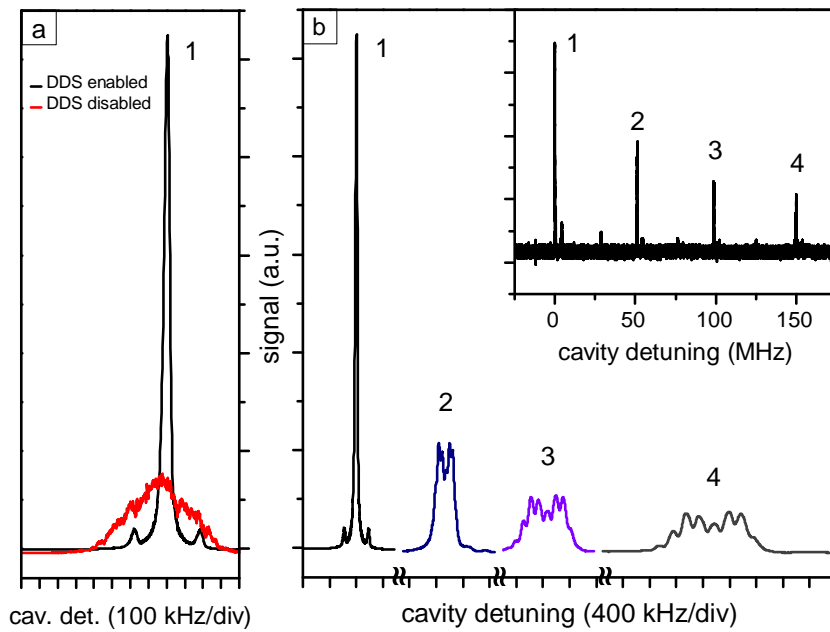$$W_{\text{pk}} = \left(f_r - \frac{20}{3} \frac{c}{2L_n} \right) M_{\text{tot}} \tag{2.9}$$

Figure 2.12: Transmission peaks of the high-finesse cavity recorded for different cavity detunings. **a)** The peak corresponding to eq. 2.8, recorded in two different ECDL phase-locking operating regimes: with operating DDS (black line, 30 kHz FWHM), and with simple phase locking to the nearest NIR-comb tooh (red line, 400 kHz FWHM). **b)** 1-FSR-wide cavity scan (inset) with zooms on consecutive longitudinal resonances spaced by FSR/3 = 50 MHz.

where M_{tot} is the total number of the DFG-comb teeth. Eq. 2.9 enables to estimate M_{tot}. As an example, the measured width of the third peak is $W_{\text{pk}} = 630$ kHz FWHM. Since in this case

$$f_r - \frac{20}{3}\frac{c}{2(L_0 + \lambda/3)} = 1.44 \text{ kHz} \tag{2.10}$$

a total teeth number $M_{\text{tot}} = 440$ is obtained. Calculations on the other peaks give consistent results that, recalling the total comb power, allow to estimate an average per-tooth power of 1 μW. This is also in agreement with the expected spectral coverage of the DFG-comb retrieved by the phase-matching bandwidth of the DFG process at this wavelength (see section 1.2.3).

Figure 2.12a also shows the effect of the phase-locking technique on the *width* of the DFG-comb teeth. The width of the black peak, corresponding to the locking scheme described above (with operating DDS for the ECDL phase locking), is 30 kHz FWHM, limited both by the cavity mode and by the dispersion of the teeth due to the cavity mirrors. On the other hand, the red peak, corresponding to a standard phase locking of the ECDL to the nearest NIR-comb tooth (without DDS), is much wider (about 400 kHz FWHM), confirming that the DDS really provides narrower DFG-comb teeth.

In order to estimate the coherence of the DFG-comb we have used the high-finesse cavity as *multimode frequency-to-amplitude converter* to retrieve the FNPSD of the radiation in the condition established by eq. 2.8 (see appendix A.2 for a demonstration). The factor used to convert amplitude fluctuations to frequency fluctuations is the slope of the first peak of fig. 2.12 at half maximum (see appendix A.1). Due to the photons average lifetime, the cavity acts as a second-order low-pass filter with a 9.4 kHz cutoff frequency. The spectrum reported in fig. 2.13 is compensated for this cutoff. Using Elliott's formula to calculate the linewidth of the comb teeth (eq. 1.127), a value of 2.0 kHz FWHM on a 1-s time scale and 750 Hz on a 20-ms time scale is obtained. Taking into account the DFG-comb power, a per-tooth power spectral density of 0.5 μW/kHz (on a 1-s time scale) is obtained, value which is comparable with the best performing OPO-based MIR-combs [79, 80]. It is worth noting that this power level is in a range suitable for direct comb spectroscopy in this spectral region.
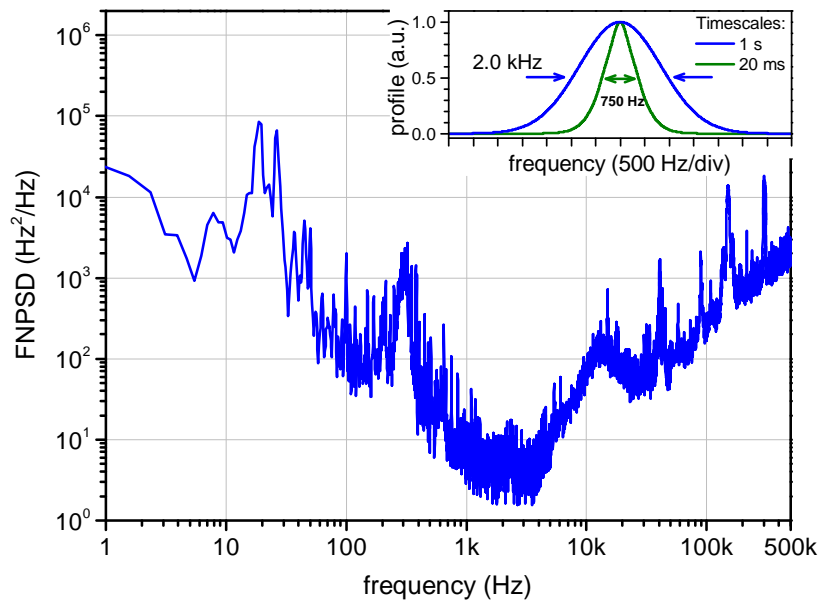
Figure 2.13: FNPSD related to the DFG-comb radiation retrieved by using the high-finesse cavity as frequency-to-amplitude converter. The spectrum analyzer is set in max-hold acquisition mode to be sure to collect the maximum amplitude for each frequency interval. The spectrum is compensated for the 9.4 kHz cavity cutoff. **Inset:** power spectrum profile of the DFG-comb teeth on different time scales, calculated from the FNPSD using eq. 1.127.

2.2.2 Frequency comb CO_2 spectroscopy

In this section the metrological and spectroscopic performances of the DFG-comb presented in the previous section (2.2.1) will be discussed. The DFG-comb is used both as an accurate and highly-stable phase/frequency reference for a continuous-wave quantum cascade laser at 4330 nm, thus enabling high-precision spectroscopy with a powerful and narrow-linewidth MIR source, and as a multi-frequency highly coherent MIR source to perform high-sensitivity broadband direct comb spectroscopy in ambient air with the Vernier technique [86].

By using the experimental setup shown in fig. 2.14, a room-temperature continuous-wave DFB QCL operating around 4330 nm is phase-locked to a single tooth of the DFG-comb (see section 2.2.1 for details on its generation). This is done by superimposing a fraction of the QCL
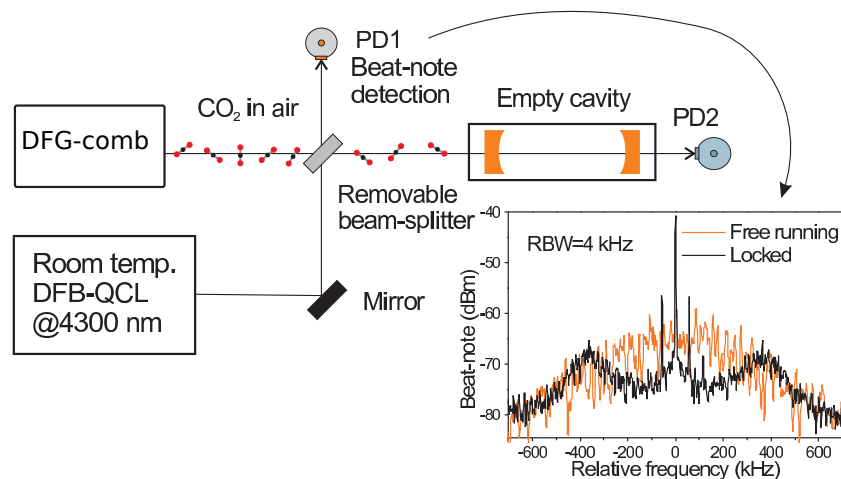
Figure 2.14: Experimental setup. A continuous-wave DFB QCL is phase-locked to a single tooth of the DFG-comb. Alternatively, the DFG-comb is coupled to a high-finesse cavity for spectroscopy purposes. **Inset**: beat note between the QCL and one DFG-comb tooth, in both free-running and phase-locked conditions.

beam (about 1 mW) with the DFG-comb beam and sending them to a liquid-N_2-cooled HgCdTe photodetector (200-MHz bandwidth - PD1). Figure 2.14 shows the detected beat note between the QCL and the nearest comb tooth, as recorded by a RF spectrum analyzer. The beat-note frequency is phase-locked to a local oscillator provided by a RF signal generator, by using a home-made phase-detection electronics with hybrid analog/digital architecture. The phase-error signal is processed by a PID

controller. The servo bumps confirm a phase-locking bandwidth of about 400 kHz, mainly limited by the QCL frequency modulation behavior (see appendix A.5). The phase-locking efficiency $\eta = 73\%$ is estimated as the ratio between the areas of the resolution-bandwidth-limited carrier and the whole beat-note spectrum. Using again eq. 2.1 we can estimate a residual RMS phase-noise $\varphi_{RMS} = 0.56$ rad, as an evaluation of the PLL performance. This value is the same compared to the one obtained with the experiment reported in section 2.1.2 where the laser is the same, confirming that it is the QCL that limits the performances of the locking. It is remarkable that the possibility of phase locking the QCL to one arbitrary DFG-comb tooth within its working range (which for a standard DFB QCL spans about 300 GHz) makes the DFG-comb itself a sort of universal absolute frequency reference for this class of lasers.

A free-running QCL linewidth of about 400 kHz is inferred from the free-running beat note of fig. 2.14, by considering the few kHz linewidth measured for the DFG-comb tooth (see section 2.2.1). Instead, a full characterization of the phase-locked QCL linewidth behavior on different time scales can be only retrieved by measuring its FNPSD (see section 1.4.3). To that purpose, we used an empty 1-m-long high-finesse Fabry-Pérot cavity (finesse $F \approx 9000$ at 4330 nm) as frequency-to-amplitude converter. Figure 2.15 shows a comparison between the FNPSD of the phase-locked QCL and the one of the DFG-comb (fig. 2.13). Both the spectra have been compensated for the cavity cut-off (see appendix A.1), corresponding to a 8.5 μs ring-down time for resonant photons. The quite good agreement between the two recorded noise spectra confirms that measuring the FNPSD of many comb teeth together (simultaneously in resonance with the optical cavity – the so-called *multimode frequency-to-amplitude conversion* – see appendix A.2 for a demonstration) yields the same result as measuring the FNPSD of a single comb tooth. It is worth noting that this further confirmation of the DFG-comb high-coherence degree is enabled by the phase-locked QCL, used as a tracking oscillator amplifying a single comb tooth, otherwise too weak to be measured. By integrating the FNPSD spectrum of the phase-locked QCL using eq. 1.127, a linewidth of about 4.6 kHz over 1 s is obtained, with a narrowing factor compared to the free-running operation of about 100. This value is a bit larger than what is measured for the DFG-comb (2 kHz), mainly due to residual $1/f$ frequency noise of the QCL. Such a single-frequency narrow-linewidth
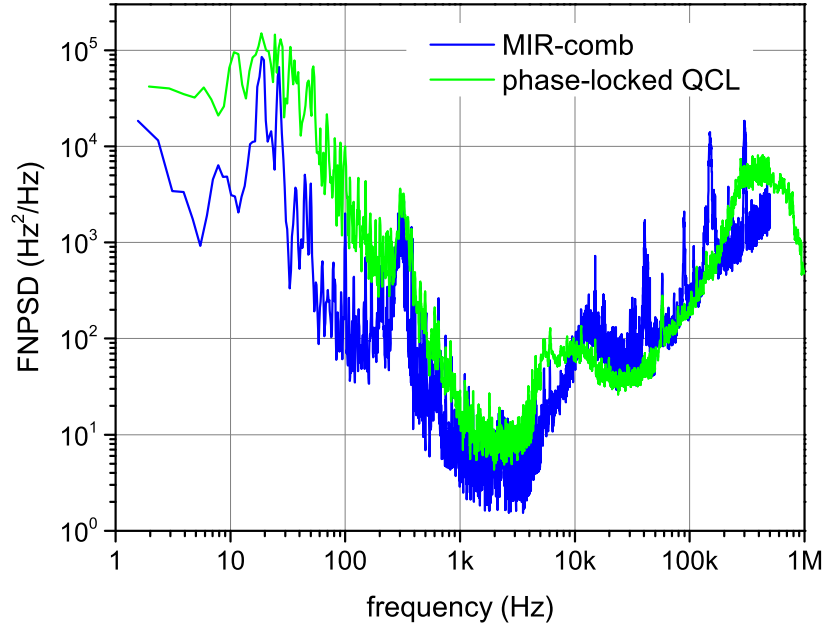
Figure 2.15: Comparison between the FNPSD measured for the DFG-comb (MIR-comb – see fig. 2.13) and for the phase-locked QCL, retrieved by using the optical cavity as frequency-to-amplitude converter. The DFG-comb trace is noisier than the QCL one, due to lower available power.

absolutely-referenced MIR source with tens of milliwatt of power can serve as a unique tool to perform high-precision/sensitivity molecular spectroscopy, also exploiting recently developed sub-Doppler techniques [87].

Alternatively, the multi-frequency DFG-comb itself can be used for broadband *direct comb spectroscopy*. A convenient technique to go this second way is the Vernier technique [88], that proved to be able to resolve all individual teeth of the DFG-comb, as described below. This approach is enabled by the high-enough average power (about 1 μW) and narrow linewidth (about 2 kHz) of each tooth. Since the optical cavity has a free spectral range FSR $\approx$ 150 MHz and the signal NIR-comb has a repetition rate $f_r \approx$ 1 GHz, the simplest Vernier ratio to make the DFG-comb teeth simultaneously resonant with the cavity is the one reported in eq. 2.8 (20/3 – see appendix A.6). In order to resolve the single teeth, the repetition rate f_r of the NIR-comb has to be slightly detuned from the value f_{r0} that perfectly satisfies the resonance Vernier condition of eq. 2.8. We scanned the cavity length by applying a voltage ramp to three piezoelectric actuators moving one of the two mirrors.

In fig. 2.16 the measured spectrum of the DFG-comb transmitted by the empty cavity is reported. The signal is detected by a liquid-N_2-cooled InSb photodetector (1-MHz bandwidth – PD2 in fig. 2.14). The
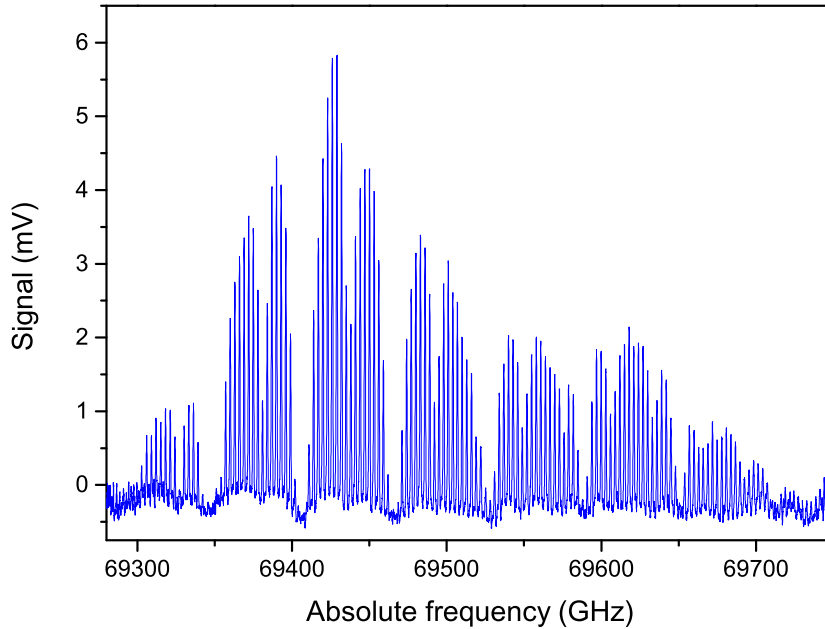

Figure 2.16: DFG-comb spectrum resolved with the Vernier technique: only one of the 3 sub-combs is shown (see fig. 2.12 and appendix A.6).

DFG-comb spectrum exhibits a FWHM of about 200 GHz, due to the spectral bandwidth of the quasi phase matching (see section 1.2.3), with strong amplitude inhomogeneities, mainly due to the absorption of CO_2 molecules in ambient air over a 2-m path-length. The absolute frequency scale is retrieved in two steps. Firstly, a relative linear frequency scale is calculated by fitting the length-to-voltage response of the piezoelectric actuators to a 5th-order polynomial curve, by using the comb teeth as frequency markers with spacing equal to $3f_r$. Secondly, the molecular absorption features in ambient air are used (as a natural wavemeter) to retrieve the integer order numbers of the teeth.

The spectrum plotted in fig. 2.16 is measured by averaging 80 scans of the optical cavity length and the measured FWHM of each single tooth corresponds to 55 kHz, which is wider than the cavity resonance linewidth (about 19 kHz), mainly due to cavity drift during the averaging time (4.75 s).

Given the 20/3 Vernier ratio, when scanning the cavity length by a

complete FSR, 3 sub-combs are acquired, each of them with a teeth spacing $3f_r$ and shifted with respect to the others by $\pm f_r$ (see appendix A.6). After properly interlacing the 3 sub-combs, we obtain the overall DFG-comb spectrum with a teeth spacing f_r. Actually, the spectrum of the generated DFG-comb depends both on the parent NIR-comb and on the quasi-phase-matching relation. Therefore, to make the spectroscopic analysis easier, the experimental data have been normalized to make the amplitude of the DFG-comb teeth as flat as possible. This is done by dividing the original spectrum by an envelope Gaussian curve with proper center and width. The central portion of the processed spectrum is shown in fig. 2.17. The transmission spectrum through a 2-m path-
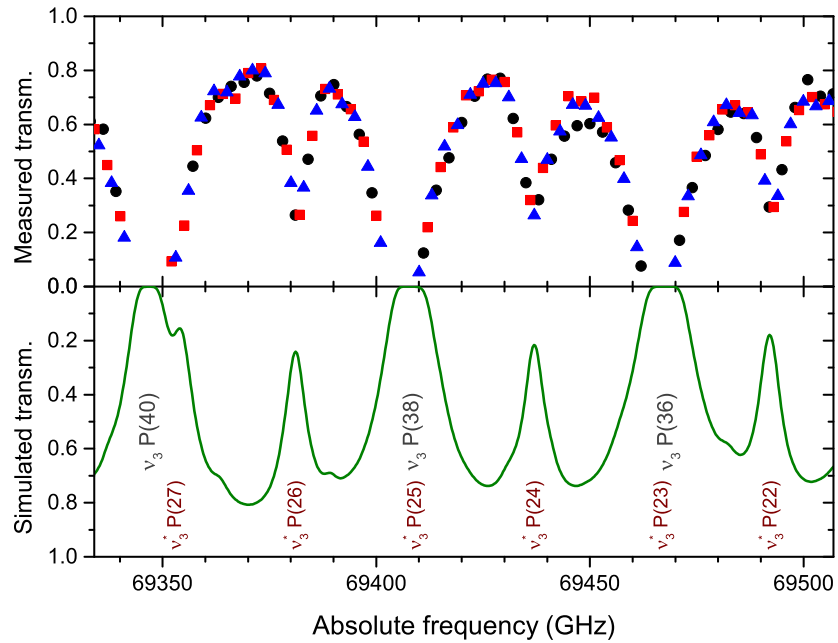
Figure 2.17: Central portion of the DFG-comb air transmission spectrum measured with the Vernier technique; circles, squares and triangles identify the 3 interlaced sub-combs. Below the HITRAN simulation [6] is plotted, and the CO_2 ro-vibrational transitions of two bands are also labeled: $\nu_3(00^01 - 00^00)$ and $\nu_3^*(01^11 - 01^10)$.

length in ambient air, as simulated by the HITRAN 2012 database [6], is plotted in the same figure. The agreement between the experimental DFG-comb transmission spectrum in air and the HITRAN simulation is very good. This is an interesting portion of the electromagnetic spectrum to be analyzed. Indeed, the characteristic CO_2 absorption at this wavelength (4.3 μm) is clearly visible, in particular the lines belonging to the

$(00^01 - 00^00)$ and $(01^11 - 01^10)$ bands (see section 1.1.3).

2.2.3 Quantum-cascade-laser comb frequency noise

A promising alternative for generating MIR-combs is represented by QCLs. As stated in section 1.5.4, for mid-infrared QCLs, the upper-state lifetime is very short (≈ 0.3 ps) compared to the cavity round-trip time.[10] This is responsible for a tendency to operate with a nearly constant output power, damping any energy spike propagating at the round-trip frequency within the cavity. Nonetheless, in multimode-operating devices, a residual amplitude modulation in the emitted radiation is present, enabling to observe a beat-note signal at the round-trip frequency. This signal is also present in the laser current and is detectable through a bias-tee.[11] QCL-combs have been initially characterized by measuring the autocorrelation of the intermode beat note at the cavity round-trip frequency (around 7 GHz for 6-mm-long devices), performing a so-called beat-note spectroscopy [34], which consists in the detection of the beat note given by only a subgroup of modes. This selection is obtained using a Fourier transform interferometer (FTIR). A more sensitive technique is provided by comparing two QCL-combs in a heterodyne beat experiment. An experiment on QCLs arranged in a dual-comb spectroscopy setup demonstrated a mode equidistance fractional accuracy of 7.5×10^{-16} relative to the carrier (optical frequency) [89], a value close to those measured for microresonator-based Kerr combs [29].[12]

Single-frequency QCLs frequency noise has been widely investigated [66, 68, 69, 90, 91]. With the following experiment, the *frequency noise* of a QCL-comb has been investigated for the first time [92]. This characterization is essential both for spectroscopy applications as well as for a better understanding of the fundamental properties of these devices with such a unique comb formation mechanism. The generation of the comb of frequencies is interpreted within the framework of *supermodes*. A high-finesse optical cavity is used as multimode frequency-to-amplitude converter to retrieve the QCL-comb intrinsic linewidth (see appendix A.2

---

[10] The cavity round-trip time is about 140 ps for 6-mm-long devices.

[11] Due to the short upper-state lifetime, QCLs are able to *detect* the beating between their own modes.

[12] A comparison between QCL-combs and microresonator-based Kerr combs makes sense, since in both cases the phenomenon that gives the mode locking is FWM (see section 1.2.4).

for a demonstration). A comparison among the obtained linewidths is also given, demonstrating that the FWM effectively correlates the quantum noise of the comb modes.

Frequency noise

What distinguishes a frequency comb from a simple array of perfectly equally-spaced single-frequency optical sources is the correlation of the frequency noise. While the heterodyne beat of two independent single-frequency laser sources always yields a linewidth wider than that of the individual lasers, this is not the case if the two single frequencies are extracted from a frequency comb source. These considerations are equally true for technical as well as for quantum noise. The *intrinsic linewidth* of a semiconductor laser is given by the Schawlow-Townes-Henry formula (eq. 1.131). It is proportional to the ratio of the number of photons emitted in the cavity by spontaneous emission over the total number of photons circulating in the cavity. As compared to a single-frequency device, we observe that the only effect of comb operation is the redistribution of the stimulated photons into equally spaced modes with a negligible additional frequency noise. For this reason, the intrinsic linewidth of single comb modes is expected to be unchanged and can be expressed by the Schawlow-Townes formula considering the total optical power of all comb modes.

Similar to microresonator-based combs, QCL-combs are generated through FWM (see section 1.2.4). For this reason, according to a semi-classical approach to QCL-combs [64, 65], it makes sense to compare the quantities with the quantum formalism developed for microresonator-based combs [93]. This permits the retrieval of the Langevin equation for the photon annihilation operator related to the *n*-th QCL-comb mode:

$$\dot{\hat{a}}_n = \underbrace{\left(\frac{G_n - 1}{2\tau_c} + iD_n \right) \hat{a}_n}_{\text{gain \& dispersion}} - \underbrace{\frac{G_n}{2\tau_c} \sum_{k,l} C_{kl} B_{kl} \, \hat{a}_k^\dagger \hat{a}_m \hat{a}_l \, \kappa_{n,k,l,m}}_{\text{FWM}} + \underbrace{\frac{1}{\tau_c} \hat{V}_n}_{\text{noise}} \quad (2.11)$$

with

$$G_n = \frac{i\gamma_{12}}{2\pi n f_s + i\gamma_{12}} g_0$$

$$D_n = -\frac{\pi\delta_n^2}{f_n} - 2\pi \delta_n$$

$$C_{kl} = \frac{\gamma_{22}}{\gamma_{22} - 2\pi i (l-k) f_s}$$

$$B_{kl} = \frac{\gamma_{12}}{2i} \left(\frac{1}{2\pi k f_s - i\gamma_{12}} - \frac{1}{2\pi l f_s + i\gamma_{12}} \right)$$

where $\kappa_{n,k,l,m}$ is the spatial superposition integral among the modes involved in the FWM, τ_c is the photon lifetime in the laser cavity, γ_{22} is the scattering rate out of the excited laser state, γ_{12} is the loss of coherence of the laser transition, f_s is the comb mode spacing (without dispersion), g_0 is the peak gain, δ_n is the difference between the frequency of the n-th mode of the ideal laser cavity f_n and the frequency of the n-th mode of the laser cavity with dispersion. The coefficients G_n and D_n represent the complex gain coefficient for the mode n and the modal dispersion, respectively. The coefficient C_{kl} represents the amplitude of the coherent population oscillations. The coefficient B_{kl} represents the bandwidth of the FWM gain and determines how many modes contribute to the FWM process. $\hat{V}_n$ are the vacuum Langevin noise operators related to the optical loss processes (waveguide and mirrors) [93, 94], characterized by the following statistical properties:

$$\langle \hat{V}_n(t) \rangle = 0 \tag{2.12a}$$

$$\langle \hat{V}_n^\dagger(t) \hat{V}_n(t') \rangle = \delta(t-t') \tag{2.12b}$$

$$\langle \hat{V}_n(t) \hat{V}_n(t') \rangle = 0 \tag{2.12c}$$

The product of the terms G_n, C_{kl} and B_{kl} can be linked to the third-order nonlinear susceptibility $\chi^{(3)}$ [64, 65]. Thanks to the FWM term, eq. 2.11 ensures that in comb operation the average relative phases of the modes are fixed. Therefore, through a unitary transformation, it is possible to select a new basis for the cavity modes, the *supermodes* basis, such that one of these supermodes corresponds to that selected by the comb operation [95] (see section 1.3.1). The new annihilation operators are given by

$$\hat{b}_q = \sum_n U_q^n \hat{a}_n \tag{2.13}$$

where U_q^n is the element of a unitary matrix such that $U^{-1} = U^\dagger$ [96]. In this way, the equation is reduced to that of a single-mode laser (with only one mode excited). In particular, the Langevin operators for the new modes

$$\hat{V}'_q = \sum_n U_q^n \hat{V}_n \qquad (2.14)$$

will have the same correlation properties (eq. 2.12) because of the unitary nature of the transformation. The resulting frequency noise is expected to be the same as that of a single-mode laser.

Experiment

The laser used for these experiments is a QCL-comb based on an In-GaAs/InAlAs broadband design with multiple active regions (multistack – see section 1.5.3), previously reported in ref. [34]. It operates in continuous wave at room temperature, emitting several milliwatts of power at 7.10 μm on a single transverse mode. The device length is 6 mm, corresponding to $f_s \approx 7.5$ GHz (multi-longitudinal-mode emission). The comb mode spacing f_s can be measured as a radio-frequency (RF) modulation arising directly on the laser-biasing current and extracted from the device through a bias-tee [89]. Two main operating regimes are observed in this device. Just above the laser threshold, the device emits single-mode radiation and we do not observe any RF beat note. Above a second current threshold, a *comb regime* is observed for a significant part of the device working range (see fig. 2.18, bottom), where a narrow RF beat note on the laser current corresponding to f_s is observed. In comb regime, the laser emits a single coherent comb of frequencies. The presence of these two operating regimes allows the study of the frequency noise in both the regimes using the same device. In order to investigate the FNPSD, a high-finesse optical cavity (*Fabry-Pérot*, $\mathcal{F} \approx 6000$) is used to resolve the laser spectrum and to detect the frequency fluctuations of the laser, acting as frequency-to-amplitude converter (fig. 2.18, top). A pair of high-reflectivity mirrors (99.96% of declared reflectivity) coated with dielectric layers is used to build a self-made cavity suitable for our experiments. In the setup, an optical isolator (transmission $T = -2.9$ dB, extinction $E = -33$ dB) is employed to avoid the instabilities induced on the laser by the back-reflection from the input mirror of the cavity. To collect the signal transmitted by the cavity, a high-sensitivity nitrogen-
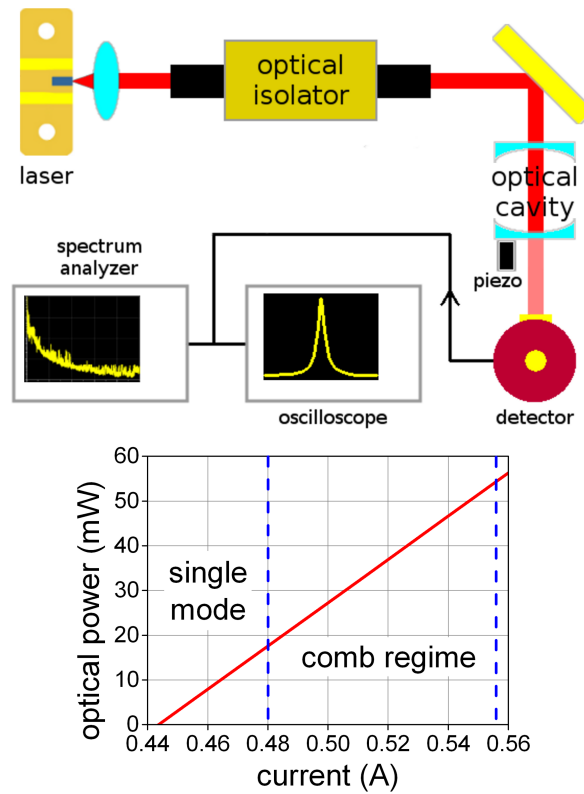
Figure 2.18: **Top:** Experimental setup used to measure the FNPSD of the laser. The main optical components include the laser (a multistack InGaAs/InAlAs QCL), the optical isolator, the high-finesse optical cavity and the high-sensitivity HgCdTe detector. The signal is processed by a high-sampling-rate oscilloscope.

Bottom: Power-versus-current curve of the QCL at fixed temperature. Two operating regimes are observed in this device, a single-mode regime and a comb regime.

cooled HgCdTe detector (BW = 0–10 MHz) is employed. A 12-bit vertical resolution, 1 GHz analog bandwidth, 2.5 GS/s sampling rate oscilloscope is used to acquire the signal and to compute its Fourier transform. The distance between the two mirrors (about 20 mm) is chosen in order to set the free spectral range (FSR) of the cavity close to f_s. In order to resolve the laser spectrum, a *Vernier ratio $Vr = f_s$/FSR* slightly different from one is chosen and a piezoelectric actuator is used to scan the cavity length over one FSR (see section 2.2.2 and appendix A.6). A schematic representation is depicted in fig. 2.19a and the obtained spectrum is shown in fig. 2.20.

To utilize the cavity as a frequency-to-amplitude converter, we act on the piezoelectric actuator and on the temperature controller of the laser to set $Vr = 1.0$ and to let the comb offset frequency f_o be equal to that of the optical cavity. In this way, the comb modes and the optical cavity resonances are perfectly matched (see fig. 2.19b for a schematic and fig. 2.19c for the measured cavity transmission profile). As a consequence, in these conditions and *only* in these conditions of temperature and driving current of the laser, all the comb modes are transmitted by the cavity. The cavity can thus be used as a *multimode* frequency-to-amplitude converter to collect the frequency fluctuations of all the modes at the same time (see section 2.2.1 as an example of application of this technique and appendix A.2 for a demonstration). Since $Vr = 1.0$, an accurate value of the optical cavity free spectral range (FSR) can be obtained by measuring f_s as described above. Such an accurate FSR value is needed for the calibration of the frequency-to-amplitude converter (see appendix A.1). The laser emits a power of $P = 25$ mW when the comb modes are exactly matched to the cavity resonances. Thanks to the high finesse of the cavity, it is also possible to collect the frequency fluctuations of an individual comb mode by slightly varying the FSR. A spectrum retrieved with the laser in single-mode operating conditions ($P = 15$ mW) has been also acquired. The FNPSD measured on the single-mode and comb regimes are reported in fig. 2.21. The spectra are compensated for the frequency-to-amplitude converter cutoff (see appendix A.1). We observe that the frequency noise on the comb regime lies slightly below the frequency noise on the single-mode regime. Moreover, the frequency noise of an individual comb mode is also equivalent to that acquired on all comb modes together. By integrating the FNPSD
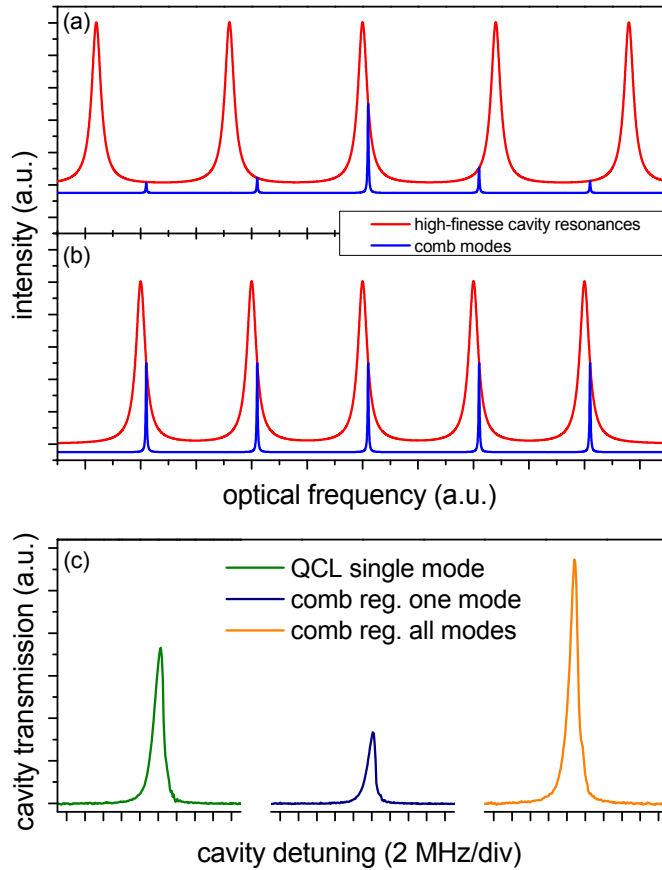
Figure 2.19: Schematic of the optical cavity and of the comb spectra with $Vr \neq 1.0$ (comb regime - one mode) and $Vr = 1.0$ (comb regime - all modes) (**a**) and **b**) respectively).

c) Cavity transmissions acquired in the three conditions: single-mode QCL, QCL in comb regime with only one mode in resonance with the cavity and QCL in comb regime with all the modes in resonance with the cavity. These acquisitions are obtained by scanning the cavity length. The cavity detuning is the variation of the resonance frequency (FSR) with the length. The comb is composed of many modes, but the most intense ones are six (see fig. 2.20). Essentially only these main modes contribute significantly to the orange transmission peak. On the other hand only the most intense mode (the one in resonance) contribute to the blue peak. These peaks are used for the calibration of the frequency-to-amplitude converter (see appendix A.1).
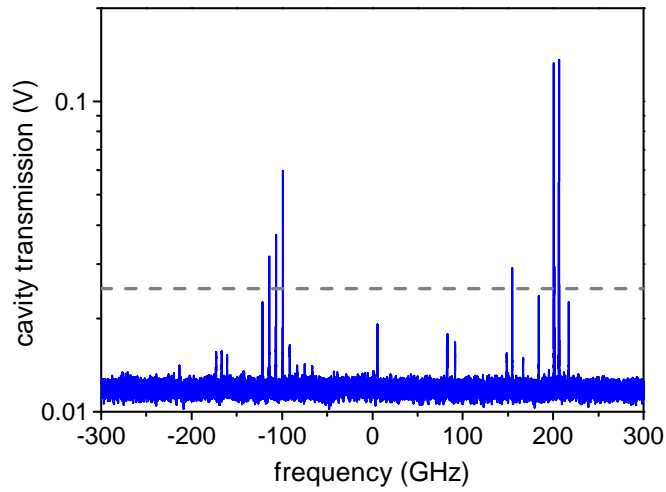
Figure 2.20: QCL-comb spectrum resolved by the cavity with a *Vernier ratio V r* slightly different from one. The cavity length is scanned over one FSR using a piezoelectric actuator. See fig. 2.19a for a schematic representation. The dashed gray line sets the relative detection noise floor level at a RF of 1 MHz (see fig. 2.21).
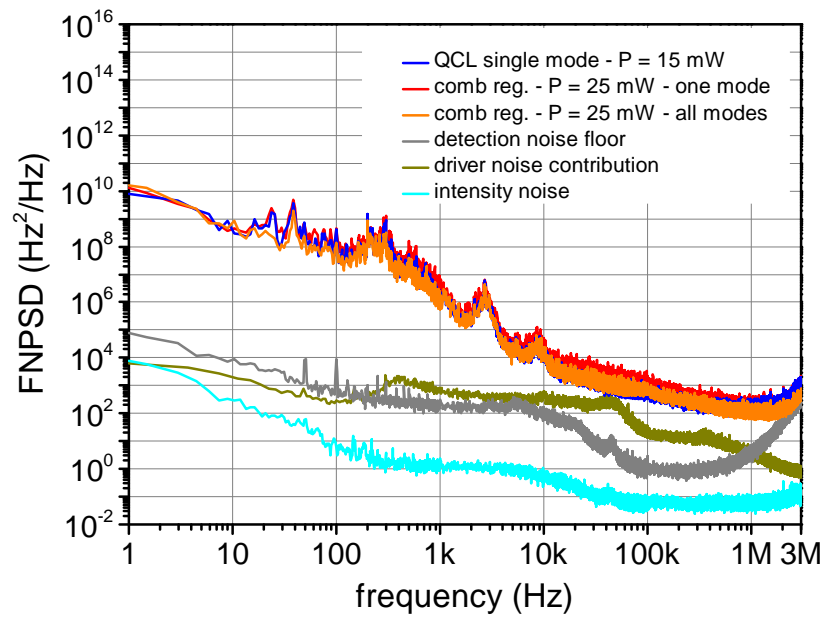
Figure 2.21: FNPSD of the QCL-comb taken in three different conditions. The spectra are compensated for the frequency-to-amplitude converter cutoff. The technical contributions to the noise are also reported: taking into account the detection noise floor shape, the spectra are reliable up to 2 MHz; the two contributions given one by the current driver and the other one related to the intensity noise are negligible.

using Elliott's formula (eq. 1.127), the FWHM of a laser mode can be retrieved. In this case a FWHM of about 600 kHz on a 1-s time scale is obtained. This value is consistent with the linewidth usually shown by DFB QCLs (see section 2.1.1 and references [68, 69] for a comparison). Moreover, the contributions of the current driver noise and the laser intensity noise as well as the detection noise floor are reported. Taking into account the detection noise floor shape, the spectra are reliable up to 2 MHz. Around 1 MHz, a *flattening* can be observed. Figure 2.22 shows a portion of the same FNPSD (from 100 kHz to 3 MHz). This flattening, characteristic of a white frequency noise, corresponds to the intrinsic quantum noise level $D_{\delta\nu}$ due to the spontaneous emission, the so-called *Schawlow-Townes* limit (see section 1.4.4).
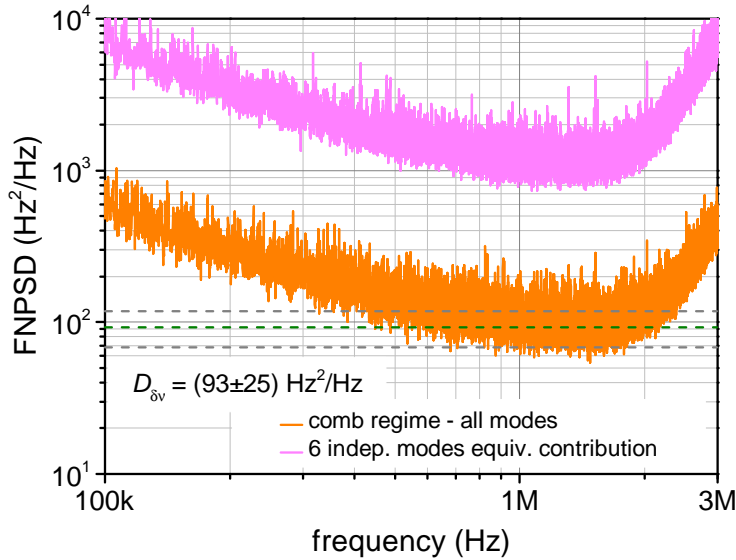
Figure 2.22: Zoom of the flattening portion of the spectrum related to the comb regime with all the modes transmitted around 1 MHz (see fig. 2.21), corresponding to the Schawlow-Townes limit ($D_{\delta\nu}$). The simulated FNPSD related to 6 independent modes is also shown.

Discussion

At this point it is interesting to compare this level $D_{\delta\nu}$ to the expected linewidth (HWHM) for single-mode lasers with the same characteristics,

given by the Schawlow-Townes formula (eq. 1.131)

$$\delta\nu = \frac{h\nu}{P}\frac{\alpha_{\text{tot}}c^2}{4\pi n_{\text{g}}^2}\alpha_{\text{m}}n_{\text{sp}}(1+\alpha_E^2)\qquad(2.15)$$

Taking $\nu = 42.2$ THz as center frequency, $P = 25$ mW as total power emitted by the laser, $\alpha_{\text{m}} = 2.2$ cm^{-1} as mirror losses, $\alpha_{\text{tot}} = 7.2$ cm^{-1} as total losses,[13] $n_{\text{g}} = 3.4$ as group refractive index, $n_{\text{sp}} = 2$ as spontaneous emission factor and $\langle\alpha_E^2\rangle = 0.0023$ as squared Henry linewidth enhancement factor averaged over the laser spectrum (see appendix A.3), we obtain $\delta\nu = 230$ Hz, value which is consistent with the one obtained from the spectrum $\delta\nu = \pi D_{\delta\nu} = (292 \pm 78)$ Hz (fig. 2.22). The fact that the measured Schawlow-Townes limit for the comb emission corresponds to the one computed using eq. 2.15 justifies the theoretical framework introduced with eqs. 2.11–2.14, since it confirms that in comb operation the laser behaves like a single-mode device, i.e. the modes are coherent.

Let's consider again the QCL-comb FNPSDs. The comparison between the two FNPSDs in comb regime shows that the quantum fluctuations of the different modes are correlated. In fact, we observe that the FNPSD – in particular the portion limited by the quantum noise – is identical when measured with one comb mode and with all comb modes simultaneously (see fig. 2.21). This quantum limit – a value which is given by the Schawlow-Townes expression – would be at least a factor of 6 *larger* than the measured one (see fig. 2.22), assuming that the quantum fluctuations of each comb mode are uncorrelated. This statement is justified by the fact that at a RF of 1 MHz at least 6 QCL-comb modes are expected to contribute to the spectrum (see fig. 2.20), because these modes are the ones within a factor of 0.2 respect to the most intense one, where the factor $(1/0.2)^2$ is the ratio between the FNPSD and the detection noise floor (see fig. 2.21). Such a factor of 6 is outside the uncertainty of the measurement.

This experiment proves that in QCL-combs the four-wave mixing process – at the origin of the comb operation – *correlates* the frequency fluctuations among the modes until the quantum limit. As a result, the linewidth is shown to be limited by the Schawlow-Townes formula, as it is for single-mode lasers of the same total power. Since QCL-combs

---

[13]The relatively high waveguide losses are due to the residual *cross-absorption* given by the multistack structure.

do not suffer from additional frequency noise, they are suitable for high-resolution spectroscopy applications.

2.2.4   Quantum-cascade-laser frequency comb stabilization

The experiment presented in the previous section proves the intrinsic coherence of the emission of a QCL-comb, but to be used for high-resolution spectroscopy applications a proper *stabilization* to overcome technical noise is required, as for single-frequency QCLs (see section 2.1). Indeed, for metrological purposes, a fine control of the main optical parameters is required [97] (see section 1.3.4). Moreover, this can be an additional occasion for studying the coherence properties of QCL-combs emission. In the following experiment, the DFG-comb presented in section 2.2.1 has been used to investigate the comb properties of the multimodal QCL emission, in a dual-comb-like setup [98]. This characterization is essential for metrological applications of such QCL-combs. Basically a QCL-comb tooth has been phase-locked to a DFG-comb one and the collective effect on the other QCL-comb teeth has been studied. The results are interpreted within the framework of frequency combs in terms of offset and spacing frequencies, relating these parameters and their fluctuations to primary physics quantities such as the QCL effective waveguide refractive index and the group refractive index.

Experimental setup

In fig. 2.23 the experimental setup is shown. The QCL-comb, provided by ETH Zürich, is a broad-gain Fabry-Pérot device, emitting continuous-wave radiation around 4.70 μm (of a previous generation respect to the laser presented in section 2.2.3). The spacing (f_s) between the longitudinal modes (QCL-comb teeth) is about 7 GHz. The laser working temperature is 16.5°C and the current is 735 mA, with an emitted power of 60 mW on a single transverse mode. In fig. 2.24 the laser spectrum measured with an FTIR spectrometer is shown. The DFG-comb[14] is essentially used to convert the MIR QCL-comb spectrum down to the radio frequencies (RF). It is important to remark here that the frequency noise of the DFG-comb (single tooth linewidth) is particularly low (2-kHz linewidth on a 1-s time scale). Moreover, the DFG-comb long term

---

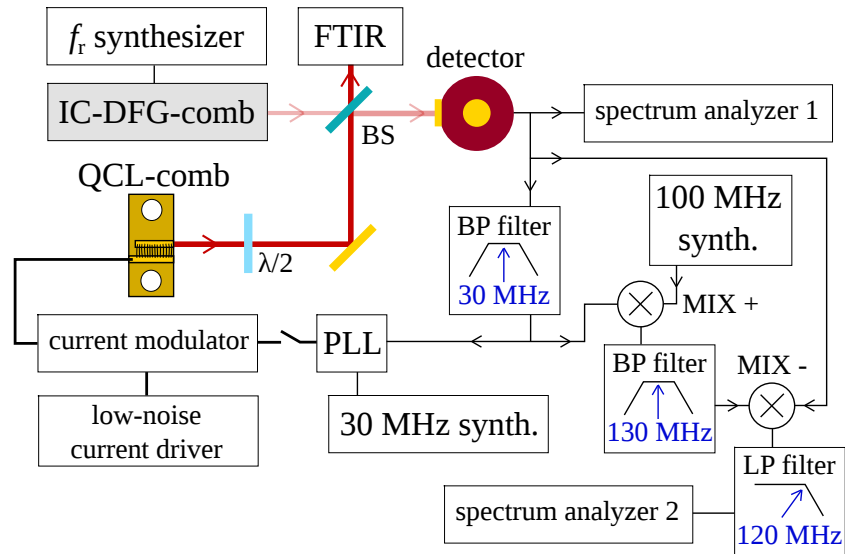[14] See section 2.2.1 for the details on its generation.

Figure 2.23: Experimental setup used for the beat-note detection. $\lambda/2$: half-wave plate to adjust the polarization; BS: asymmetric non-polarizing beam splitter (transmission 99%, reflection 1%); BP: RF band pass filter (in figure the center frequency is reported); LP: low pass filter; MIX: RF mixer; PLL: phase-locked-loop electronics. Each frequency synthesizer in the setup (including the ones in spectrum analyzers) is referenced to a quartz/Rb/GPS disciplined clock.
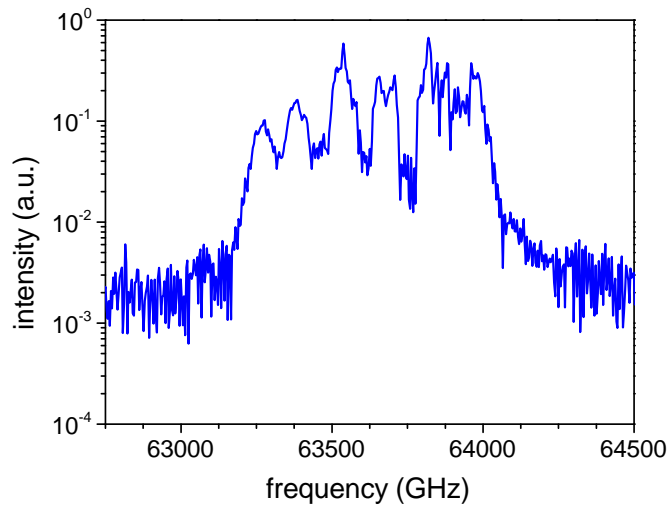

Figure 2.24: QCL-comb spectrum measured with an FTIR spectrometer. The resolution is 7 GHz, therefore the laser modes cannot be resolved. Considering that the spectrum is 700 GHz-wide, and the mode spacing is 7 GHz, an overall number of about 100 modes is deduced.

frequency stability and frequency accuracy descend directly from the ones of the metrological NIR-comb involved in the generation chain. The DFG-comb repetition rate (f_r) is 1 GHz and the spectrum is about 300-GHz wide.

As shown in fig. 2.23, the QCL-comb beam (about 1 mW of power) is superimposed to the DFG-comb beam (about 0.5 mW of power), sending them to a HgCdTe photodetector (200-MHz bandwidth). The recorded heterodyne beat-note signal (HBNS) is used for further analysis of the phase noise and frequency control of the QCL-comb. A fraction of the HBNS signal is recorded by an RF spectrum analyzer (spectrum analyzer 1). When the frequency spacing between the QCL-comb modes and the DFG-comb ones falls within the bandwidth of the detector, the obtained RF spectrum is made of several peaks, each of them resulting from the beating between a QCL-comb tooth and a DFG-comb tooth (in a ratio of one every seven). The spacing between these peaks is $|f_s - 7f_r|$ (about 10 MHz).[15]

The HBNS is also used in two RF chains. As represented on the left, the signal is filtered at 30 MHz just to select only one peak (with all the parameters chosen to have the better signal-to-noise ratio). Then it is sent to a home-made hybrid analog/digital phase-locked-loop (PLL) electronics. When the loop is closed on the QCL current modulator, this signal is locked to the 30 MHz local oscillator, essentially *locking* one QCL-comb tooth to a DFG-comb one.

On the right, the chain to remove the offset is depicted. The HBNS is filtered at 30 MHz to select only one peak, summed in an RF mixer to a 100 MHz signal and then subtracted in another mixer to the original HBNS. In this way, spectrum analyzer 2 shows the HBNS where one peak has been subtracted to all the others, therefore any common frequency contribution (offset) is canceled out.

Results

When the QCL-comb operates in free-running regime, the peaks in the HBNS (observed with spectrum analyzer 1) are about 1-MHz wide. As a first step, the performance of the loop has been tested. Once closed the

---

[15]This difference can be *positive* or *negative*, and in a HBNS both cases can occur at the same time. In this eventuality the RF peaks coming from a positive difference are named *direct*, the others are named *folded*.

loop and optimized the PLL parameters, the HBNS has been acquired with spectrum analyzer 1 in real-time mode. Each acquisition is made of 20 frames. Each frame contains the HBNS in time domain over a 2-ms time interval sampled at 75 MHz. Afterwards, for each frame the Fourier transform of the signal (amplitude and phase) has been computed. All the 20 obtained amplitude spectra of an acquisition are reported in fig. 2.25. In fig. 2.26 a zoom of the locked peak (the one filtered to be
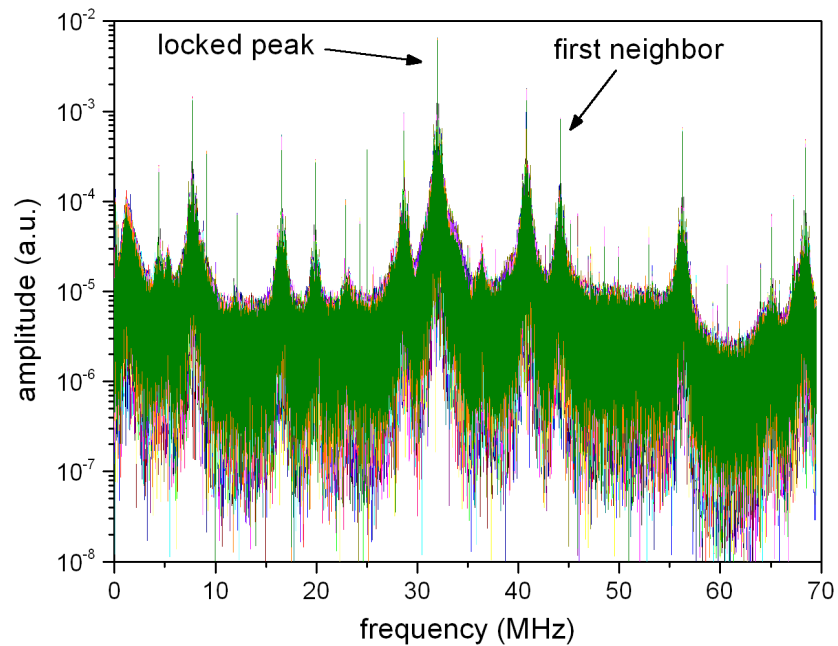

Figure 2.25: FFT amplitude of the 20 frames of an acquisition of the HBNS acquired using spectrum analyzer 1. Each color is related to a specific frame. The QCL-comb operates in locking condition. Each frame contains the HBNS in time domain over a 2-ms time interval sampled at 75 MHz.

used in the locking chain) is shown. On a frequency span of 2 MHz the typical shape of locked signals is evident, with the bumps given by the electronic bandwidths. On a span of 12 kHz the peak is still resolution-bandwidth-limited and a *perfect stability* over the whole acquisition is observed. In fig. 2.26 the phase of the signal around the locked peak is also reported. The phase is clearly stable over the whole acquisition. Now, for studying the collective effect of the locking, we concentrate our attention on the other peaks. In fig. 2.27 a zoom of the first-neighbor peak is shown. On a span of 2 MHz the peak shows a shape close to the one of the locked peak, but on a span of 12 kHz frequency fluctuations are evident. Nonetheless, they are strongly reduced compared to the
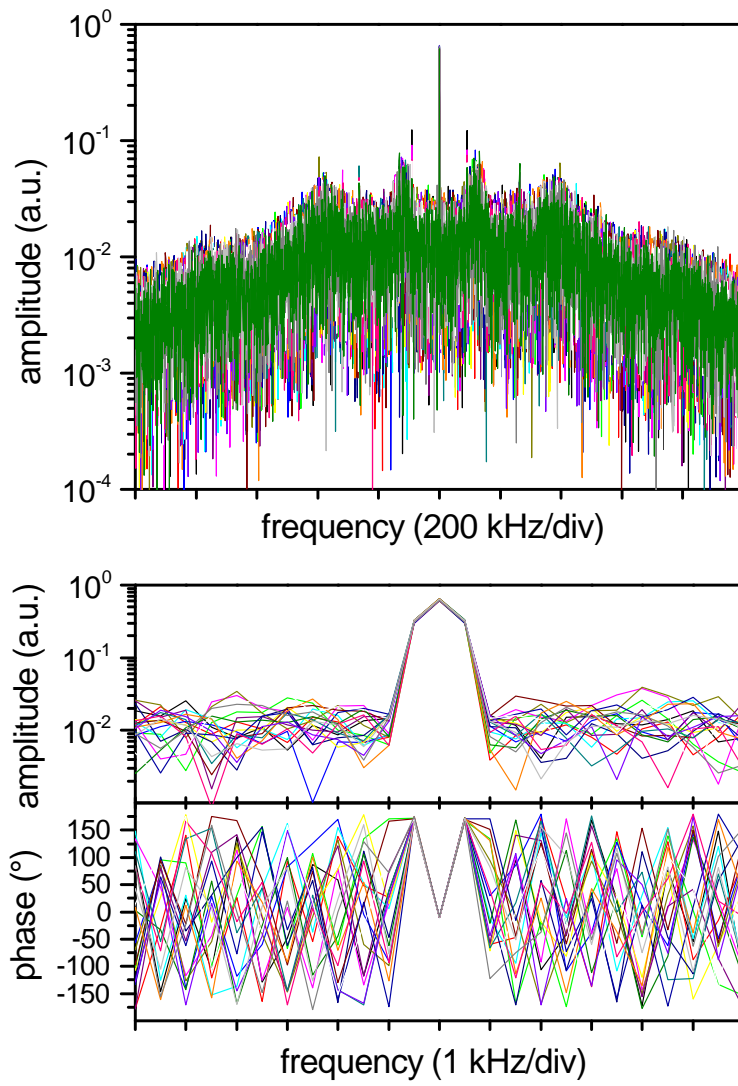
Figure 2.26: Zoom of the locked peak: amplitude (on two different spans) and phase (see fig. 2.25). Even on the narrower span a perfect stability both of the peak amplitude and phase can be observed.
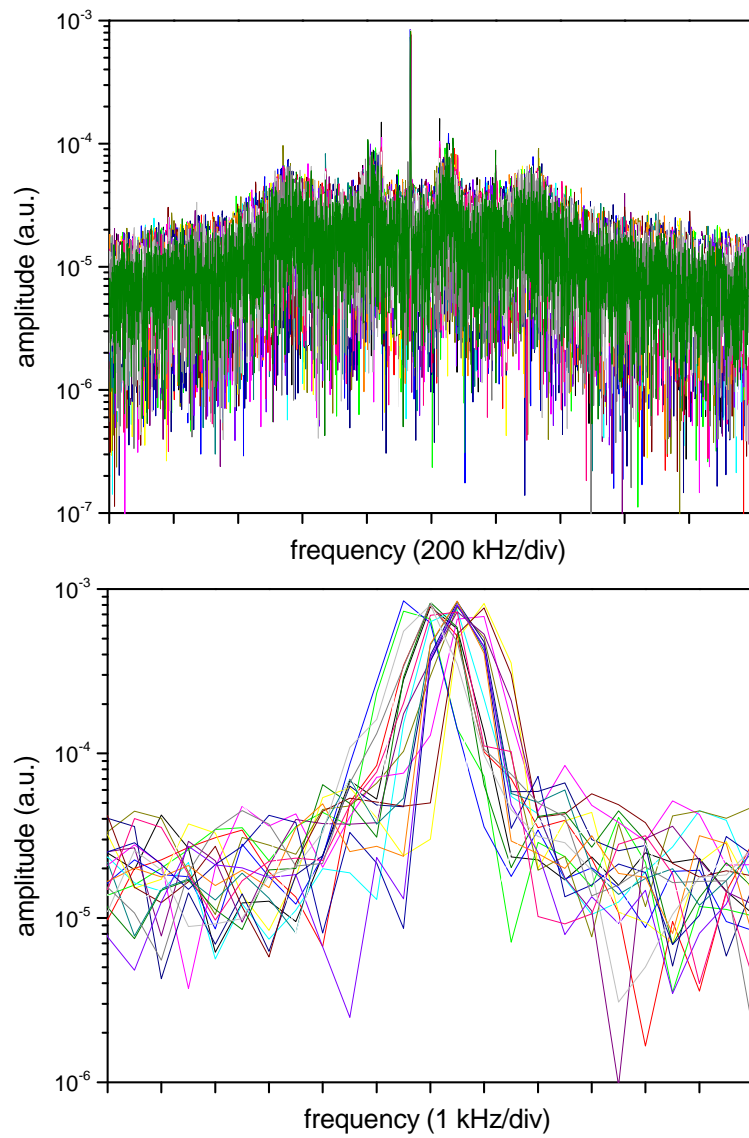
Figure 2.27: Zoom of the first-neighbor peak in locking operation (see fig. 2.25). On the narrower span the presence of frequency fluctuations is evident.

free-running regime, we can estimate a linewidth of few kHz against 500 kHz.

To be more quantitative, the 20 amplitude spectra have been *averaged*, yielding the spectrum shown in fig. 2.28. All the peaks have been fitted
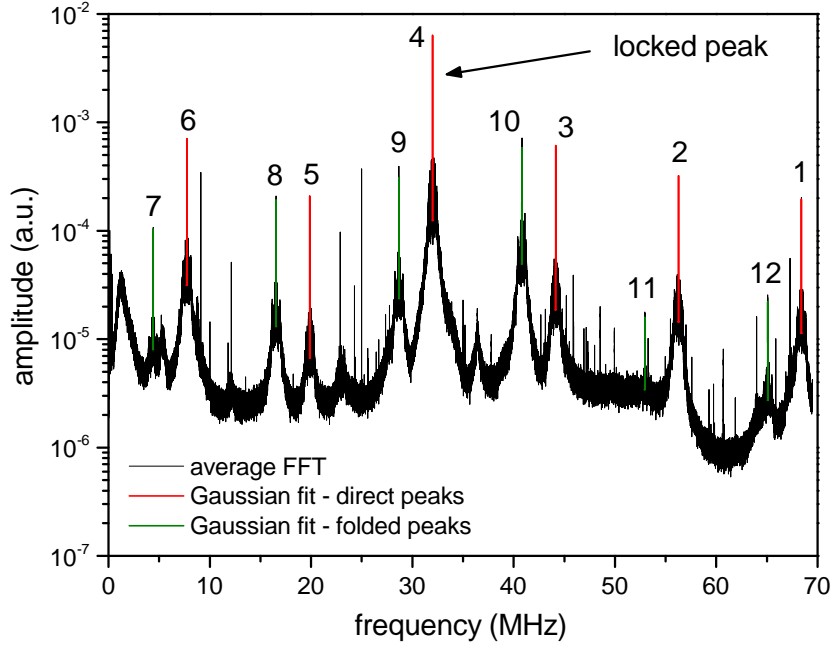
Figure 2.28: Average over the 20 amplitude spectra of an acquisition in locking operating regime (see fig. 2.25). Each peak has been fitted with a Gaussian function and labeled with an integer number m. For the direct peaks the relative QCL-comb mode has a higher frequency compared to the relative DFC-comb mode. For the folded peaks the opposite holds.

with a Gaussian function (see fig. 2.29 for an example). The obtained σ (Gaussian FWHM) have been plotted against the peak number and fitted with the following function:

$$\sigma(m) = \sqrt{\sigma_0^2(m - m_0)^2 + RBW^2} \qquad (2.16)$$

where m numbers the peaks in the HBNS, m_0 denotes the locked peak, and RBW is the instrumental resolution bandwidth. The use of this function comes from the assumption that both the shape of the instrumental function and the distribution of the frequency fluctuations are Gaussian, and it is justified by the fact that the function fits well the acquired data. σ_0 represents the mean square root value of the frequency fluctuation of the spacing between the laser modes (Δf_s). Repeating this procedure with few different acquisitions (sets of 20 frames) and averaging over the
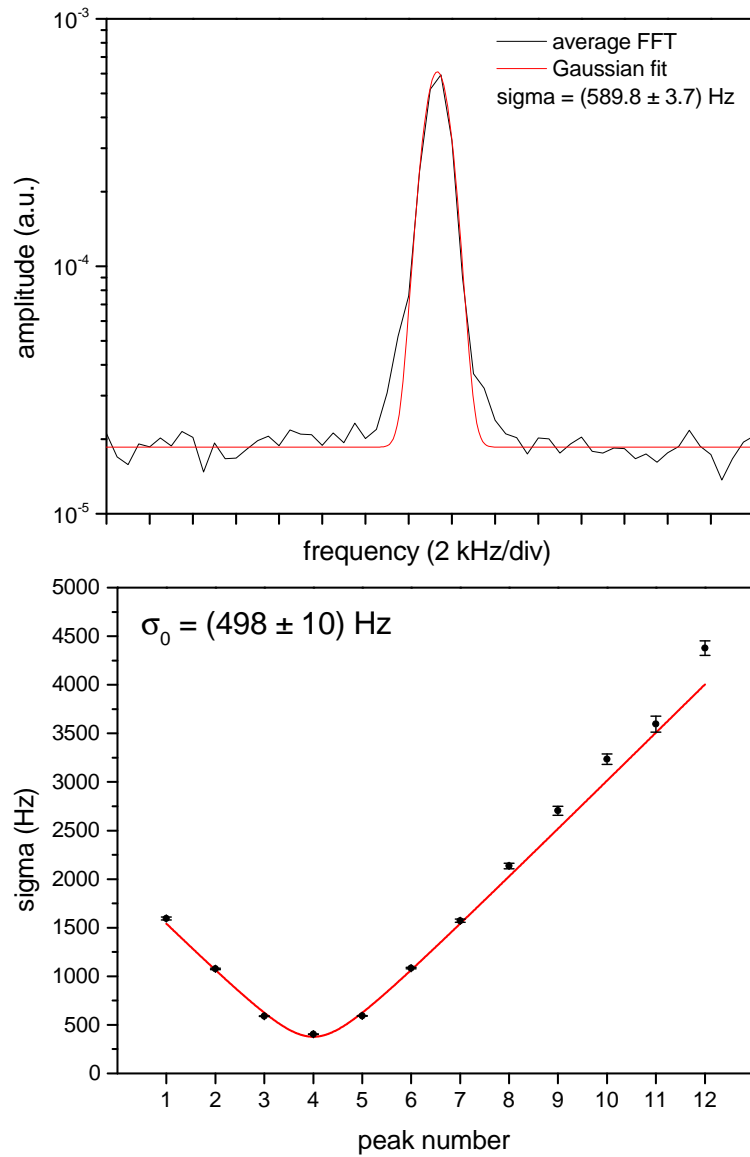
Figure 2.29: **Top:** zoom of the first-neighbor averaged peak (number 3 in fig. 2.28) fitted with a Gaussian function.
Bottom: fit of the peaks widths in locking operating regime using eq. 2.16.

obtained values, yields

$$\bar{\sigma}_{0 \text{ lock}} = (450 \pm 40) \text{ Hz} \qquad (2.17)$$

Since the QCL-comb modes are 100, and considering that we phase-lock the central one (or one nearby), the accumulated residual frequency noise on the modes on the sides of the spectrum is

$$(450 \times 50) \text{ Hz} \simeq 22 \text{ kHz} \qquad (2.18)$$

Since the linewidth of the DFG-comb (the reference) is $\Delta\nu_{\text{DFG}} = (750 \pm 200)$ Hz (on a 20 ms time scale) [83], we can state that the overall single QCL-comb mode linewidth is reduced from 500 kHz to values ranging from 1 to 23 kHz on a 40 ms time scale.

Afterwards, in order to study the dynamics of the laser in free-running operation, the locking chain has been opened, and the HBNS has been acquired downstream the chain removing the offset fluctuations. Again each acquisition is made of 20 frames and each frame contains the HBNS in time domain over a 2-ms time interval sampled at 75 MHz. The 20 amplitude spectra have been averaged, giving the spectrum shown in fig. 2.30. All the peaks have been fitted with a Gaussian function (see fig. 2.31 for an example). The obtained σ have been plotted against the peak number and fitted again with eq. 2.16. The value obtained averaging over few different acquisitions is

$$\bar{\sigma}_{0 \text{ free run.}} = (343 \pm 12) \text{ Hz} \qquad (2.19)$$

In order to interpret these results in terms of the two main optical quantities characterizing the laser waveguide, the effective and the group refractive index (n_c and n_g, respectively) a specific discussion is needed (see appendix A.4). The frequencies of a reference mode (whose frequency and order are ν_c and N, respectively) and of its first neighbor are expressed in terms of the effective and the group refractive index. Subsequently, the OFC offset (f_o) and spacing (f_s) parameters and their fluctuations are derived. The obtained relations for the fluctuations are
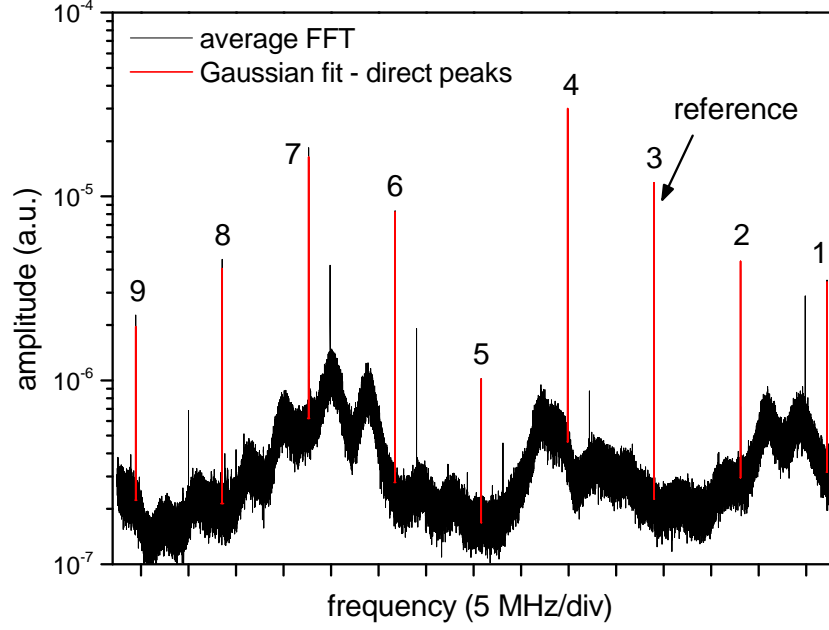
Figure 2.30: Average over the 20 amplitude spectra of an acquisition in free-running operating regime with the offset canceled, acquired using spectrum analyzer 2. The reference peak used for the offset subtraction has been pointed out. Each peak has been fitted with a Gaussian function and labeled with an integer number m. The offset cancellation works for direct peaks.

	free running	locked
Δf_s	(343 ± 12) Hz	(450 ± 40) Hz
$\Delta \nu_c$	(500 ± 50) kHz	(750 ± 200) Hz

Table 2.2: Measured widths (frequency fluctuations) in free-running and locked operation. The reported values are referred to a 40 ms time scale.

(see eqs. A.41 and A.42)

$$\frac{\Delta n_c}{n_c} = -\Delta \nu_c \frac{1}{N} \frac{2n_c L}{c} \qquad (2.20a)$$

$$\frac{\Delta n_g}{n_g} = -\Delta f_s \frac{2n_g L}{c} \qquad (2.20b)$$

where $L = (6.40 \pm 0.05)$ mm is the physical length of the waveguide, $n_c = (3.175 \pm 0.005)$, $n_g = (3.320 \pm 0.025)$, and $N = 9030$ (computed as the ratio between the optical frequency and the spacing f_s).

In table 2.2 the measured values are collected (refer to eqs. 2.17 and 2.19). All the reported values are referred to a 40 ms time scale. In
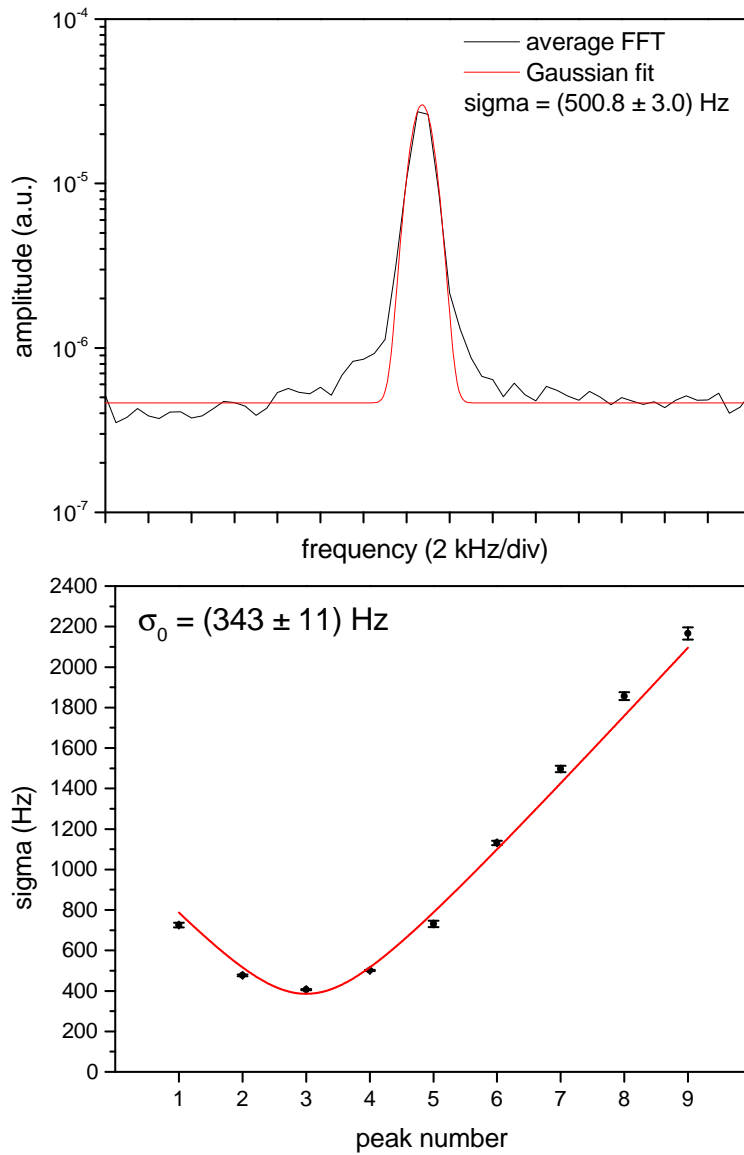
Figure 2.31: **Top:** zoom of the first-neighbor averaged peak (number 4 in fig. 2.30) fitted with a Gaussian function.
Bottom: fit of the peaks widths in free-running operating regime using eq. 2.16.

order to understand the *impact* of the locking on the laser parameters, the ratios between the values in locking conditions and in free-running conditions are computed, yielding

$$\frac{\Delta n_c}{n_c}\bigg|_{\text{lock}} = 0.0015 \cdot \frac{\Delta n_c}{n_c}\bigg|_{\text{free}} \qquad (2.21\text{a})$$

$$\frac{\Delta n_g}{n_g}\bigg|_{\text{lock}} = 1.3 \cdot \frac{\Delta n_g}{n_g}\bigg|_{\text{free}} \qquad (2.21\text{b})$$

 The ratios given in eq. 2.21 clearly show that the loop acts essentially on the *effective refractive index n_c* reducing its fluctuations in order to stabilize the emission (satisfying eq. A.35). On the other hand $\Delta n_g/n_g$ is almost unaffected. This means that the contribution given by the term related to Δn_c to Δn_g is negligible compared to the one related to the dispersion $\mathrm{d}n/\mathrm{d}\nu$ (see eq. A.34).

   This experiment proves that the QCL-comb mode used in the locking chain is perfectly stabilized, while the other modes are only partially stabilized. The locked QCL-comb mode shows a perfectly stable phase difference compared to the DFG-comb one, while the other QCL-comb modes show a *reduced linewidth* from 500 kHz down to values ranging from 1 to 23 kHz on a 40 ms time scale, depending on the distance from the locked mode. Another actuator to control the spacing fluctuations is required in order to lock all the modes. Apparently, the spacing fluctuations are not affected by the locking.

Conclusion

To conclude, a *summary* of the main results reported in this thesis and some perspectives are here given.

The main theme of this work is the development of *coherent laser sources* for *high-resolution molecular spectroscopy* in the MIR.

- The first reported experiment (see section 2.1.1 and ref. [67]) consists in frequency referencing a single-frequency QCL to a CO_2 absorption line detected by polarization spectroscopy. Starting from a free-running linewidth of about 500 kHz for the QCL, a 760 Hz linewidth (on a 1 ms time scale) is obtained thanks to the locking, and the QCL absolute frequency is stabilized to the center of the CO_2 line at a precision level of 4×10^{-11} on 1 s. The absolute frequency of the locked QCL is measured with an accuracy of 4×10^{-10}.

- The second one (see section 2.1.2 and ref. [73]) consists in phase-locking the same laser to a metrological non-linear-generated radiation. The 250-kHz bandwidth with a residual RMS phase-noise of 0.56 rad leads to a subkilohertz-linewidth QCL radiation. The QCL frequency stability is 6×10^{-13} on 1 s with an absolute traceability accuracy of 2×10^{-12}, both limited by the reference OFC.

- The third one (see section 2.1.3 and ref. [77]) is a proof of the performances of the phase-locked QCL as spectroscopy source. Several CO_2 absorption lines have been measured by saturation spectroscopy. The reported measurements are 3–4 orders of magnitude more precise than the values extracted from the HITRAN

117

database [6] and thus could be used to improve the molecular parameters of the involved ro-vibrational band. The 1–4 kHz precision achieved by the presented measurements is limited by both the Lamb-dip width and the S/N, but neither by the spectral linewidth nor the accuracy of the QCL absolute frequency.

- With the fourth experiment (see section 2.2.1 and ref. [83]) a change of perspective is reached, moving from single-frequency spectroscopy to *multi-frequency spectroscopy*. It consists indeed in the intracavity generation of a MIR OFC through non-linear difference-frequency generation (DFG-comb). The proposed technique ensures an appreciable amount of power (0.5 mW), together with a remarkably high stability. The tooth linewidth is indeed 2.0 kHz and 750 Hz on a time scale of 1 s and 20 ms, respectively. An average power of 1 μW for each single tooth is achieved, which means a remarkably high value for the per-tooth power spectral density (0.5 μW/kHz on a 1-s time scale). The generated spectrum spans 27 nm, with a center wavelength tunable from 4.2 to 5.0 μm.

- The fifth one (see section 2.2.2 and ref. [86]) is a test of the performances of the DFG-comb as reference for single-frequency QCLs and as source for direct comb spectroscopy. Using a high-finesse optical cavity as spectrometer to resolve the comb spectrum, the absorption of CO_2 around 4.3 μm has been studied.

- The sixth experiment (see section 2.2.3 and ref. [92]) deals with a new-generation QCL-comb. The aim of the experiment is to characterize its frequency noise till the Schawlow-Townes limit using a high-finesse optical cavity as multimode frequency-to-amplitude converter, in order to test the effective coherence among the modes. Since the measured frequency noise spectrum for all the modes shows the same values compared to the one given by a single mode, the coherence is proven down to the quantum limit.

- In the seventh and last-presented experiment (see section 2.2.4 and ref. [98]) a QCL-comb has been phase-locked through a single chain to the DFG-comb mentioned in section 2.2.1. The QCL-comb modes show a reduced linewidth from 500 kHz down to values ranging from 1 to 23 kHz on a 40 ms time scale, but for controlling the spacing fluctuations an additional actuator is required.

The experimental *perspectives* are twofold. First, the capabilities of the DFG-comb have to be exploited in a more efficient manner filling the high-finesse cavity with the sample gas, in order to detect sample gases with lower concentration than ambient CO_2 and/or weaker absorption lines. Moreover, *new-generation non-linear crystals*, realized with a holographic technique [99, 100], are planned to be used to ensure a wider comb spectral coverage (up to a factor of ten).

On the side of QCL-combs, the experiments proved the intrinsic coherence of the emitted radiation, but as for metrological NIR-combs a proper *full stabilization* is needed for metrological and high-resolution spectroscopy applications. Several approaches will be tried, each of them aimed to the fine control and the absolute frequency referencing of the emission.

$\big[$ Appendix

A.1 Frequency-to-amplitude converter calibration

In order to measure frequency fluctuations of an optical signal, a proper *frequency-to-amplitude converter* is required. This happens because standard detectors (such as photodiodes) are sensitive to power (amplitude/intensity) fluctuations, but they are almost insensitive to frequency fluctuations.[16] In this section, the procedure for the *calibration* of an optical frequency-to-amplitude converter is discussed. This procedure has already been applied giving reliable results, as ascertained by comparing the results obtained by using different types of frequency-to-amplitude converters, such as optical cavities resonances and molecular absorption lines (see section 2.1.2 for an example of comparison). The obtained frequency noise power spectral densities (FNPSDs) are reliable up to the limit given by the detection noise floor set by the detection system. The setup is mainly composed of the laser source under test, an optical cavity with a mirror connected to a piezoelectric actuator, a detector, an oscilloscope and a spectrum analyzer (see fig. 2.18). The laser current and temperature must stay constant in order to keep the optical frequency constant. In order to calibrate the frequency-to-amplitude converter, two ingredients are needed:

- The *cavity transmission profile*, obtained by scanning the cavity length acting with a voltage ramp on the piezoelectric actuator.

---

[16]An important role in determining this limitation is played by the fact that the carrier frequency is orders of magnitude larger than its deviations (tens–hundreds of terahertz versus megahertz).

The cavity is usually scanned over few FSRs (typically three) in order to avoid non-linearities. The cavity transmission profile is acquired with a detector and the photo-voltage is sampled with an oscilloscope, triggered by the voltage ramp controlling the piezoelectric actuator.

- The *photo-current voltage noise power spectral density* (VNPSD) of the light transmitted by the cavity, collected with the same detector and acquired with a spectrum analyzer. The VNPSD contains the FNPSD if the cavity length is adjusted in order to have the optical frequency of the laser source corresponding to the side of a cavity resonance, where the transmission is half the maximum. The VNPSD unities are V^2/Hz because VNPSD are voltage fluctuations square mean values normalized to the detection RF bandwidth.

The frequency scale of the cavity transmission profile is obtained observing adjacent resonance peaks which fall at a specific Δt that corresponds to the cavity FSR. After this conversion, the profile of the cavity transmission is expressed in terms of V/Hz. At this point we focus on the resonance peak closer to the center of the transmission profile, we measure its FWHM and we determine the slope of the sides fitting the profile around the half maximum with a beeline. This slope is expressed in V/Hz. As a frequency-to-amplitude converter, the cavity behaves as a second-order *low-pass filter*. The cutting is due to the photon lifetime within the cavity. The cutoff frequency is given by $f_c = $ FWHM/2 and the compensating factor for this cutoff is $(1 + (f/f_c)^2)$. At the end, the following formula is obtained:

$$\text{FNPSD (Hz}^2\text{/Hz)} = \text{VNPSD (V}^2\text{/Hz)} \left[\frac{1 + (f/f_c)^2}{\text{slope(V/Hz)}} \right]^2 \qquad \text{(A.1)}$$

The detection noise floor is acquired and elaborated exactly in the same way, just with the laser beam blocked before reaching the cavity.

As already stated, frequency fluctuations are converted into intensity fluctuations, but also the *original* intensity fluctuations of the laser source are detected. In order to have a reliable FNPSD spectrum, it is crucial to check that these original intensity fluctuations are *negligible* compared to the ones given by the conversion. To this purpose, the intensity noise

(amplitude noise) of the laser has to be measured. For this measurement the cavity is removed and the laser beam is shined onto the detector, just properly attenuated to take advantage of the whole detection dynamical range. In order to compare the intensity noise with the frequency noise a proper conversion is needed. The intensity noise has to be scaled to the level of the cavity transmission. This is done by dividing the intensity noise by the signal DC value and multiplying it for the peak value of the cavity resonance (*RP*). Finally it is multiplied for the same slope. The contribution of the intensity noise to the frequency noise is therefore given by

$$
\text{FNPSD}_{\text{intensity}}(\text{Hz}^2/\text{Hz}) = \text{VNPSD}_{\text{intensity}}(\text{V}^2/\text{Hz})\cdot
$$
$$
\cdot \left(\frac{RP(\text{V})}{\text{DC}_{\text{intensity}}(\text{V})}\right)^2 \left(\frac{1}{\text{slope}(\text{V}/\text{Hz})}\right)^2 \tag{A.2}
$$

A.2 Multimode frequency-to-amplitude conversion

In this section it will be shown how, by satisfying the right conditions, it is possible to use an optical cavity as *multimode frequency-to-amplitude converter* to retrieve the frequency noise of a frequency comb (see fig. 2.19b). The intensity of the i-th comb mode transmitted by the optical cavity is given by

$$
I_i = I_{i0}T(\nu_{ij}) \tag{A.3}
$$

where I_{i0} is the intensity of the i-th comb mode, $\nu_{ij} = \nu_j - \nu_i$, ν_i is the center frequency of the i-th comb mode, ν_j is the center frequency of the j-th cavity resonance and $T(\nu_{ij})$ is the convolution between the i-th comb mode shape and the j-th cavity resonance profile.[17] The total intensity transmitted by the cavity is given by

$$
I_{\text{tot}} = \sum_i I_i = \sum_i [I_{i0}T(\nu_{ij})] \tag{A.4}
$$

If

$$
\nu_{ij} = \Delta\nu = \text{const.} \qquad \forall i, j \tag{A.5}
$$

---

[17] $T(\nu_{ij})$ is non-vanishing only if $|\nu_{ij}| < \text{FSR}$.

we are allowed to bring $T(\nu)$ out of the sum, yielding

$$I_{\text{tot}} = T(\Delta\nu)\sum_i I_{i0} = T(\Delta\nu)I_{0\text{ tot}} \tag{A.6}$$

This proves that in these conditions the transmission and consequently the frequency-to-amplitude conversion follows the same rules of the single-mode case.

Actually, the condition expressed by eq. A.5, where both the comb modes and the cavity resonances have the same dispersion in frequency, is not so strict. It is in fact sufficient that

$$|\nu_{ij} - \nu_{lm}| \ll \frac{1}{2}\text{FWHM}\left[T(\Delta\nu)\right] \tag{A.7}$$

for all the transmitted modes. In other words it is sufficient that the accumulated dispersion over the whole comb spectrum is small compared to the width of the cavity resonances.

A.3 Henry linewidth enhancement factor estimation

In this section it will be shown how to compute the Henry linewidth enhancement factor (see section 1.4.4) for a QCL-comb. For the derivation, a *Lorentzian lineshape* for the intersubband transition can be assumed [58]. The factor can therefore be expressed as

$$\alpha_E(\nu) = \frac{\nu_{32} - \nu}{\gamma_{32}} \tag{A.8}$$

where ν_{32} and γ_{32} are the center frequency and the HWHM of the transition, respectively, while ν is the frequency of the radiation emitted by the laser. Concerning ν, we have to consider that the emitted radiation is a *comb of frequencies*, therefore α_E has to be computed as *average* over the whole emitted spectrum

$$\langle\alpha_E^2\rangle_{\text{laser spectrum}} = \frac{1}{\Delta\nu\,\gamma_{32}^2}\int_{\text{las. sp.}}(\nu_{32}-\nu')^2\,d\nu' \tag{A.9}$$

where $\Delta\nu$ is the width of the comb spectrum. Assuming that the center of the emitted spectrum corresponds to ν_{32} we obtain directly

$$\langle \alpha_E^2 \rangle_{\text{laser spectrum}} = \frac{1}{3\gamma_{32}^2} \left(\frac{\Delta\nu}{2} \right)^2 \tag{A.10}$$

For the QCL-comb used in the experiment presented in section 2.2.3 we know from electroluninescence measurements that $\gamma_{32} = 150 \text{ cm}^{-1}$. Moreover, in the actual operating conditions of the laser ($P = 25 \text{ mW}$) the spectrum width is $\Delta\nu = 25 \text{ cm}^{-1}$. The obtained Henry factor is then

$$\langle \alpha_e^2 \rangle_{\text{laser spectrum}} = 0.0023 \tag{A.11}$$

value that can be *neglected* in eq. 2.15.[18]

A.4 OFC parameters derivation

In this section, a discussion on how to *relate* the two main optical parameters of a frequency comb (spacing and offset frequencies) to the effective refractive index and the group refractive index of a QCL-comb waveguide is presented.
We start considering two teeth of the QCL-comb, the reference one and its first neighbor. Their frequencies are respectively given by

$$\nu_c = N \frac{c}{2n(\nu_c)L} \tag{A.12a}$$

$$\nu_1 = (N+1) \frac{c}{2n(\nu_1)L} \tag{A.12b}$$

where N is an integer giving the order of the tooth chosen as reference, $n(\nu_i)$ is the effective refractive index, and L is the QCL-comb cavity length. In comb formalism, the frequencies of these two teeth are expressed in terms of offset frequency f_o and spacing f_s as follows:

$$\nu_c = N f_s + f_o \tag{A.13a}$$

$$\nu_1 = (N+1) f_s + f_o \tag{A.13b}$$

---

[18]In case of a multistack device the shape of the gain curve on the top is even flatter than a Lorentzian, consequently the given value for $\langle \alpha_E^2 \rangle$ has to be considered as an upper limit.

Inverting the two formulas we easily obtain

$$f_s = \nu_1 - \nu_c \tag{A.14a}$$

$$f_o = \nu_c(N+1) - \nu_1 N \tag{A.14b}$$

Now we compute the spacing:

$$f_s = (N+1)\,\frac{c}{2n(\nu_1)L} - N\,\frac{c}{2n(\nu_c)L} \tag{A.15}$$

We then expand the refractive index and introduce the group refractive index as follows

$$n(\nu_1) = n(\nu_c) + f_s\,\left.\frac{dn}{d\nu}\right|_{\nu_c} \tag{A.16}$$

$$n_g = n(\nu_c) + \nu_c\,\left.\frac{dn}{d\nu}\right|_{\nu_c} \tag{A.17}$$

$$\left.\frac{dn}{d\nu}\right|_{\nu_c} = \frac{1}{\nu_c}[n_g - n(\nu_c)] \tag{A.18}$$

obtaining

$$n(\nu_1) = n(\nu_c) + \frac{f_s}{\nu_c}[n_g - n(\nu_c)] \tag{A.19}$$

Henceforth $n(\nu_c) = n_c$. Now, using eqs. A.13 and A.19, and the expansion

$$1/(1+x) \simeq 1 - x \tag{A.20}$$

for $x \ll 1$, and noting that

$$\frac{f_s}{\nu_c}[n_g - n_c] \ll n_c \tag{A.21}$$

we can continue computing the spacing (eq. A.15)

$$\begin{aligned}
f_s &\simeq (N+1)\frac{c}{2n_cL}\left[1 - \frac{f_s}{n_c}\frac{2n_cL}{c}\frac{1}{N}(n_g - n_c)\right] - N\frac{c}{2n_cL}\\
&= \frac{c}{2n_cL} - \frac{(N+1)}{N}\frac{f_s}{n_c}(n_g - n_c)
\end{aligned} \tag{A.22}$$

Factorizing f_s as

$$f_s\left[1 + \frac{(N+1)}{N}\frac{(n_g - n_c)}{n_c}\right] = \frac{c}{2n_cL} \tag{A.23}$$

and using again eq. A.20 we obtain

$$f_s \simeq \frac{c}{2 n_g L} \left[1 + \frac{1}{N} \frac{(n_c - n_g)}{n_g} \right] \qquad \text{(A.24)}$$

Now we evaluate the offset frequency:

$$f_o = N(N+1) \frac{c}{2n(\nu_c)L} - N(N+1) \frac{c}{2n(\nu_1)L} \qquad \text{(A.25)}$$

Using again eq. A.19 and neglecting terms in $(n_g - n_c)^2$ we obtain

$$f_o \simeq f_s(N+1) \frac{(n_g - n_c)}{n_c} \qquad \text{(A.26)}$$

Using eq. A.24 at the zeroth order we obtain

$$f_o \simeq (N+1) \frac{c}{2L} \left(\frac{1}{n_c} - \frac{1}{n_g} \right) \qquad \text{(A.27)}$$

In order to check eq. A.27 with the formalism developed for *pulsed combs*, we can compare it to equation 1 in ref. [101]. The latter, written for the group phase offset, reads as follows:

$$\Delta \varphi_{GPO} = \frac{2\pi \nu_c^2}{c} \int_0^L \frac{\mathrm{d} n(z)}{\mathrm{d}\nu} \mathrm{d}z \qquad \text{(A.28)}$$

The sub-cycle part of $\Delta\varphi_{GPO}$ is $\Delta\varphi_{CEO}$, the carrier envelope offset, defined mod 2π. The offset frequency is defined as

$$f_o = \frac{\Delta\varphi_{CEO}}{2\pi} f_s = \nu_c^2 \frac{f_s}{c} \int_0^L \frac{\mathrm{d} n(z)}{\mathrm{d}\nu} \mathrm{d}z \qquad \text{(A.29)}$$

In our case the refractive index is homogeneous along the laser cavity, therefore the integral yields just a factor $2L$. Finally, recalling eqs. A.12 and A.18 we obtain

$$f_o = f_s N \frac{(n_g - n_c)}{n_c} \qquad \text{(A.30)}$$

This result is very *close* to that of eq. A.26 since $N \gg 1$.

In eq. A.24 every parameter is usually well known, therefore it can be used to *compute* the group refractive index. For the moment we neglect the second term in parenthesis, obtaining

$$n_g \simeq \frac{c}{2L f_s} \qquad \text{(A.31)}$$

For the QCL-comb presented in section 2.2.4 we have $L = (6.40 \pm 0.05)$ mm and $f_s = 7.062$ GHz (measured by using the metrological DFG-comb), obtaining

$$n_g = (3.320 \pm 0.025) \tag{A.32}$$

Knowing that the average refractive index seen by the laser mode within the guide is $n(\nu_c) = (3.175 \pm 0.005)$ and knowing that $N = 9030$ (computed as the ratio between the optical frequency and the spacing f_s), considering again eq. A.24 it can be easily verified that the second term in parenthesis is negligible. Henceforth we will neglect it whenever convenient.

Recalling eq. A.13, the optical parameters *fluctuations* can be evaluated:

$$\Delta\nu_c = N\Delta f_s + \Delta f_o \tag{A.33a}$$
$$\Delta\nu_1 = (N+1)\Delta f_s + \Delta f_o \tag{A.33b}$$

Moreover, from eq. A.17 and using eq. A.33 the group-refractive-index fluctuations can be computed:

$$\begin{aligned}
\Delta n_g &= \Delta n_c + \Delta\nu_c \frac{\mathrm{d}n}{\mathrm{d}\nu} + \nu_c \, \Delta\left(\frac{\mathrm{d}n}{\mathrm{d}\nu}\right) \\
&= \Delta n_c \left(1 - N\frac{c}{2n_c L}\frac{1}{n_c}\frac{\mathrm{d}n}{\mathrm{d}\nu}\right) + \nu_c \, \Delta\left(\frac{\mathrm{d}n}{\mathrm{d}\nu}\right)
\end{aligned} \tag{A.34}$$

Assuming that the Nth QCL-comb tooth is phase-locked to a DFG-comb tooth (see section 2.2.4), within the bandwidth of the loop we can state that

$$\Delta\nu_c = \Delta\nu_{\text{DFG}} \tag{A.35}$$

yielding

$$\Delta\nu_1 = \Delta f_s + \Delta\nu_{\text{DFG}} \tag{A.36}$$

In QCLs the two main phenomena that give the tunability of the emitted frequency are the variation of the refractive index and the variation of the physical length of the laser cavity with *temperature*, but the first contribution is one order of magnitude larger (see ref. [58] page 178). The other temperature-dependent parameter is the group refractive index. From eq. A.17 it is clear that n_g is not independent from n_c. Nonetheless

n_g contains the term $\mathrm{d}n/\mathrm{d}\nu$ which can depend on temperature in a different way compared to n_c. For this reason we compute

$$\Delta f_x = \frac{\mathrm{d}f_x}{\mathrm{d}n_c}\Delta n_c + \frac{\mathrm{d}f_x}{\mathrm{d}n_g}\Delta n_g \qquad (x = s, o) \qquad (A.37)$$

In particular, using eq. A.24 (at the zeroth order) and eq. A.27, they read as follows:

$$\Delta f_s = -\frac{\Delta n_g}{n_g}\frac{c}{2n_g L} \qquad (A.38)$$

$$\Delta f_o = -(N+1)\frac{c}{2L}\left(\frac{\Delta n_c}{n_c^2} - \frac{\Delta n_g}{n_g^2}\right) \qquad (A.39)$$

Moreover, using again eq. A.12 we have

$$\Delta \nu_c = -\frac{\Delta n_c}{n_c}N\frac{c}{2n_c L} \qquad (A.40)$$

yielding

$$\frac{\Delta n_c}{n_c} = -\Delta \nu_c \frac{1}{N}\frac{2n_c L}{c} \qquad (A.41)$$

and from eq. A.38 we have

$$\frac{\Delta n_g}{n_g} = -\Delta f_s \frac{2n_g L}{c} \qquad (A.42)$$

where the *fluctuations* of the effective and the group refractive index are obtained.

A.5   QCL frequency modulation bandwidth

An important characteristic for a laser is its frequency modulation bandwidth. The setup used for this measurement is the same used for the measurement of the FNPSD (see appendix A.1). In this case a frequency modulation is induced by modulating the driving current. The frequency of the modulation is varied and the laser *frequency deviation* is measured. In fig. A.1 the frequency modulation bandwidth of the QCL used for the experiments reported in section 2.1 is shown. This bandwidth results to be the limiting factor in the PLLs.
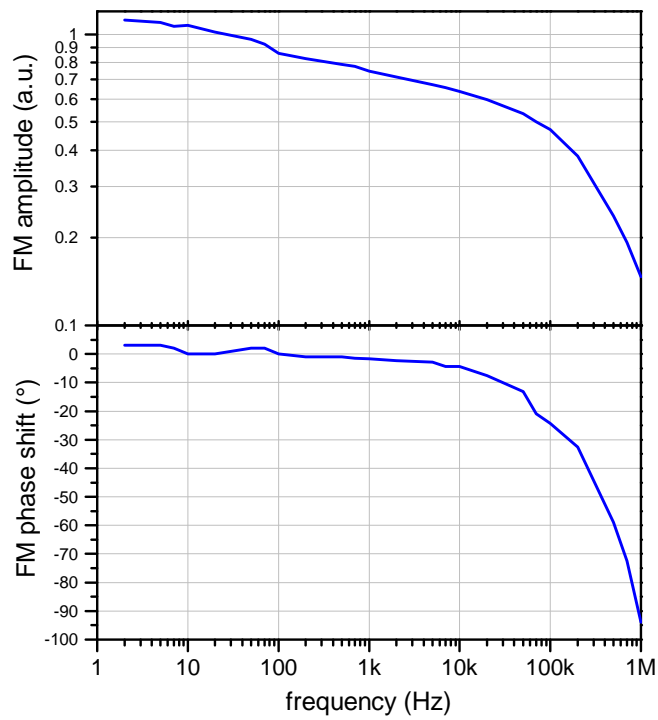
Figure A.1: Frequency modulation bandwidth of the QCL used for the experiments reported in section 2.1. From the shape of the two graphs a bandwidth of about 200 kHz is inferred. FM: frequency modulation.

A.6 The Vernier technique

The Vernier technique is a valuable tool for the study of OFCs spectra and for spectroscopy [85, 86, 88]. It enables the filtering of the modes of an OFC using a high-finesse optical cavity. For a schematic representation see fig. 2.19. The *Vernier ratio* is defined as $Vr = f_s/$FSR. If $Vr = 1$ (or any integer) each comb mode is in resonance with the cavity, therefore everyone is transmitted. If Vr is slightly detuned from 1, only one mode at a time is in resonance with the cavity, therefore, by tuning the cavity length, the comb spectrum can be resolved. The Vernier ratio can also assume a fractional value expressed as $Vr = n/m$, where *n* and *m* are two integers. In this case only one comb mode every *m* is in resonance with the cavity at a time. Still detuning the cavity length in order to cover one FSR all of them are in resonance, but in *m* subgroups at a time (see fig. A.2).
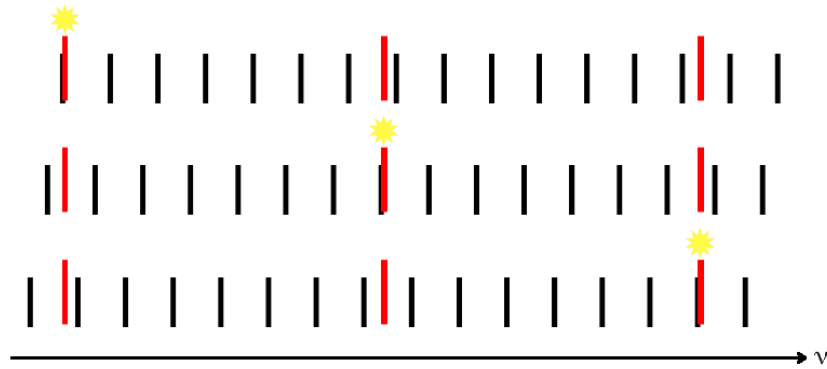
Figure A.2: Schematic representation of the Vernier technique in the optical-frequencies domain with $Vr = 20/3$, where the black lines are the cavity resonances and the red ones are the OFC modes. By moving the cavity resonances in order to cover a FSR (slip to the left) the OFC modes are in resonance in 3 subgroups at a time, as represented by the stars.

A.7 OFC as pure transfer oscillator: the DDS locking scheme

In order to have a DFG radiation characterized by a narrow linewidth, it is crucial to employ two master sources (*pump* and *signal*) characterized by the same spectrum shape, ideally *phase-locked*. Since they

are tens of terahertz far apart, an intermediate transfer oscillator like an OFC is required (see fig. A.3). It is not enough to phase-lock the two

Figure A.3: Schematic representation of the OFC used as transfer oscillator, where the black lines are the OFC modes, while the red ones are the *signal* and the *pump* sources, respectively. N_s and N_p are two integers identifying the closest comb modes (where $N = 0$ for the ideal OFC mode that is the closest to $\nu = 0$).

sources to the closest modes of the OFC by using the standard approach because the fluctuations of the spacing among the modes would affect the DFG. Even though the spacing is somehow stabilized, the residual fluctuations can still be important since the two master sources are phase-locked to two OFC modes which are separated by many other modes, therefore the spacing fluctuations are significantly amplified. In order to overcome this trouble an alternative scheme based on the direct digital synthesis (DDS) of RFs has been introduced [70, 74, 75]. A dedicated electronics (the so-called DDS) multiplies the *signal* beat note by a factor $(N_p - N_s)/N_s$ given by the relative distance in frequency between the two master sources, where N_s and N_p are two integers identifying the closest comb modes ($N = 0$ for the ideal OFC mode that is the closest to $\nu = 0$). Then the obtained signal is used as reference for the phase locking of the *pump* with a large bandwidth. An absolute frequency traceability of the generated DFG radiation is obtained by controlling the frequency of the *signal* against the nearest OFC mode with a low-bandwidth PLL. By using this scheme the OFC frequency fluctuations do not affect the DFG radiation. In particular, on short time scales the linewidth of the DFG radiation is proportional to the *signal* one,[19] while on long time scales the stability is given by the OFC.

In case the *signal* radiation is a portion of the OFC itself (see section 2.2.1), a LO source in the proximity is still needed in order to convert the frequency fluctuations of the OFC *signal* modes to an RF

---

[19]This fact is particularly evident in fig. 2.6 for the DFG FNPSD, where the residual $1/f$ trend between 30 Hz and 1 kHz is given by the *signal* laser, the Nd:YAG.
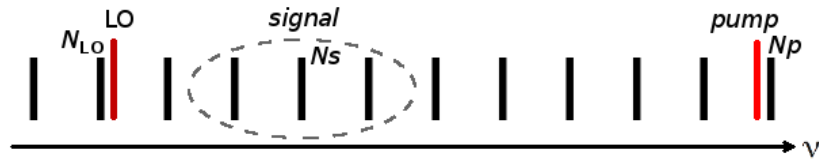
Figure A.4: Schematic representation of the OFC used as transfer oscillator, where the black lines are the OFC modes, while the red ones are the LO and the *pump* sources, respectively. The OFC modes used as *signal* are marked. N_{LO}, N_s and N_p are three integers identifying the closest comb modes (where $N = 0$ for the ideal OFC mode that is the closest to $\nu = 0$).

signal (see fig. A.4). Again the DDS multiplies the *signal* beat note by a factor $(N_p - N_s)/N_{LO}$, and the obtained signal is used as reference for the phase locking of the *pump*. On short time scales the linewidth of the DFG radiation is proportional to the LO one. In this case the perfect compensation operated by the DDS is strictly valid only for one of the OFC modes. See section 2.2.1 for details.

Abbreviations

DDS	direct digital synthesis
DOF	degree of freedom
DFB	distributed feedback
DFG	difference-frequency generation
ECDL	external-cavity diode laser
FET	field-effect transistor
FFT	fast Fourier transform
FIR	far infrared
FNPSD	frequency noise power spectral density
FSR	free spectral range
FTIR	Fourier transform interferometer
FWHM	full width at half maximum
FWM	four-wave mixing
HBNS	heterodyne beat-note signal
HWHM	half width at half maximum
LO	local oscillator
MBE	molecular beam epitaxy
MIR	mid infrared
NIR	near infrared

NPSD	noise power spectral density
OFC	optical frequency comb
OPO	optical parametric oscillator
PID	proportional-integral-derivative
PLL	phase-locked loop
PPLN	periodically-poled lithium niobate ($LiNbO_3$)
PS	polarization spectroscopy
QCL	quantum cascade laser
RF	radio frequency
RMS	root mean square
SFG	sum-frequency generation
SHG	second-harmonic generation
S/N	signal-to-noise ratio
VNPSD	voltage noise power spectral density

Bibliography

[1] ISO 20473:2007 – Optics and photonics – Spectral bands. [page 11]

[2] T. Miyasaka and T. Watanabe. Enhanced CO_2 greenhouse to compensate for reduced solar luminosity on early earth. *Nature*, **277**, 22, 1979. [page 11]

[3] D. A. Lashof and D. R. Ahuja. Relative contributions of greenhouse gas emissions to global warming. *Nature*, **344**, 529–531, 1990. [page 11]

[4] I. Galli, S. Bartalini, S. Borri, P. Cancio, D. Mazzotti, P. De Natale, and G. Giusfredi. Molecular gas sensing below parts per trillion: Radiocarbon-dioxide optical detection. *Phys. Rev. Lett.*, **107**, 270802, 2011. [pages 11, 79]

[5] I. Galli, S. Bartalini, P. Cancio, P. De Natale, D. Mazzotti, G. Giusfredi, M. Fedi, and P. A. Mandó. Optical detection of radiocarbon dioxide: First results and AMS intercomparison. *Radiocarbon*, **55**, 213–223, 2013. [page 11]

[6] Harvard-Smithsonian Center for Astrophysics (CfA), V. E. Zuev Insitute of Atmosperic Optics (IAO). HITRAN on the Web. *http://hitran.iao.ru/*, 2012. [pages 12, 22, 69, 77, 79, 93, 118]

[7] P. Maddaloni, M. Bellini, and P. De Natale. *Laser-based measurements for time and frequency domain applications: a handbook.*

CRC Press, 6000 Broken South Parkway NW 300, Boca Raton, FL 33487-2742, USA, 2013. [pages 12, 69, 74]

[8] G. Modugno, M. Inguscio, and G. M. Tino. Search for small violations of the symmetrization postulate for spin-0 particles. *Phys. Rev. Lett.*, **81**, 4790–4793, 1998. [page 12]

[9] G. Modugno and M. Modugno. Testing the symmetrization postulate on molecules with three identical nuclei. *Phys. Rev. A*, **62**, 022115, 2000. [page 12]

[10] D. Mazzotti, P. Cancio, G. Giusfredi, M. Inguscio, and P. De Natale. Search for exchange-antisymmetric states for spin-0 particles at the 10^{-11} level. *Phys. Rev. Lett.*, **86**, 1919–1922, 2001. [page 12]

[11] T. H. Maiman. Stimulated optical radiation in ruby. *Nature*, **187**, 493–494, 1960. [page 12]

[12] H. W. Mocker and R. J. Collins. Mode competition and self-locking effects in a Q-switched ruby laser. *Appl. Phys. Lett.*, **7**, 270–273, 1965. [page 12]

[13] J. Faist, F. Capasso, D. L. Sivco, C. Sirtori, A. L. Hutchinson, and A. Y. Cho. Quantum cascade laser. *Science*, **264**, 553–556, 1994. [pages 13, 57]

[14] A. S. Pine. Doppler-limited molecular spectroscopy by difference-frequency mixing. *J. Opt. Soc. Am.*, **64**, 1683–1690, 1974. [page 13]

[15] E. J. Lim, H. M. Hertz, M. L. Bortz, and M. M. Fejer. Infrared radiation generated by quasi-phase-matched difference-frequency mixing in a periodically poled lithium niobate waveguide. *Appl. Phys. Lett.*, **59**, 2207–2209, 1991. [pages 13, 70, 82]

[16] E. P. Ippen, C. V. Shank, and A. Dienes. Passive mode locking of the cw dye laser. *Appl. Phys. Lett.*, **21**, 348–350, 1972. [page 13]

[17] T. Udem, J. Reichert, R. Holzwarth, and T. W. Hänsch. Absolute optical frequency measurement of the cesium D_1 line with a mode-locked laser. *Phys. Rev. Lett.*, **82**, 3568–3571, 1999. [page 13]

[18] T. Udem, J. Reichert, R. Holzwarth, and T. W. Hänsch. Accurate measurement of large optical frequency differences with a mode-locked laser. *Opt. Lett.*, **24**, 881–883, 1999. [page 13]

[19] S. A. Diddams, D. J. Jones, J. Ye, S. T. Cundiff, J. L. Hall, J. K. Ranka, R. S. Windeler, R. Holzwarth, T. Udem, and T. W. Hänsch. Direct link between microwave and optical frequencies with a 300 THz femtosecond laser comb. *Phys. Rev. Lett.*, **84**, 5102–5105, 2000. [page 13]

[20] P. Maddaloni, P. Cancio, and P. De Natale. Optical comb generators for laser frequency measurement. *Meas. Sci. Technol.*, **20**, 052001, 2009. [page 13]

[21] A. Foltynowicz, T. Ban, P. Masłowski, F. Adler, and J. Ye. Quantum-noise-limited optical frequency comb spectroscopy. *Phys. Rev. Lett.*, **107**, 233002, 2011. [page 13]

[22] A. L. Wolf, J. Morgenweg, J. C. J. Koelemeij, S. A. van den Berg, W. Ubachs, and K. S. E. Eikema. Direct frequency-comb spectroscopy of a dipole-forbidden clock transition in trapped $^{40}Ca^+$ ions. *Opt. Lett.*, **36**, 49–51, 2011. [page 13]

[23] L. C. Sinclair, I. Coddington, W. C. Swann, G. B. Rieker, A. Hati, K. Iwakuni, and N. R. Newbury. Operation of an optically coherent frequency comb outside the metrology lab. *Opt. Express*, **22**, 6996–7006, 2014. [page 13]

[24] P. Maddaloni, P. Malara, G. Gagliardi, and P. De Natale. Mid-infrared fibre-based optical comb. *New J. Phys.*, **8**, 1–8, 2006. [page 13]

[25] E. Baumann, F. R. Giorgetta, W. C. Swann, A. M. Zolot, I. Coddington, and N. R. Newbury. Spectroscopy of the methane ν_3 band with an accurate midinfrared coherent dual-comb spectrometer. *Phys. Rev. A*, **84**, 062513, 2011. [page 13]

[26] A. Ruehl, A. Gambetta, I. Hartl, M. E. Fermann, K. S. E. Eikema, and M. Marangoni. Widely-tunable mid-infrared frequency comb source based on difference frequency generation. *Opt. Lett.*, **37**, 2232–2234, 2012. [pages 13, 80]

[27] A. Schliesser, N. Picqué, and T. W. Hänsch. Mid-infrared frequency combs. *Nat. Photon.*, **6**, 440–449, 2012. [pages 13, 79]

[28] F. Zhu, H. Hundertmark, A. A. Kolomenskii, J. Strohaber, R. Holzwarth, and H. A. Schuessler. High-power mid-infrared frequency comb source based on a femtosecond Er:fiber oscillator. *Opt. Lett.*, **38**, 2360–2362, 2013. [pages 13, 80]

[29] T. J. Kippenberg, R. Holzwarth, and S. A. Diddams. Microresonator-based optical frequency combs. *Science*, **332**, 555–559, 2011. [pages 13, 94]

[30] C. Y. Wang, T. Herr, P. Del'Haye, A. Schliesser, J. Hofer, R. Holzwarth, T. W. Hänsch, N. Picqué, and T. J. Kippenberg. Mid-infrared optical frequency combs at 2.5 μm based on crystalline microresonators. *Nat. Commun.*, **4**, 1345, 2013. [page 13]

[31] A. G. Griffith, R. K. W. Lau, J. Cardenas, Y. Okawachi, A. Mohanty, R. Fain, Y. H. D. Lee, M. Yu, C. T. Phare, C. B. Poitras, A. L. Gaeta, and M. Lipson. Silicon-chip mid-infrared frequency comb generation. *Nat. Commun.*, **6**, 1–5, 2015. [page 13]

[32] C. Lecaplain, C. Javerzac-Galy, E. Lucas, J. D. Jost, and T. J. Kippenberg. Quantum cascade laser kerr frequency comb. *ArXiv*, 1506.00626, 2015. [page 13]

[33] A. A. Savchenkov, V. S. Ilchenko, F. Di Teodoro, P. M. Belden, W. T. Lotshaw, A. B. Matsko, and L. Maleki. Generation of kerr combs centered at 4.5 μm in crystalline microresonators pumped with quantum-cascade lasers. *Opt. Lett.*, **40**, 3468–3471, 2015. [page 13]

[34] A. Hugi, G. Villares, S. Blaser, H. C. Liu, and J. Faist. Mid-infrared frequency comb based on a quantum cascade laser. *Nature*, **492**, 229–233, 2012. [pages 13, 61, 80, 94, 97]

[35] C. Wieman and T. W. Hänsch. Doppler-free laser polarization spectroscopy. *Phys. Rev. Lett.*, **36**, 1170–1173, 1976. [pages 13, 28]

[36] G. Herzberg. *Molecular spectra and molecular structure. II Infrared and Raman spectra of polyatomic molecules*. Van Nostrand Reinhold Company, New York, USA, 1950. [pages 16, 18]

[37] W. Demtröder. *Atoms, molecules and photons. An introduction to atomic-, molecular- and quantum-physics*. Springer, Berlin, Germany, 2006. [page 18]

[38] W. Demtröder. *Laser spectroscopy. Vol. 1: Basic principles*. Springer, Berlin, Germany, 2008. [page 21]

[39] D. Mazzotti, P. Cancio, G. Giusfredi, P. De Natale, and M. Prevedelli. Frequency-comb-based absolute frequency measurements in the mid-infrared with a difference-frequency spectrometer. *Opt. Lett.*, **30**, 997–999, 2005. [pages 23, 65]

[40] W. Demtröder. *Laser spectroscopy. Vol. 2: Experimental techniques*. Springer, Berlin, Germany, 2008. [pages 24, 28, 29]

[41] S. Bartalini, S. Borri, and P. De Natale. Doppler-free polarization spectroscopy with a quantum cascade laser at 4.3 μm. *Opt. Express*, **17**, 7440–7449, 2009. [pages 30, 65]

[42] J. D. Jackson. *Classical Electrodynamics*. John Wiley & Sons, third ed., 1999. [page 31]

[43] A. Yariv. *Quantum Electronics*. John Wiley & Sons, New York, USA, third ed., 1989. [pages 32, 41]

[44] M. Born and E. Wolf. *Principles of optics: electromagnetic theory of propagation, interference and diffraction of light*. Pergamon Press, Oxford, UK, 1975. [page 36]

[45] R. Boyd. *Nonlinear optics*. Elsevier/Academic Press, Amsterdam, The Netherlands, third ed., 2008. [page 37]

[46] A. Yariv. *Optical electronics in modern communications*. Oxford University Press, New York, USA, fifth ed., 1997. [page 39]

[47] C. P. Christensen, L. W. Braverman, W. H. Steier, and C. Wittig. Active mode locking of the XeF laser. *Appl. Phys. Lett.*, **29**, 424–425, 1976. [page 45]

[48] W. Schmidt and F. P. Schäfer. Self-mode-locking of dye-lasers with saturated absorbers. *Phys. Lett. A*, **26**, 558–559, 1968. [page 45]

[49] U. Keller, K. J. Weingarten, F. X. Kartner, D. Kopf, B. Braun, I. D. Jung, R. Fluck, C. Honninger, N. Matuschek, and J. Aus der Au. Semiconductor saturable absorber mirrors (SESAM's) for femtosecond to nanosecond pulse generation in solid-state lasers. *IEEE J. Sel. Top. Quant.*, **2**, 435–453, 1996. [page 45]

[50] A. E. Siegman. *Lasers*. University Science Books, Mill Valley, California, USA, 1986. [pages 46, 62]

[51] J. Herrmann. Theory of Kerr-lens mode locking: role of self-focusing and radially varying gain. *J. Opt. Soc. Am. B*, **11**, 498–512, 1994. [page 46]

[52] J. Reichert, R. Holzwarth, T. Udem, and T. W. Hänsch. Measuring the frequency of light with mode-locked lasers. *Opt. Commun.*, **172**, 59–68, 1999. [page 47]

[53] K. Petermann. *Laser diode modulation and noise*. Kluwer Academic Publishers, Dordrecht, The Netherlands, 1991. [page 49]

[54] D. S. Elliott, R. Roy, and S. J. Smith. Extracavity laser bandshape and bandwidth modification. *Phys. Rev. A*, **26**, 12–18, 1982. [page 53]

[55] A. L. Schawlow and C. H. Townes. Infrared and optical masers. *Phys. Rev.*, **112**, 1940–1949, 1958. [page 54]

[56] C. H. Henry. Theory of the linewidth of semiconductor lasers. *IEEE J. Quantum Electron.*, **18**, 259–264, 1982. [page 55]

[57] R. F. Kazarinov and R. A. Suris. Possibility of the amplification of electromagnetic waves in a semiconductor with a superlattice. *Sov. Phys. Semicond.*, **5**, 707–709, 1971. [page 57]

[58] J. Faist. *Quantum cascade lasers*. Oxford University Press, Oxford, UK, 2013. [pages 59, 124, 128]

[59] M. Beck, D. Hofstetter, T. Aellen, J. Faist, U. Oesterle, M. Ilegems, E. Gini, and H. Melchior. Continuous wave operation of a mid-infrared semiconductor laser at room temperature. *Science*, **295**, 301–305, 2002. [page 60]

[60] J. Faist, C. Gmachl, F. Capasso, C. Sirtori, D. L. Sivco, J. N. Baillargeon, and A. Y. Cho. Distributed feedback quantum cascade lasers. *Appl. Phys. Lett.*, **70**, 2670–2672, 1997. [page 61]

[61] J. Faist, M. Beck, T. Aellen, and E. Gini. Quantum-cascade lasers based on a bound-to-continuum transition. *Appl. Phys. Lett.*, **78**, 147–149, 2001. [page 61]

[62] C. Gmachl, D. L. Sivco, R. Colombelli, F. Capasso, and A. Y. Cho. Ultra-broadband semiconductor laser. *Nature*, **415**, 883–887, 2002. [page 61]

[63] P. Friedli, H. Sigg, B. Hinkov, A. Hugi, S. Riedi, M. Beck, and J. Faist. Four-wave mixing in a quantum cascade laser amplifier. *Appl. Phys. Lett.*, **102**, 222104–1–4, 2013. [page 61]

[64] J. B. Khurgin, Y. Dikmelik, A. Hugi, and J. Faist. Coherent frequency combs produced by self frequency modulation in quantum cascade lasers. *Appl. Phys. Lett.*, **104**, 081118, 2014. [pages 62, 95, 96]

[65] G. Villares and J. Faist. Quantum cascade laser combs: effects of modulation and dispersion. *Opt. Express*, **23**, 1651–1669, 2015. [pages 62, 95, 96]

[66] S. Bartalini, S. Borri, P. Cancio, A. Castrillo, I. Galli, G. Giusfredi, D. Mazzotti, L. Gianfrani, and P. De Natale. Observing the intrinsic linewidth of a quantum-cascade laser: Beyond the Schawlow-Townes limit. *Phys. Rev. Lett.*, **104**, 083904–1–4, 2010. [pages 64, 94]

[67] F. Cappelli, I. Galli, S. Borri, G. Giusfredi, P. Cancio, D. Mazzotti, A. Montori, N. Akikusa, M. Yamanishi, S. Bartalini, and P. De Natale. Sub-kilohertz linewidth room-temperature mid-IR quantum cascade laser using a molecular sub-doppler reference. *Opt. Lett.*, **37**, 4811–4813, 2012. [pages 64, 117]

[68] S. Bartalini, S. Borri, I. Galli, G. Giusfredi, D. Mazzotti, T. Edamura, N. Akikusa, M. Yamanishi, and P. De Natale. Measuring frequency noise and intrinsic linewidth of a room-temperature DFB quantum cascade laser. *Opt. Express*, **19**, 17996–18003, 2011. [pages 66, 94, 102]

[69] L. Tombez, J. D. Francesco, S. Schilt, G. D. Domenico, J. Faist, P. Thomann, and D. Hofstetter. Frequency noise of free-running 4.6 μm distributed feedback quantum cascade lasers near room temperature. *Opt. Lett.*, **36**, 3109–3111, 2011. [pages 66, 72, 94, 102]

[70] I. Galli, S. Bartalini, P. Cancio, G. Giusfredi, D. Mazzotti, and P. De Natale. Ultra-stable, widely tunable and absolutely linked mid-IR coherent source. *Opt. Express*, **17**, 9582–9587, 2009. [pages 66, 70, 85, 132]

[71] S. M. Foreman, A. Marian, J. Ye, E. A. Petrukhin, M. A. Gubin, O. D. Mücke, F. N. C. Wong, E. P. Ippen, and F. X. Kärtner. Demonstration of a HeNe/CH$_4$-based optical molecular clock. *Opt. Lett.*, **30**, 570–572, 2005. [page 69]

[72] A. Mills, D. Gatti, J. Jiang, C. Mohr, W. Mefford, L. Gianfrani, M. Fermann, I. Hartl, and M. Marangoni. Coherent phase lock of a 9 μm quantum cascade laser to a 2 μm thulium optical frequency comb. *Opt. Lett.*, **37**, 4083–4085, 2012. [page 69]

[73] I. Galli, M. S. de Cumis, F. Cappelli, S. Bartalini, D. Mazzotti, S. Borri, A. Montori, N. Akikusa, M. Yamanishi, G. Giusfredi, P. Cancio, and P. De Natale. Comb-assisted subkilohertz linewidth quantum cascade laser for high-precision mid-infrared spectroscopy. *Appl. Phys. Lett.*, **102**, 121117, 2013. [pages 70, 75, 117]

[74] H. R. Telle, B. Lipphardt, and J. Stenger. Kerr-lens, mode-locked lasers as transfer oscillators for optical frequency measurements. *Appl. Phys. B*, **74**, 1–6, 2002. [pages 70, 132]

[75] I. Galli, S. Bartalini, S. Borri, P. Cancio, G. Giusfredi, D. Mazzotti, and P. De Natale. Ti:sapphire laser intracavity difference-

frequency generation of 30 mW cw radiation around 4.5 μm. *Opt. Lett.*, **35**, 3616–3618, 2010. [pages 70, 81, 83, 132]

[76] M. Prevedelli, T. Freegarde, and T. W. Hänsch. Phase locking of grating-tuned diode laser. *Appl. Phys. B*, **60**, S241–S248, 1995. [page 72]

[77] I. Galli, S. Bartalini, P. Cancio, F. Cappelli, G. Giusfredi, D. Mazzotti, N. Akikusa, M. Yamanishi, and P. De Natale. Absolute frequency measurements of CO_2 transitions at 4.3 μm with a comb-referenced quantum cascade laser. *Mol. Phys.*, **111**, 2041–2045, 2013. [pages 75, 117]

[78] G. Guelachvili and K. R. Rao. *Handbook of infrared standards: with spectral maps and transition assignments between 3 and 2600 μm*. Academic Press, Orlando, Florida, USA, 2012. [page 79]

[79] F. Adler, K. C. Cossel, M. J. Thorpe, I. Hartl, M. E. Fermann, and J. Ye. Phase-stabilized, 1.5 W frequency comb at 2.8–4.8 μm. *Opt. Lett.*, **34**, 1330–1332, 2009. [pages 80, 87]

[80] K. L. Vodopyanov, E. Sorokin, I. T. Sorokina, and P. G. Schunemann. Mid-IR frequency comb source spanning 4.4–5.4 μm based on subharmonic GaAs optical parametric oscillator. *Opt. Lett.*, **36**, 2275–2277, 2011. [pages 80, 87]

[81] S. A. Meek, A. Poisson, G. Guelachvili, T. W. Hänsch, and N. Picqué. Fourier transform spectroscopy around 3 μm with a broad difference frequency comb. *Appl. Phys. B*, 2013. [page 80]

[82] T. W. Neely, T. A. Johnson, and S. A. Diddams. High-power broadband laser source tunable from 3.0 μm to 4.4 μm based on a femtosecond Yb:fiber oscillator. *Opt. Lett.*, **36**, 4020–4022, 2011. [page 80]

[83] I. Galli, F. Cappelli, P. Cancio, G. Giusfredi, D. Mazzotti, S. Bartalini, and P. De Natale. High-coherence mid-infrared frequency comb. *Opt. Express*, **21**, 28877–28885, 2013. [pages 80, 112, 118]

[84] T. W. Hänsch and B. Couillaud. Laser frequency stabilization by polarization spectroscopy of a reflecting reference cavity. *Opt. Commun.*, **35**, 441–444, 1980. [page 82]

[85] F. Adler, M. J. Thorpe, K. C. Cossel, and J. Ye. Cavity-enhanced direct frequency comb spectroscopy: Technology and applications. *Annu. Rev. Anal. Chem.*, **3**, 175–205, 2010. [pages 85, 131]

[86] I. Galli, S. Bartalini, P. Cancio, F. Cappelli, G. Giusfredi, D. Mazzotti, N. Akikusa, M. Yamanishi, and P. De Natale. Mid-infrared frequency comb for broadband high precision and sensitivity molecular spectroscopy. *Opt. Lett.*, **39**, 5050–5053, 2014. [pages 89, 118, 131]

[87] G. Giusfredi, S. Bartalini, S. Borri, P. Cancio, I. Galli, D. Mazzotti, and P. De Natale. Saturated-absorption cavity ring-down spectroscopy. *Phys. Rev. Lett.*, **104**, 110801, 2010. [page 91]

[88] C. Gohle, B. Stein, A. Schliesser, T. Udem, and T. W. Hänsch. Frequency comb Vernier spectroscopy for broadband, high-resolution, high-sensitivity absorption and dispersion spectra. *Phys. Rev. Lett.*, **99**, 263902, 2007. [pages 91, 131]

[89] G. Villares, A. Hugi, S. Blaser, and J. Faist. Dual-comb spectroscopy based on quantum-cascade-laser frequency combs. *Nat. Commun.*, **5**, 5192, 2014. [pages 94, 97]

[90] M. Yamanishi, T. Edamura, K. Fujita, N. Akikusa, and H. Kan. Theory of the intrinsic linewidth of quantum-cascade lasers: Hidden reason for the narrow linewidth and line-broadening by thermal photons. *IEEE J. Quantum Electron.*, **44**, 12–29, 2008. [page 94]

[91] T. Liu and Q. J. Wang. Fundamental frequency noise and linewidth broadening caused by intrinsic temperature fluctuations in quantum cascade lasers. *Phys. Rev. B*, **84**, 125322, 2011. [page 94]

[92] F. Cappelli, G. Villares, S. Riedi, and J. Faist. Intrinsic linewidth of quantum cascade laser frequency combs. *Optica*, **2**, 836–840, 2015. [pages 94, 118]

[93] Y. K. Chembo. Quantum correlations, entanglement, and squeezed states of light in kerr optical frequency combs. *ArXiv*, 1412.5700, 2014. [pages 95, 96]

[94] C. Benkert, M. O. Scully, J. Bergou, L. Davidovich, M. Hillery, and M. Orszag. Role of pumping statistics in laser dynamics: quantum Langevin approach. *Phys. Rev. A*, **41**, 2756–2765, 1990. [page 96]

[95] H. Haken and M. Pauthier. Nonlinear theory of multimode action in loss modulated lasers. *IEEE J. Quantum Electron.*, **4**, 454–459, 1968. [page 96]

[96] G. Grynberg, A. Aspect, and C. Fabre. *Introduction to quantum optics, from the semi-classical approach to quantized light*. Cambridge University Press, 32 Avenue of the Americas, New York, NY 10013-2473, USA, 2010. [page 97]

[97] S. Schilt, N. Bucalovic, V. Dolgovskiy, C. Schori, M. C. Stumpf, G. Di Domenico, S. Pekarek, A. E. H. Oehler, T. Südmeyer, U. Keller, and P. Thomann. Fully stabilized optical frequency comb with sub-radian CEO phase noise from a SESAM-modelocked 1.5-μm solid-state laser. *Opt. Express*, **19**, 24171–24181, 2011. [page 104]

[98] F. Cappelli *et al.* Stability measurements of a quantum cascade laser frequency comb. *To be submitted*. [pages 104, 118]

[99] R. Shiloh and A. Arie. Spectral and temporal holograms with nonlinear optics. *Opt. Lett.*, **37**, 3591–3593, 2012. [page 119]

[100] A. Leshem, R. Shiloh, and A. Arie. Experimental realization of spectral shaping using nonlinear optical holograms. *Opt. Lett.*, **39**, 5370–5373, 2014. [page 119]

[101] F. W. Helbing, G. Steinmeyer, J. Stenger, H. R. Telle, and U. Keller. Carrier-envelope-offset dynamics and stabilization of femtosecond pulses. *Appl. Phys. B*, **74**, 35–42, 2002. [page 127]

[102] S. Riedi, F. Cappelli, S. Blaser, P. Baroni, A. Müller, and J. Faist. Broadband superluminescence, 5.9 μm to 7.2 μm, of a quantum cascade gain device. *Opt. Express*, **23**, 7184–7189, 2015.

[103] L. Tombez, F. Cappelli, S. Schilt, G. Di Domenico, S. Bartalini, and D. Hofstetter. Wavelength tuning and thermal dynamics of continuous-wave mid-infrared distributed feedback quantum cascade lasers. *Appl. Phys. Lett.*, **103**, 031111, 2013.

[104] S. Borri, I. Galli, F. Cappelli, A. Bismuto, S. Bartalini, P. Cancio, G. Giusfredi, D. Mazzotti, J. Faist, and P. De Natale. Direct link of a mid-infrared QCL to a frequency comb by optical injection. *Opt. Lett.*, **37**, 1011–1013, 2012.
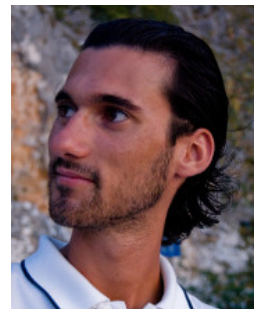
List of Figures

⌐ Curriculum vitæ & Publications list

Francesco Cappelli

Place and date of birth	Firenze, September 26, 1986
Email addresses	francesco.cappelli@ino.it
	francesco.cappelli@phys.ethz.ch

Work experience	Research in Physics - Optics
	(laser sources and gas spectroscopy)

· November 30, 2012 – today: PhD student
University of Florence c/o LENS - European Laboratory for Non-Linear Spectroscopy, Via Nello Carrara 1, 50019 Sesto Fiorentino (FI) - Italy.

· February 15, 2014 – December 31, 2014: Guest PhD student
ETH - Swiss Federal Institute of Technology (Zurich branch), Auguste-Piccard-Hof 1, CH-8093 Zürich - Switzerland.

· April 26, 2012 – November 30, 2012: Fellowship
CNR-INO - Italian National Institute of Optics (Florence branch)

c/o LENS - European Laboratory for Non-Linear Spectroscopy, Via Nello Carrara 1, 50019 Sesto Fiorentino (FI) - Italy.

· January 2009 – December 2011: Master in Physics (110/110 cum laude)
University of Florence (Italy) – Physics of Matter - Optics
Thesis title: Direct link of a mid-infrared quantum cascade laser to a frequency comb by optical injection.

Scientific publishing activity

· Collaboration as reviewer to the journal Applied Physics Letters, AIP Publishing, LLC, Suite 1NO1, 2 Huntington Quadrangle, Melville, NY 11747-4502, USA.

· Collaboration as reviewer to the journal Optics Express, OSA - The Optical Society, 2010 Massachusetts Ave., N.W. Washington, D.C. 20036-1012, USA.

Publications List

1. F. Cappelli, G. Villares, S. Riedi, and J. Faist. Intrinsic linewidth of quantum cascade laser frequency combs. *Optica*, **2**, 836–840, 2015

2. S. Riedi, F. Cappelli, S. Blaser, P. Baroni, A. Müller, and J. Faist. Broadband superluminescence, 5.9 μm to 7.2 μm, of a quantum cascade gain device. *Opt. Express*, **23**, 7184–7189, 2015

3. I. Galli, S. Bartalini, P. Cancio, F. Cappelli, G. Giusfredi, D. Mazzotti, N. Akikusa, M. Yamanishi, and P. De Natale. Mid-infrared frequency comb for broadband high precision and sensitivity molecular spectroscopy. *Opt. Lett.*, **39**, 5050–5053, 2014

4. L. Tombez, F. Cappelli, S. Schilt, G. Di Domenico, S. Bartalini, and D. Hofstetter. Wavelength tuning and thermal dynamics of continuous-wave mid-infrared distributed feedback quantum cascade lasers. *Appl. Phys. Lett.*, **103**, 031111, 2013

5. I. Galli, F. Cappelli, P. Cancio, G. Giusfredi, D. Mazzotti, S. Bartalini, and P. De Natale. High-coherence mid-infrared frequency comb. *Opt. Express*, **21**, 28877–28885, 2013

6. I. Galli, S. Bartalini, P. Cancio, F. Cappelli, G. Giusfredi, D. Mazzotti, N. Akikusa, M. Yamanishi, and P. De Natale. Absolute frequency measurements of CO_2 transitions at 4.3 μm with a comb-referenced quantum cascade laser. *Mol. Phys.*, **111**, 2041–2045, 2013

7. I. Galli, M. S. de Cumis, F. Cappelli, S. Bartalini, D. Mazzotti, S. Borri, A. Montori, N. Akikusa, M. Yamanishi, G. Giusfredi, P. Cancio, and P. De Natale. Comb-assisted subkilohertz linewidth quantum cascade laser for high-precision mid-infrared spectroscopy. *Appl. Phys. Lett.*, **102**, 121117, 2013

8. F. Cappelli, I. Galli, S. Borri, G. Giusfredi, P. Cancio, D. Mazzotti, A. Montori, N. Akikusa, M. Yamanishi, S. Bartalini, and P. De Natale. Sub-kilohertz linewidth room-temperature mid-IR quantum cascade laser using a molecular sub-doppler reference. *Opt. Lett.*, **37**, 4811–4813, 2012

9. S. Borri, I. Galli, F. Cappelli, A. Bismuto, S. Bartalini, P. Cancio, G. Giusfredi, D. Mazzotti, J. Faist, and P. De Natale. Direct link of a mid-infrared QCL to a frequency comb by optical injection. *Opt. Lett.*, **37**, 1011–1013, 2012.

International conferences and symposia (oral or poster)

Conference name	Place	Dates
ITQW (The 13th international conference on intersubband transitions in quantum wells) & IWFCTA (International workshop on frequency comb technology and applications) 2015	Vienna, Austria	6 – 11 September 2015
HRMS - High Resolution Molecular Spectroscopy 2015	Dijon, France	24 – 28 August 2015

CLEO Europe 2015 - Conference on lasers and electro-optics (awarded with the *2015 Travel grant student award*)	Munich, Germany	21 – 25 June 2015
IQCLSW-2014, International quantum cascade lasers school & workshop 2014 (awarded with the *Nature Photonics best student paper prize*)	Policoro (Matera), Italy	7 – 12 September 2014
Nano-Tera-Microresonator Frequency Combs and their Applications - MFCA 2014	Ascona, Switzerland	17 – 20 August 2014
CLEO USA 2014, Conference on Lasers and Electro-Optics	San Jose (CA), USA	7 – 13 June 2014
SIOF annual meeting (Italian Society of Optics and Photonics)	Rome, Italy	2 December 2013
HRMS - High Resolution Molecular Spectroscopy 2013 (awarded with the *Amat-Mills* prize)	Budapest, Hungary	25 – 30 August 2013
CLEO USA 2013, Conference on Lasers and Electro-Optics	San Jose (CA), USA	9 – 14 June 2013
MPNS COST Action Training School - MP1204 TERA-MIR Radiation: Materials, Generation, Detection and Applications	Cortona (AR), Italy	20 – 24 May 2013
INO Annual Symposium (Italian National Institute of Optics)	Florence, Italy	13 – 14 March 2013
SPTM - International School of Physics and Technology of Matter	Otranto (LE), Italy	17 – 23 September 2012

Acknowledgments

And *dulcis in fundo...* the acknowledments!

First of all I gratefully thank my PhD supervisor Paolo De Natale: he strongly supported and stimulated me in every moment during the course, both from the scientific and the human point of view. Then I gratefully thank my ETH-guest-period supervisor Jérôme Faist: he promptly welcomed me in his group sharing with me the secrets concerning those peculiar devices named quantum cascade lasers.

Then I wish to thank my lab mates. Firstly the historical one, Iacopo Galli, the one with whom I shared most of the work at LENS. He patiently guided me through the learning of the art of performing experiments. Secondly Gustavo Villares, the one with whom I shared most of the work at ETH. He always stimulated me with interesting and smart ideas. Finally Giulio Campo, the last-came. He helped me a lot with the last experiment.

Afterwards, I want to thank both the groups staffs: in particular Saverio Bartalini, Simone Borri and Davide Mazzotti for the help they gave me in writing this thesis, and Pablo Cancio, Giovanni Giusfredi and Mario Siciliani on the Florence side; Giacomo Scalari, Mattias Beck, Andreas Hugi and Erna Hug on the Zürich side. Moreover, I wish to thank my ETH office mates: Borislav Hinkov, Federico Valmorra and Selam Nida. I would also like to recall with affection the other members of the two groups: Luigi Consolino, Annamaria Campa, Cristina Ileana, Christopher Bonzon, Sabine Riedi, Lorenzo Bosco, Markus Rösch, Giancarlo Cerulo, Camille Ndebeka-Bandou, Martin Süess, Curdin Maissen, Johanna Wolf, Janine Keller, Gian Lorenzo Paravicini, Markus Geiser,

Valeria Liverini, Keita Otani... and my PhD mates Tommaso Mazzoni, Stefano Conclave, Giacomo Cappellini, Marco Mancini, Irene Costantini, Claudia Crocini, Lorenzo Gori... On the technicians side I want to thank Marcel Baer, Alessio Montori, Marco De Pas, Mauro Giuntini, Riccardo Ballerini e Ahmed Hajeb.

Finally I thank my family: my mother, my father, my sister, my grandparents and the others. All of them have strongly supported me in every moment and in every way.

This thesis is dedicated to everyone of them.

Francesco